Conformational Dynamics of Guanine Residues Within the Human Telomeric G-quadruplex

by

Susan Y. Liu

A dissertation submitted to the Graduate Faculty in Biochemistry in partial fulfillment of the requirements for the degree of
Doctor of Philosophy, The City University of New York
2012

APPROVAL PAGE

This manuscript has been read and accepted for the Graduate Faculty in Biochemistry in satisfaction of the dissertation requirement for the degree of Doctor of Philosophy.

Prof. Lesley Davenport

Date — Chair of Examining Committee

Prof. Edward J. Kennelly

Date — Executive Officer

Dr. Mary E. Hawkins

Prof. Laura J. Juszczak

Prof. Roberto Sanchez-Delgado

Prof. Brian W. Williams

Supervisory Committee

The City University of New York

ABSTRACT

Conformational Dynamics of Guanine Residues Within the Human Telomeric G-quadruplex

by

Susan Y. Liu

Advisor: Lesley Davenport

The human telomeric single-stranded guanine-rich DNA (HT_4: $d(TTAGGG)_4$) located at the end of chromosomes forms an intramolecular G-quadruplex in the presence of K^+ or Na^+ *in vitro*. The formation and stabilization of this structure by quadruplex interactive agents (QIAs) can inhibit the activity of the enzyme complex telomerase, which is over-activated in cancer cells, and is thus a target for potential cancer therapeutics. However, the solution quadruplex conformation is complex and varies with the presence of stabilizing Na^+ or K^+-ions. In addition, details about the contribution of individual guanine residues of the single stranded HT_4 sequence required for G-quadruplex formation and stabilization remain unclear.

In our studies, we have focused on the conformational dynamics of the human telomeric HT_4 intramolecular G-quadruplex in solution, specifically the role each guanine residue plays in the quadruplex folding process, through investigating their contributions to the global quadruplex stabilities and the local environmental changes around single guanine residue. To accomplish this aim, we have substituted single guanine residues with the fluorescence analog—6MI at guanine positions (G1, G2, G4, G5, G7, G9, G11 and G12) along the HT_4 oligonucleotide. Serving as either both a base mutation and a sensitive probe for local environment changes, the 6MI-substituted oligonucleotides have provided insights into the quadruplex dynamics under physiological conditions.

We have confirmed the formation of G-quadruplex conformations in the presence of 100mM KCl or NaCl by all 6MI-substituted sequences using thermal difference spectroscopy. In general, the global stabilities of the 6MI-labeled sequences (as judged by mid-point of thermal UV-melting profiles and $\Delta G_{folding}$) are weaker than for the parent HT_4, but to varying extents, suggesting that different guanine positions of the quadruplex do indeed play distinct roles in the formation and stabilization of the G-quadruplex. In the presence of K^+, mutations at guanine positions near the 5' and 3'-ends (G2, G4, G9, G11 and G12) destabilize the quadruplex more severely than those positions at the middle (G5 and G7) of the HT_4, due to the better accommodation of bulky 6MI at G5 and G7 through bulging out. For the Na^+-promoted quadruplex conformation, however, the center tetrad guanine mutations appear to have the greatest impact on global stabilities, suggesting their critical roles in chelating with the cations for quadruplex stability.

Studies of local environmental effects around individual guanine positions have been explored using the sensitivity of 6MI fluorescence. With quadruplex folding promoted through either decreasing temperatures or addition of K^+, a decrease in fluorescence intensity generally corresponds to formation of quadruplex. The degree of fluorescence quenching however, varied for different 6MI-labeled sequences, suggesting different extents of base stacking interactions associated with quadruplex folding for each guanine residue. Analyses of fluorescence data from thermal folding or K^+ titration studies suggested a cooperative quadruplex folding pathway, with base nucleation starting at relatively low K^+-ion concentrations (<20mM). In the K^+-stabilized quadruplex, nucleation initiates around the center tetrad (G5 and G11), followed by loop formations (G4, G7 and G9), and finally folding of the terminal ends (G1, G2 and G12). In contrast, for Na^+-stabilized quadruplex folding, the top G-tetrad (G1, G7 and G12) appears to initiate folding, followed by guanines on the middle G-tetrad (G2, G5 and G11).

Interestingly, the G1 labeled position (close to the 5'-end) shows abnormal behavior compared with other substituted positions on folding, with a fluorescence intensity enhancement and spectral shifts to longer wavelength. Our data suggests the flexibility of G1 on

the 5'-end of the sequence in the folded quadruplex conformation with possible strand fraying and H-bonding interactions, over base stacking interactions, as predicted for all other guanine positions.

Time-resolved fluorescence studies were performed to address possible mechanisms for the observed steady-state fluorescence quenching with quadruplex folding. Fluorescence intensity decay profiles were best fit using three decay components for all 6MI-labeled sequences. Although static quenching is evident, presumably arising from base stacking interactions, the observed intensity quenching is dominated by an ultrafast quasi-static self-quenching deactivation route (QSSQ). This effect is greatest for 6MI positions G5 and G11 sandwiched by two guanines, and lowest for G1 near the 5'-end. On K^+-initiated folding, an increase in QSSQ is detected, suggesting that the additional fluorescence intensity quenching may arise from additional (sub-picosecond) electron transfer events or base stacking interactions around the 6MI probe.

Fluorescence decay-associated spectra (DAS), which associate lifetimes (or decay rates) with fluorescence spectral envelopes, can provide insights into the origins of the heterogeneous fluorescence decay observed for the 6MI-labeled oligonucleotides. DAS revealed that the longer wavelength spectral shifts observed for G1 with quadruplex folding are associated with the longest fluorescence decay time τ_1, and appear to originate from enhanced solvent interactions around the G1 fluorophore.

Environmental heterogeneity has been further examined using single value decomposition (SVD) analyses for the absorbance and fluorescence thermal folding profiles. We have extracted at least four components for the unlabeled HT_4 sequence and at least three for the fluorescence melting profiles of the 6MI-labeled sequences. Our data suggest that the folding pathway for the quadruplex formation process involves intermediate states.

Overall, our studies provide additional information and better understanding about the complex HT_4 G-quadruplex conformational dynamics under physiological conditions. Such knowledge can assist in the designing of future anti-cancer drugs targeting the human telomeric quadruplex.

ACKNOWLEDGMENTS

I am heartily thankful to my advisor, Professor Lesley Davenport, whose encouragement, patience, and great support from the initial to the final level enabled me to develop an understanding of the subject, while allowing me the room to work in my own way, and other committee members, Dr. Mary E. Hawkins, Professor Laura Juszczak, Professor Roberto Sanchez-Delgado, and Professor Brian W. Williams for their thorough reviews and illuminating comments from proposal development to thesis completion.

I am grateful to the Biochemistry Program at the Graduate Center and Chemistry Department at Brooklyn College of City University of New York, particularly the faculty, and staff members that I have encountered during my study, for making the whole graduate experience enjoyable and productive.

Lastly, I offer my regards and appreciation to all my families and friends who supported me in any respect during the completion of the project.

TABLE OF CONTENTS

LIST OF FIGURES

LIST OF TABLES

LIST OF ABBREVIATIONS

2-AP	2-Aminopurine
6MI	6-Methyl-8-(2-deoxy-D-ribofuranosyl Isoxanthopterin
8-BrG	8-bromoguanine
ALT	Alternative Lengthening of Telomeres
BMVC	3,6-Bis(1-Methyl-4-Vinylpyridinium) Carbazole diiodide
DAS	Decay-Associated Spectra
DNA	Deoxyribonucleic Acid
ES	Embryonic Stem
FRET	Förster resonance energy transfer
GBA	Glycosidic Bond Angle
HT_4	Human telomeric DNA sequence $(TTAGGG)_4$
hTERT	Human Telomerase Reverse Transcriptase
hTR	Human Telomerase RNA
M1	Mortality Stage 1
M2	Mortality Stage 2
QIAs	Quadruplex Interacting Agents

QSSQ	Quasi Static Self Quenching
RNA	Ribonucleic Acid
SVD	Single Value Decomposition
TDS	Thermal Difference Spectra
Tm	Melting Temperature
WHO	World Health Organization

Chapter 1

INTRODUCTION: TELOMERASE, TELOMERE AND G-QUADRUPLEX

As projected by the World Health Organization (WHO), cancer will become the leading cause of death worldwide in 2011 [1]. Understanding its cause and finding a cure is a long-term goal for the human race. Cancer is not just one disease but many diseases, all characterized by uncontrolled cell division and the spread of abnormal cells. Although different molecular pathways or gene mutations have been found to account for the onset of varying types of cancer, emerging evidence implicates that uncontrolled cell division and therefore immortality of nearly all cancer cells, stems from the abnormally high activity of an enzyme complex called telomerase. Telomerase functions by elongating the telomere (which is involved in controlling the frequency of cell division, as discussed below) through addition of a tandem repeated (TTAGGG) guanine-rich sequence to the 3'-overhang of human chromosome. Its activity is extremely low in normal somatic cells, intermediate in stem cells of renewal tissues (e.g., blood, skin and intestine), but highly active in most cancer cells. Therefore inhibiting the activity of the telomerase presents a potential approach for attenuating the growth of cancer cells. Coincidentally, the guanine-rich telomere can form a four-stranded DNA (G-quadruplexed) conformation *in vitro*, which inhibits the telomerase activity, making it a potential target for cancer therapeutics. This chapter will present background information on telomerase, telomeres and the role of G-quadruplex conformation.

1.1 Telomeres and Telomerase

This section will present an introduction to the function of the telomeres and the activity of telomerase in normal and cancer cells, i.e. how telomere shortening leads to cell aging, and telomerase activation leads to cancer cell immortality.

1.1.1 Telomere Shortening and Cell Aging

Why do human beings age? Although aging is a complicated process and may not be explained by any single molecular or physiological mechanism, one explanation lies in the fundamental issue that human cells are unable to replicate and renew themselves indefinitely. Formal evidence came in 1961, when Hayflick demonstrated that normal human cells can divide approximately 50–70 times (known as the Hayflick limit) before they stop dividing and become senescent [2]. The number of times a cell can divide is actually controlled by the length of telomeres located at the end of chromosomes [3]. In eukaryotic cells, both ends of the chromosomes are protected by telomeres composed of tandem repeat noncoding sequences rich in guanine bases. In human chromosomes, telomeres are repeats of the double stranded 5'-$(TTAGGG)_n$-3' (5-10kilobases) followed by the single stranded 3'-overhang (100-200bases) [4, 5]. Telomeres slow down the linear chromosome shortening arising from the "end of replication problem" in eukaryotic cells.

1.1.2 End of Replication Problem

Eukaryotic chromosomes are shortened after every cell replication cycle due to the "end of replication problem" [6, 7]. In DNA replication, DNA polymerase proceeds only in the the 5' to 3' direction and thus requires a short RNA primer for the lagging DNA strand synthesis (Figure 1.1). After DNA polymerization, the RNA primers are removed and replaced by DNA synthesis extending from an upstream Okazaki fragment. However, the terminal RNA primer can not be replaced with DNA, resulting in a 5'-terminal gap at one end on each daughter chromosome. This replication strategy therefore predicts the progressive shortening

of chromosomal DNA over multiple cycles of replication. Telomeric repeats can temporarily slow down this trend by providing a cushion of expendable noncoding sequences on the chromosome ends. When telomeres become critically short, a DNA damage signal cascade leads to cellular senescence [8, 9]. Therefore, the length of telomere acts as a mitotic clock to count the number of times that a cell can divide across its lifespan.

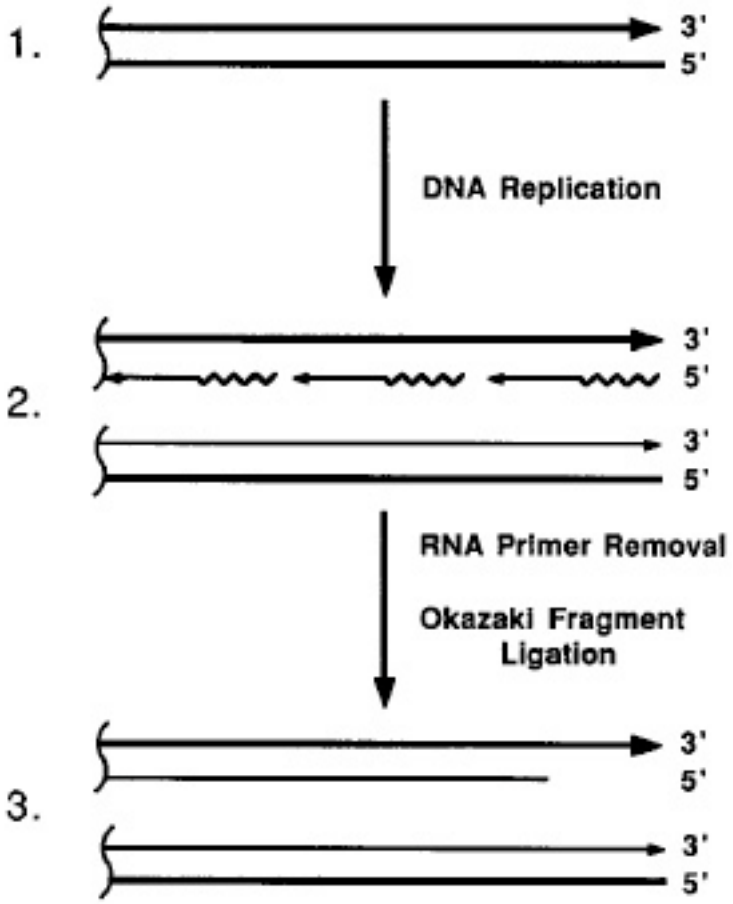

Figure 1.1. The end of replication problem. 1) The molecular end of a DNA molecule is shown. 2) Leading strand replication proceeds to the end of the DNA molecule, while lagging strand replication utilizes RNA primers and Okazaki fragment synthesis. 3) Removal of the RNA primers and Okazaki fragment ligation leaves a region at one end of each daughter molecule unreplicated. Therefore, the daughter chromosomes get shorter with each round of replication. (Figure is taken from Carol W. Greider, *Telomeres, telomerase and senescence.* BioEssays, 12(8): 363–369, 1990.)

1.1.3 Telomerase Activation in Germ-line and Pluripotent Cells

Although it is a general trend that telomeres will shorten, in certain human cell types such as germ-line cells and pluripotent stem cells of renewal tissues (e.g., blood, skin and intestine), their telomere shortening rates can be slowed down, due to the activation of an enzyme named telomerase (Figure 1.2).

Telomerase is a multimeric ribonucleoprotein complex [10–13], in which an essential protein component named human telomerase reverse transcriptase (hTERT) uses an internal RNA sequence – human telomerase RNA (hTR)[14] as a template to catalyze the addition of telomeric sequences to the ends of chromosome [15], as shown in Figure 1.3. Telomerase is only activated in embryonic stem cells [16] and some proliferative reproductive cells, but is mostly inactive in normal somatic cells (Figure 1.2). With higher activity of telomerase and thus telomere length maintenance in these special cell types, the number of times for cell replication and renewal can be increased.

1.1.4 Telomerase Activation Lead Cancer Cells to Escape from Cell Death

The telomerase activity discussed above is highly regulated. On the other hand, in approximately 85% of cancer cells, telomerase activity is abnormally overexpressed (Table 1.1), leading to cancer cells that escape cell death and become immortal (e.g. HeLa cells).

It is generally believed that many cancers are caused by mutations in multiple genes that cumulatively avoid the normal growth controls of a cell. The critical steps for a normal diploid human cell to escape from senescence and to develop into an immortalized cancer cell has been proposed to be related to telomere length maintenance by telomerase activation (Figure 1.4).

Shay and Wright have proposed one mechanism for cancer cells to escape the normal cell death control as follows [20]. In a normal human somatic cell with 96 telomeres in total, the presence of only one or a few short (up to approximately 10 reported in [21]) "uncapped" telomeres can trap the cell in mortality stage 1 (M1) and initiate the DNA damage signal leading to growth arrest (also known as replicative senescence) [20]. For

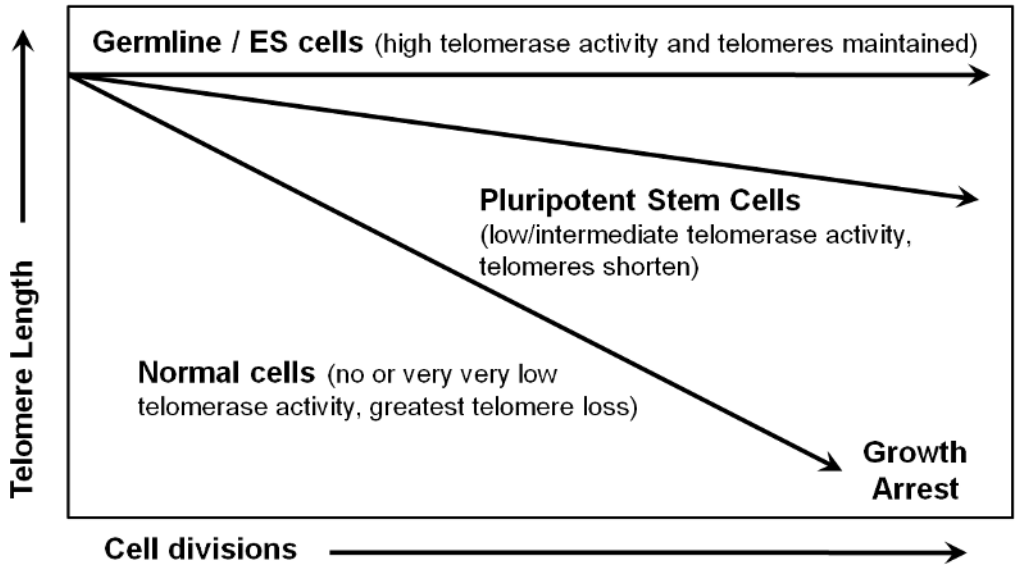

Figure 1.2. Regulation of telomerase. "Only in specific germ-line cells and totipotent embryonic stem (ES) cells does telomerase fully maintain telomere length. In pluripotent stem cells of renewal tissues (e.g., blood, skin and intestine), there is regulated telomerase activity that may help extend the proliferative capacity of these cells. However, these proliferative renewal cells show progressive telomere shortening throughout life. Many tissues and cells have either extremely low levels of telomerase or no detectable telomerase activity, and these cell types may show the greatest rate of telomere loss [17–19]." (Figure is redrawn and caption is taken from J. W. Shay and W. E. Wright. *Telomeres*, chapter *Telomerase and Human Cancer*, pages 84, Cold Spring Harbor Laboratory Press, 2006.)

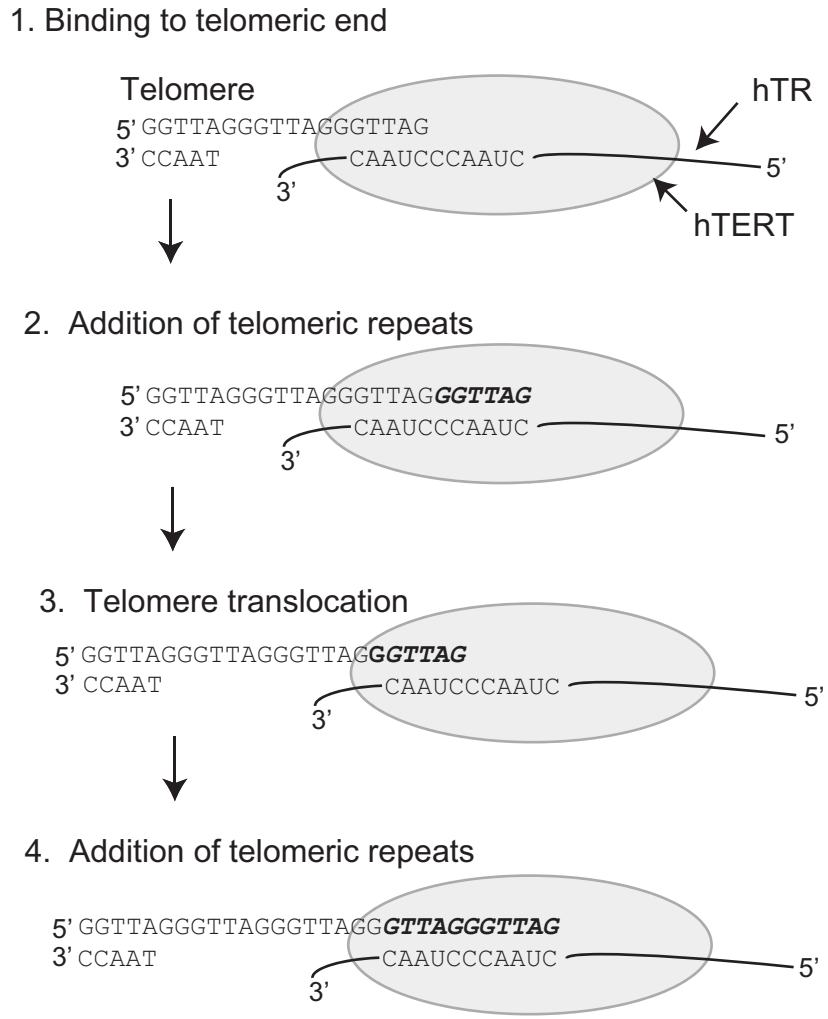

Figure 1.3. Mechanism of telomere elongation by telomerase. The human telomerase is composed of two major components: the human telomerase reverse transcriptase (hTERT, shown as oval) and the internal RNA template (hTR). Step 1: the 3'-end of human telomere binds to part of hTR. Step 2: the reverse transcriptase activity of hTERT extends the telomeric DNA until the end of the template is reached (newly added DNA sequence shown in bold). Step 3: the telomeric end is translocated and repositioned. Step 4: the process is reiterated to add telomeric repeats. (Figure is adapted from Laura K. White, Woodring E. Wright, and Jerry W. Shay. Telomerase inhibitors. *Trends in Biotechnology*, 19(3):114-120, 2001.)

some cells where important cell cycle gene checkpoint genes (e.g. p53, TP53 or pRB) have mutations, however, they ignore this "damage signal" and continue to divide until many more telomeres are critically short. Eventually these cells with extended lifespan will be trapped in mortality stage 2 (M2) and eliminated by apoptosis. Nevertheless in a rare case, a cell can bypass M2 and become immortal, i.e. it has the ability to replicate indefinitely. In order for this special cell to circumvent this telomere-length-based growth limitation, a mechanism for telomere maintenance is required, which appears to be the re-activation and up-regulation of telomerase [22, 23]. In sum, the telomere maintenance by activation of telomerase is essential for the progression of malignancies in most cancer cells.

Another pathway for telomere length maintenance in around 15% of human tumor cells is referred to as alternative lengthening of telomeres (ALT), where telomerase is not activated [24, 25]. The telomeres in the ALT activated cells are heterogeneous in length and a recombination mechanism between telomeric ends is proposed [26].

1.2 Human Telomeric G-quadruplex Conformation–New Target for Anti-cancer Therapy

Given that telomerase is activated in most human cancer and tumor cells but inactive in normal somatic cells, inhibiting the telomere maintenance by telomerase has been proposed as a potential strategy for anti-cancer therapy. Several possible approaches include: (1) inhibitions of telomerase, through either its catalytic or RNA template component [31, 32], or (2) blocking access of telomerase to the telomere, by folding the 3'-end telomeric overhang into the G-quadruplex conformation. Inhibitions of telomerase catalytic activity have been well studied and shown to be effective in attacking the immortality of human cancer cells [33]. However, a few caveats persist, including: (1) a potential delay between the drug intake and cancer cells apoptosis as it may take several cell cycles to deplete the telomeres of cancer cells, and (2) this approach does not target the ALT-activated cancer cells [34]. The second strategy can potentially resolve these problems and has attracted prominent attentions. Large efforts have been made to develop small ligands as potential anti-cancer

Table 1.1. Telomerase activity in samples obtained from malignant tissues [a]

Type of malignancy	No. samples positive/no.tested	% positive
Acute myeloid leukemia	47/64	73
Basal cell carcinoma	73/77	95
Bladder carcinoma	172/185	92
Breast carcinoma (ductal and lobular)	300/339	88
Cervical carcinoma	16/16	100
Chronic myeloid leukemia		
chronic	30/42	71
blast	21/21	100
Colorectal carcinoma	123/138	89
Gastric carcinoma	72/85	85
Head and neck squamous cell carcinoma	112/120	86
Hepatocelluar carcinoma	149/173	86
Lymphoma		
low grade	12/14	86
high grade	16/16	100
Melanoma	6/7	85
Neuroblastoma	99/105	94
Non-small-cell lung carcinoma	98/125	78
Ovarian carcinoma	21/23	91
Pancreatic carcinoma	41/43	95
Prostate carcinoma	52/58	90
Renal carcinoma	95/115	83
Retinoblastoma	17/34	50
Small-cell lung carcinoma	15/15	100
Squamous cell carcinoma	15/18	83

[a] Data are summarized from [27, 28] by J. W. Shay and W. E. Wright. in *Telomeres*, chapter Telomerase and Human Cancer, pages 87. Cold Spring Harbor Laboratory Press, 2006.

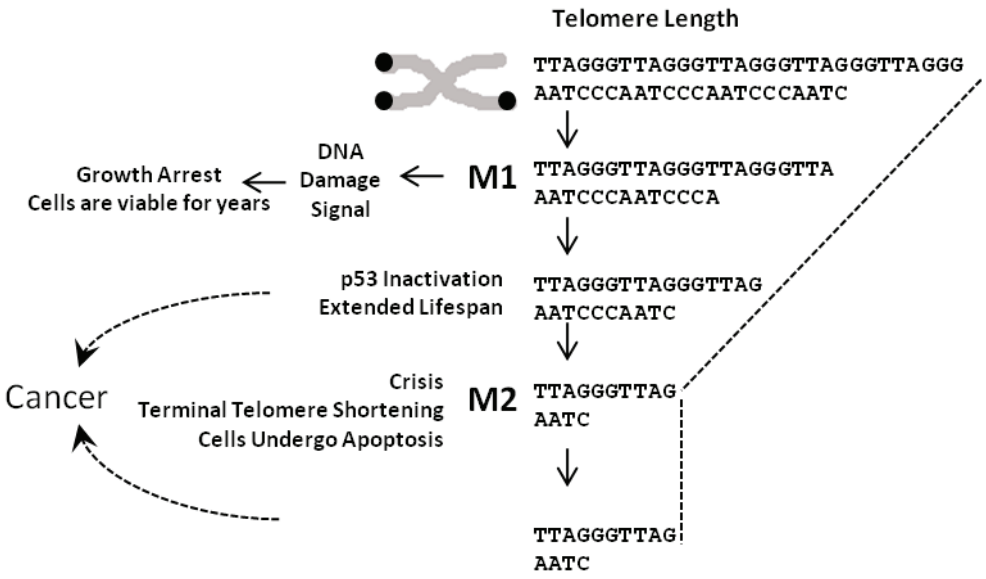

Figure 1.4. Senescence, crisis, and immortalization. "When a few telomeres are short, end associations trigger a DNA-damage signaling pathway leading to a long-term growth arrest (often referred to as replicative senescence, the Hayflick limit, or M1 for mortality stage 1. For cells that have alterations in important cell cycle checkpoint genes (such as p53), they can ignore the DNA damage signal and continue to divide until many telomeres are critically short [29]. There are some instances where the abrogation of M1 senescence can lead directly to the cancer state, but in most instances, cells with extended lifespan will eventually stay in a second growth-arrest state known as crisis or mortality stage 2 (M2). During M2, apoptosis (programmed cell death) almost universally occur. However, in a rare human cell (probability to be about one in ten million cells), there is escape from M2 and immortalization occurrence [20]. This cell has two characteristics, expression of telomerase (Table 1.1) and stabilization of telomeres. This is the common pathway for oncogenic transformation [28, 30]". (Figure is redrawn and caption is taken from J. W. Shay and W. E. Wright. *Telomeres*, chapter Telomerase and Human Cancer, pages 87. Cold Spring Harbor Laboratory Press, 2006.)

drugs by binding and stabilizing the telomeric G-quadruplex conformation. However, the dynamics for the human telomeric G-quadruplex formation under physiological conditions remain unclear.

1.2.1 Background of G-quadruplex DNA Conformation

Unlike the traditional Watson-Crick base pairing found in a double helical DNA sequence, sequences rich in guanine can self assemble to form an alternative structure *in vitro* named the G-quadruplex. Within the quadruplex, several G-tetrads base stack together (Figure 1.5A). Each G-tetrad is a planar structure composed of four guanines, which Hoogsteen base pair with each other (Figure 1.5B). Besides the G-tetrads, there may be loop regions which connect the guanine strands and further stabilize the quadruplex. Depending on the number of oligonucleotides involved in the formation, G-quadruplex conformations can be intramolecular (formed by a single-stranded oligonucleotide), or intermolecular (formed by two or four oligonucleotides strands) (Figure 1.6) [35]. Depending on the direction of the four guanine strands, the quadruplex can be parallel (Figure 1.6C) or antiparallel or a mixture of both. The formation of G-quadruplex *in vitro* needs the presence of cations, usually Na^+ or K^+ [36], which can neutralize the negative charge repulsion between the oxygen atoms in the center of G-tetrad (Figure 1.5).

1.2.2 Guanine-rich sequences prevail in the human genome

Sequencing of the telomeres of different eukaryotic groups has indicated that their tandem repeats are all guanine-rich (Table 1.2) [37–40]. Furthermore, it has been found that guanine-rich sequences (restricted to a minimum of four GGG segments separated by linkers) are prevalent in bacterial and human genomes [41–43]. Up to 3000 putative G-quadruplex-forming motifs have been identified in the human genome [44]. Of these guanine-rich sequences, several are promoter regions located upstream of the transcription starting sites of genes. G-quadruplex formations by these promoter regions are suggested to be involved in gene transcriptional regulation, including *c-myc* [45], *VEGF* [46], *HIF-1α* [47], and *c-kit*

[48].

1.2.3 G-quadruplex formation *in vivo*

Strong evidence supports the formation of G-quadruplex *in vivo*. G-quadruplex formation at telomere proximal regions of chromosomal DNA *in vivo* has been visualized using a quadruplex-specific fluorescence dye, 3,6-bis(1-methyl-4-vinylpyridinium) carbazole diiodide (BMVC) [49]. Additional evidence comes from the observation that telomere end-binding proteins control the formation of G-quadruplex DNA structures *in vivo* [50]. Both inter- and intramolecular G-quadruplex formations have also been demonstrated for the diabetes susceptibility locus in the promoter region of the human insulin gene [51]. Finally, guanine-rich sequences capable of G-quadruplex formation have been shown to induce apoptosis in tumor cells [52, 53].

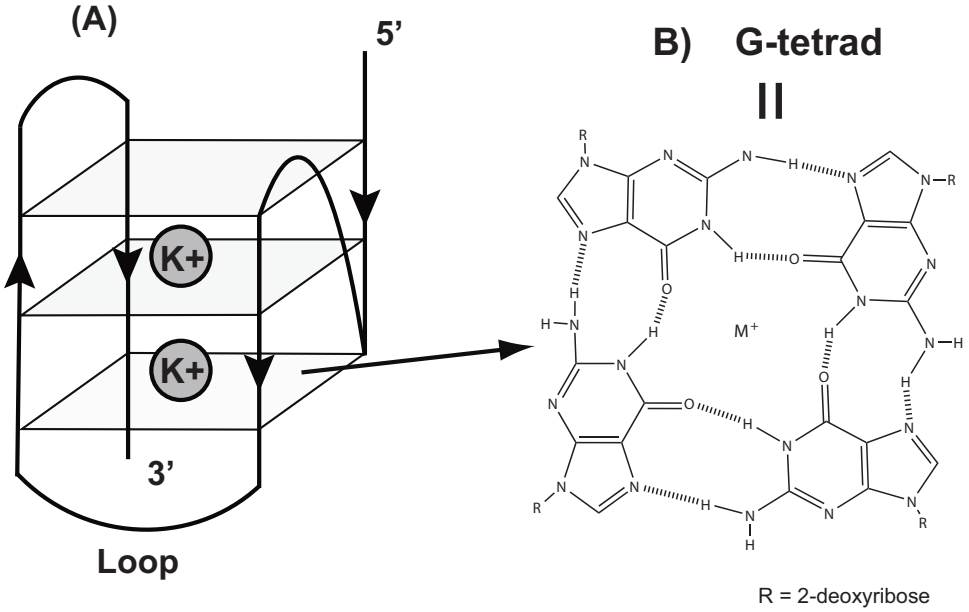

Figure 1.5. (A) Schematic drawing of an intramolecular G-quadruplex stabilized by K^+. Grey diamond shape = G-tetrad. Guanine strand directions are shown by arrows and they can be either parallel or antiparallel to each other. (B) Structure of a G-tetrad composed by four guanines Hoogsteen base pairing with each other and stabilized by the monovalent cations "M^+" (typically Na^+ or K^+).

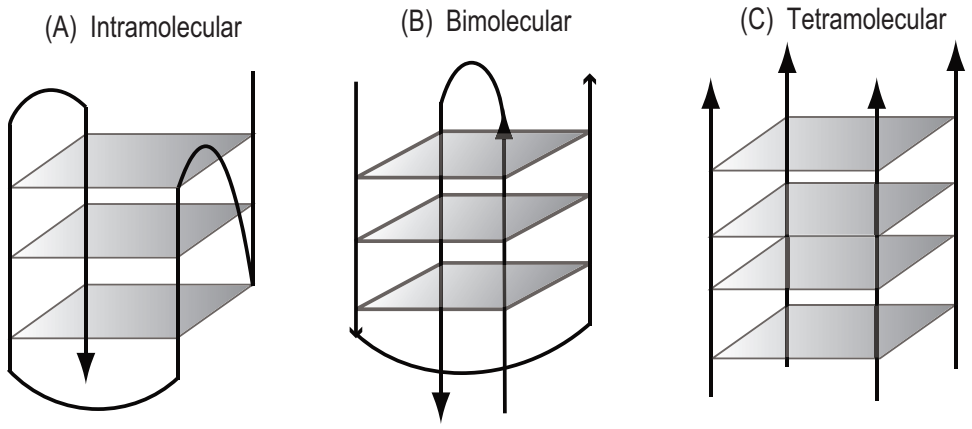

Figure 1.6. Schematic drawing of A)intramolecular B)bimolecular and C) tetramolecular G-quadruplex DNA conformations. Arrows show the 5'– 3' direction.

Table 1.2. Telomeric sequences in different organisms [a]

Group	Organism	Telomeric repeat (5' to 3')	References
Vertebrates	Human, mouse, *xenopus*	TTAGGG	[37]
Filamentous fungi	*Neurospora crassa*	TTAGGG	[38]
Ciliate protozoa	*Oxytricha nova*	T_4G_4	[39]
Budding yeasts	*Saccharomyces cerevisiae*	$T(G)_{2-3}(TG)_{1-6}$	[40]

[a] Complete list of telomeric sequences can be found in the telomerase database *http://telomerase.asu.edu/sequencestelomere.html*.

1.2.4 Intramolecular Human Telomeric G-quadruplex

Four repeats of the guanine-rich telomeric sequence d(TTAGGG)$_4$ (HT_4) can fold into G-quadruplex *in vitro* in the presence of Na^+ and K^+ (Figure 1.5). For the telomerase to elongate the telomeric sequence, a single-stranded 3'-overhang sequence is needed, which base complements the RNA template of the telomerase (Figure 1.3). If the single-stranded sequence folds into the G-quadruplex conformation, the telomeric end becomes a poor substrate for telomerase, elongation may be inhibited and the immortality of cancer cells will cease (Figure 1.7).

During the last decade, great effort has been paid to solve the structures of the human telomeric intramolecular G-quadruplex and to design structure-based small ligands, so called Quadruplex Interacting Agents (QIAs), which promote the quadruplex formation as potential anti-cancer drugs, currently one of which is undergoing clinical trials [54]. The QIA can stabilize the quadruplex by either intercalating with the G-tetrad (as shown in Figure 1.7) or binding to the TTA loop regions.

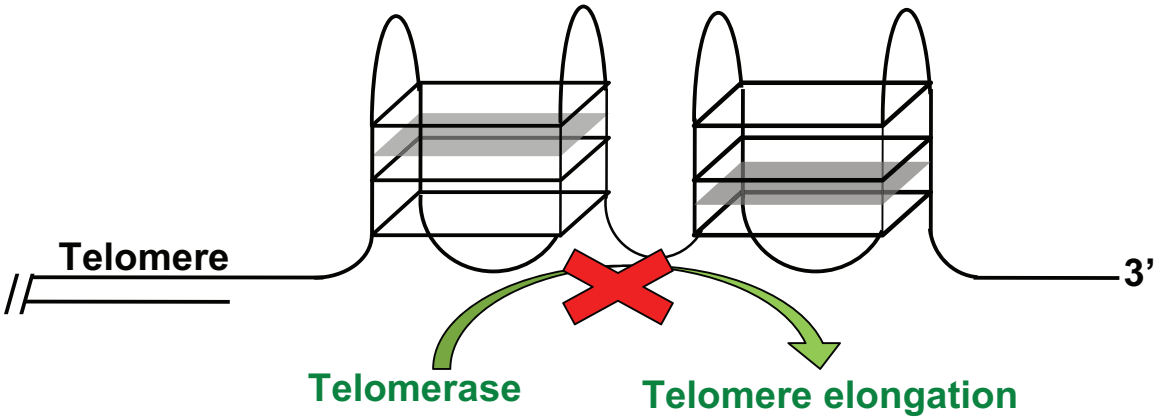

Figure 1.7. Formation and stabilization of the G-quadruplex conformation from the single-stranded human telomeric sequence 5'- (TTAGGG)$_4$-3' can inhibit the telomere elongation activity of enzyme telomerase in tumor cells. White diamond = G-tetrad; Grey diamond = Quadruplex Interacting Agents (QIAs).

1.2.5 Structures of Human Telomeric G-quadruplex

Structures of the intramolecular human telomeric G-quadruplex as solved using NMR or X-ray crystallography are summarized in Table 1.3 [55–58]. As shown in Figure 1.8, these structures differ in their loop topologies, which shows how the TTA loop links two consecutive guanine strands. Three types of loop topologies – lateral, diagonal, and double reversal – have been reported in these quadruplex structures. With different loop topologies, the guanine strand orientations are mixed with parallel and antiparallel in the hybrid-1, hybrid-2 and basket structures, but all parallel in the propeller structure. Furthermore, the glycosidic torsion angle χ on each guanine nucleotide, defined as the dihedral angle in O4′-C1-N9-C4, can be either *anti*(-120$< \chi <$ 180°) or *syn*(0$< \chi <$ 90°) (Figure 1.9). In the propeller model, where all four guanine strands are parallel, each guanine is in *anti* conformation (Figure 1.8C). In the other structures, a mix of *anti* and *syn* guanines are arranged differently at each guanine position.

Table 1.3. Intramolecular human telomeric G-quadruplex structures solvated in Na^+ or K^+

Cation	Structure	Method	DNA sequence(5' to 3')
K^+	Hybrid-1	NMR	AAAGGGTTAGGGTTAGGGTTAGGGAA
	Hybrid-2	NMR	TTAGGGTTAGGGTTAGGGTTAGGGTT
	Parallel	X-ray	AGGGTTAGGGTTAGGGTTAGGG
Na^+	Basket	NMR	AGGGTTAGGGTTAGGGTTAGGG

1.3 Cation effects on G-quadruplex conformation

Before the G-quadruplex DNA conformation was proposed, the strong correlation observed between the melting temperature of guanosine gels and the ionic radii of cations has indicated size-specific ion binding by G-tetrads [59]. Numerous subsequent studies of G-quadruplexes have confirmed the inseparability of G-tetrad formation and cation coordination. The strong interaction between cations and G-tetrads originate from the electro-

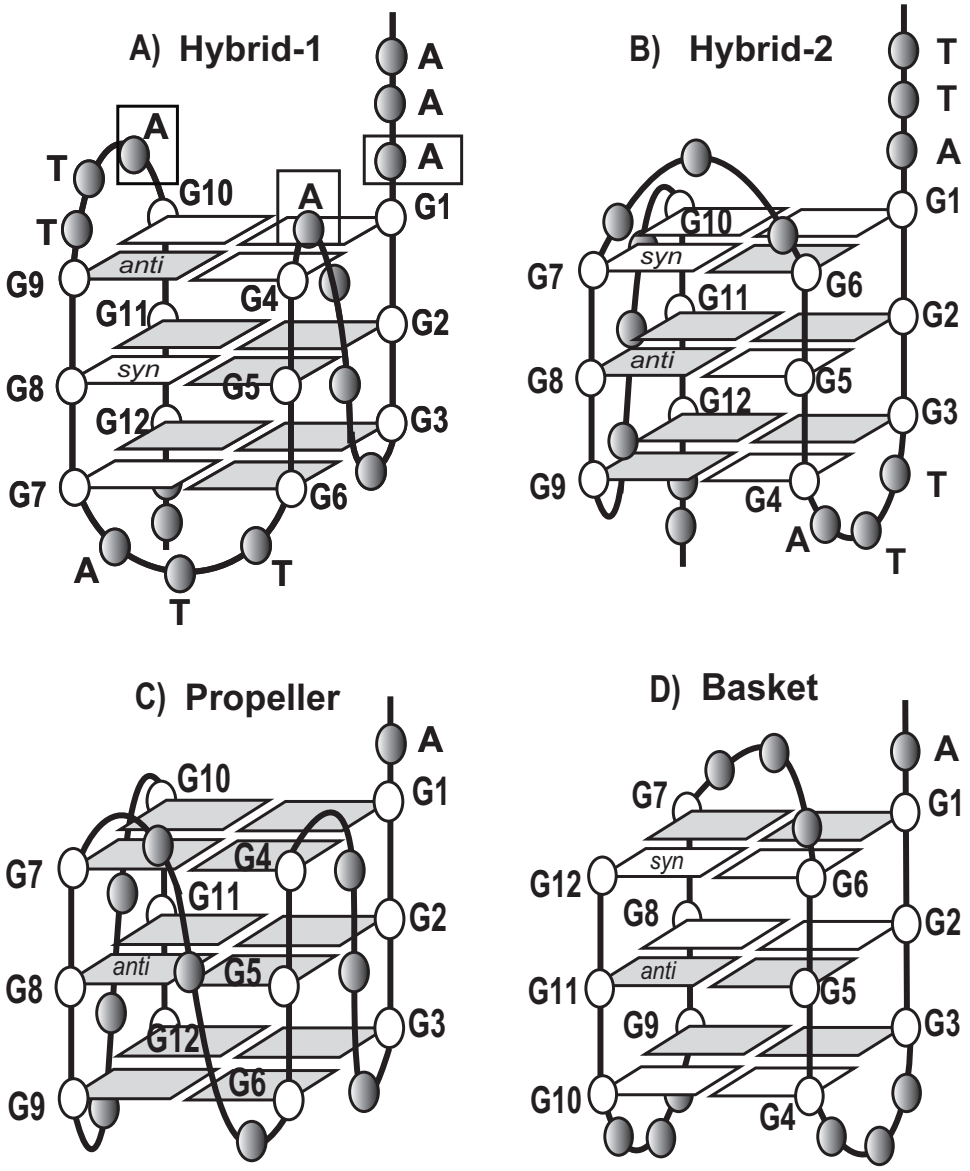

Figure 1.8. Schematic structures of the intramolecular G-quadruplex formed by the human telomeric sequence. (A) Hybrid-1 with double reversal, lateral and lateral loops [55].(B) Hybrid-2 with lateral, lateral and double reversal loops [56]. Both (A) and (B) are solvated in K^+ solution determined by NMR. The triple adenine platform is formed by the three adenine bases (A3, A9 and A21) located above the top tetrad, as highlighted in (A). (C) Propeller with all double reversal loops solvated in presence of K^+ by crystallography [57]. (D)Basket with lateral, diagonal and lateral loops solvated in Na^+ solution by NMR [58]. White circle = guanine; grey circle = adenine or thymine. Grey box = *anti* guanine, white box = *syn* guanine. (Figure is adapted from J. Dai, M. Carver, and D. Yang. Polymorphism of human telomeric quadruplex structures. *Biochimie*, 90(8):1172-83, 2008.)

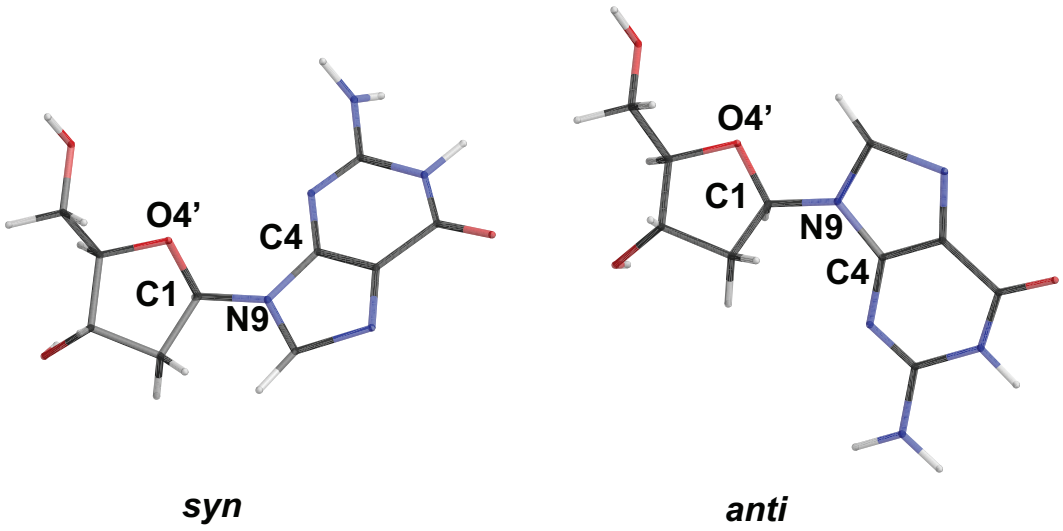

Figure 1.9. Scheme of *syn* and anti glycosidic bond angle of guanosine. The glycosidic bond angle (GBA) χ is defined as the dihedral angle in O4′-C1-N9-C4 and can be *syn* ($0< \chi < 90°$) or *anti* ($-120< \chi < 180°$).

static interactions involving the free electron pairs of the guanine O6 oxygen atoms (Figure 1.5B). However, cation coordination is not restricted to a particular geometry within a G-quadruplex. A series of stacked G-tetrads produces a regular geometry, and potential cation coordination sites, with four O6 atoms within the plane of a G-tetrad, or with eight O6 atoms between two stacked G-tetrads. The K^+ ion (ionic radius 1.33 Å) is too large to coordinate in the plane of a G-tetrad, whereas Na^+ (ionic radius 0.95 Å) is small enough to be coordinated within the plane of a G-tetrad.

The cations entering into the the G-quadruplex and coordinating with the G-tetrads require the cations to be dehydrated [60]. The dehydration energy is inversely proportional to the ionic radius. With its larger ionic radius, the energy cost for K^+ is lower than Na^+. Therefore quadruplex folding in K^+ is thermodynamically more favorable.

1.3.1 Dynamic Polymorphism of G-quadruplex in Solution

With respect to several structural features mentioned above (strand orientation, loop topology, glycosidic torsion angle and type of cations present), the human telomeric G-quadruplex is highly polymorphic. As reported by Li *et al.*, the structure of the human

telomeric G-quadruplex is "not so crystal clear" and "differs from that present in a crystal" in K^+ solution [61]. In Na^+ or K^+ solution, multiple structures of the HT_4 G-quadruplex have been reported in a ^{125}I-radioprobing study [62], a Förster resonance energy transfer (FRET) study [63], a platinum cross-linking study [64], a covalent ligation study [65] and a photon correlation spectroscopic study [65]. Dai *et al.* suggests that the structural polymorphism and dynamic equilibrium of the HT_4 G-quadruplex in solution may result from "the small energy barrier" for interconversion between different forms [66]. Therefore, understanding the conformational dynamics and stability of the HT_4 G-quadruplex under physiological conditions is crucial for better QIA development for anti-cancer therapies.

G-quadruplex formed by the fluorescence labeled HT_4 sequence by substitution using 2-aminopurine (2-AP) or 8-bromoguanine (8-BrG) (Figure 1.10) also showed conformations different from the known structures. 2-AP substituted for the adenine residue can probe the dynamics of the four TTA loop regions on quadruplex folding [61, 67, 68]. The solvent accessibility of 2-AP within the quadruplex in K^+ solution were inconsistent with the parallel model solved in X-ray crystallography (Figure 1.8C). With 8-BrG substituting at varying guanine positions, a novel mixed-parallel/antiparallel and chair-type conformation was suggested for the human telomeric quadruplex in K^+ solution by CD spectroscopy [69]. Single molecule FRET and 8-BrG substitution studies by Okamoto *et al.* further support the discrepancies between the crystal and solution studies of the G-quadruplex conformation [70].

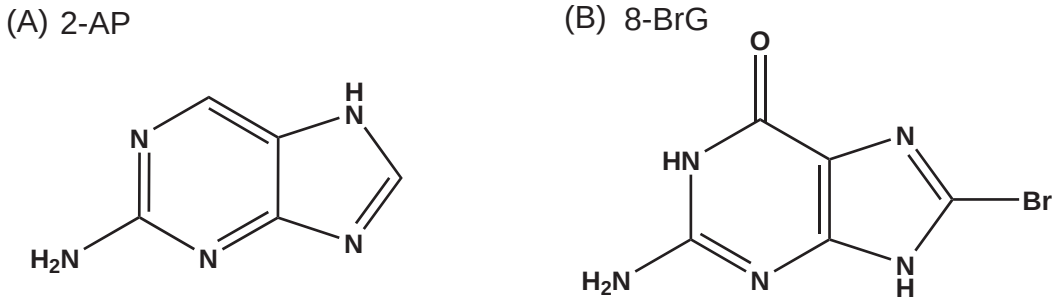

Figure 1.10. Chemical structures of (A) 2-aminopurine (2-AP) and (B) 8-bromoguanine (8-BrG).

1.4 Aims

Previously Gros *et al.* have studied the impact of base substitutions on the kinetics and stability of tetramolecular quadruplex formed by the TG_4T or TG_5T sequence and demonstrated that mutation of guanine positions are deleterious on quadruplex stability [71]. Hurley *et al.* reported that a specific G-to-A mutation leads to destabilization of G-quadruplex formed by the c-MYC gene [72]. Hence, evidence has accumulated that the guanine residues of the tetrad are critical for the stability of the G-quadruplex.

However, with 12 guanines present in the single stranded HT_4 sequence, details identifying the critical guanine residues required for G-quadruplex formation and stabilization remain unclear. In particular there is lack of understanding about folding dynamics of G-quadruplex, and how each guanine residue within the single-stranded sequence contributes to the formation and stabilization of the G-quadruplex.

We hypothesize that each guanine in the HT_4 sequence plays a different role in conformational stability and folding dynamics of the G-quadruplex. Our study aims at examining: (1) the thermodynamic contribution and (2) local dynamics around each guanine residue on folding to the HT_4 G-quadruplex conformation.

To address this aim, we have designed several oligonucleotides with site-specific substitution of individual guanine using a fluorescence guanine analog, 6-methyl-8-(2-deoxy-D-ribofuranosyl) isoxanthopterin (6MI) (Figure 1.11) within the HT_4 sequence. Our nomenclature uses Gn where n indicates the position of the substituted guanine position from the 5'-end, e.g. G5, implies that the fifth guanine of the sequence has been substituted by 6MI. Eight different 6MI-labeled oligonucleotides were used in our study–G1, G2, G4, G5, G7, G9, G11 and G12, as representative guanine positions occupying the top, middle and bottom tetrads. Due to the different loop topologies in G-quadruplex structures, these guanine residues are expected to be located within different G-tetrads (Figure 1.8). However, G2, G5 and G11 are always located on the middle G-tetrad, independent of the change of loop topologies.

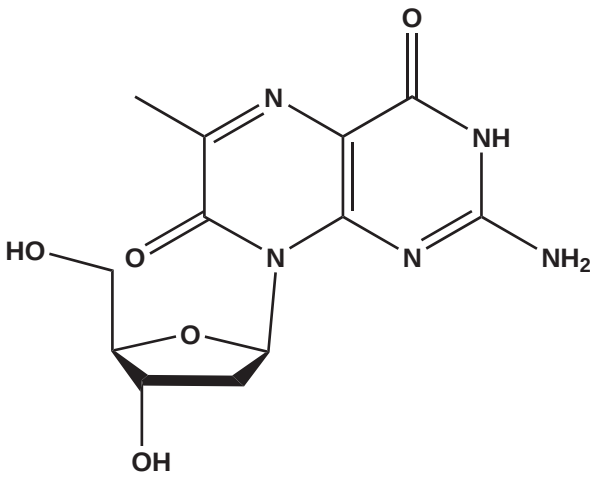

Figure 1.11. Chemical structures of 6MI.

Previously 6MI has been used as an analog of guanine residue to study protein-DNA interaction [73–75] and the kinetics of the tetramolecular TG_4T G-quadruplex [71]. When incorporated into an oligonucleotide, 6MI shows small structural perturbations and high sensitivity to its local DNA environment, especially base stacking interactions with its neighboring bases on the same oligonucleotide [76]. Using 6MI as both a guanine base "mutation" and a probe of its local environment, the folding/annealing transition of the G-quadruplex, exemplified by the spectroscopic properties (absorbance or fluorescence), can be monitored. Thus, the conformational dynamics of the HT_4 G-quadruplex can be better understood.

Mapping the critical guanine positions for their roles in folding and conformational stabilization of G-quadruplex can provide important insights into the future design and development of new QIAs as potential chemotherapeutics with high binding affinity, selectivity and stabilizing abilities for the G-quadruplex structure.

Chapter 2

ROLE OF GUANINE RESIDUES IN GLOBAL STABILITY OF G-QUADRUPLEX

2.1 Introduction

In this chapter we focus on understanding the thermodynamic role each guanine residue plays in the process of HT_4 G-quadruplex formation. This study allows us to map the guanine positions that are critical for maintaining the global stability of the quadruplex, which is of great importance in the design of improved potential anti-cancer drugs that can bind to the folded quadruplex conformation. To accomplish this aim, we used the human telomeric G-quadruplex forming sequence (HT_4) with selective replacement of specific guanine residues by the fluorophore 6MI as an intrinsic probe to map the conformational effects of various guanine residues on global quadruplex stability. First, we confirmed the formation of the G-quadruplex by all the 6MI-labeled sequences in presence of either KCl or NaCl, from the similarity of their characteristic thermal difference spectra (TDS) compared to that of the parent HT_4. Secondly, we examined the global thermodynamic stability of the G-quadruplex formed by each 6MI-substituted sequence. Compared to the parent HT_4 sequence, the thermal unfolding temperatures (melting temperatures) and free energies for folding of the quadruplex are less favorable for each DNA sequence containing 6MI, but to differing extents, which highlights the importance of specific guanine residues on the global quadruplex conformation. We have also investigated the role of the cations, Na^+ or K^+, on the stabilization and formation of the fluorescence labeled G-quadruplex forming sequences.

2.2 Materials and methods

Sample Preparation: The 6-methyl-8-(2-deoxy-D-ribofuranosyl) isoxanthopterin (6MI) and the 6MI-containing oligonucleotides (purity > 95%) were purchased from Fidelity Systems Inc. and used without further purification. All the DNA pellets were reconstituted in standard 10mM cacodylate buffer with or without 100mM KCl or 100mM NaCl at pH 7.2. The buffer pH in our study was adjusted using 1M tetrabutylammonium hydroxide (Fisher Scientific), rather than using NaOH or KOH, which can constitute up to 10mM of the cations in the buffer (measured using atomic absorption spectroscopy, data not shown). The large size of tetrabutylammonium cation precludes its ability to stabilize the quadruplex [67]. Oligonucleotides in the presence of KCl were heated to 80°C for 10 minutes then allowed to cool down overnight to room temperature to facilitate quadruplexed DNA formation.

Thermal difference spectra (TDS): The formation of G-quadruplexes for all oligonucleotides was confirmed using thermal difference spectra. The TDS were obtained by recording the UV-absorbance spectra of the unfolded and folded quadruplex states at temperatures above and below their respective melting temperature (Tm). The spectral difference between these two spectra is the TDS and can provide a unique "signature" for different types of nucleic acid tertiary structure, and all spectra within a structural family are expected to be similar or identical [77]. Therefore, TDS can be used as a tool to confirm the formation of G-quadruplex structures in our studies.

All DNA sequences were prepared as stated above with final oligonucleotide concentrations around 2μM determined spectroscopically at 260nm using extinction coefficients provided by the manufacturer. Each sample was heated from 25°C to 80°C in increments of 1°C and cooled down over the same temperature range and interval. At each temperature the sample was allowed to equilibrate for 3 minutes [78]. UV-absorption spectra of the DNA samples in the standard cacodylate buffer and the buffer alone (no oligonucleotide) were taken over the range 220-340nm using deionized water as the blank, at high temperature ($Abs(\lambda, T_{high})$; typically 80°C) and low temperatures ($Abs(\lambda, T_{low})$; typically 20°C). Cacodylate buffer was not used as the spectroscopic blank because of its increased absorbance around

220nm upon heating.

Absorbance spectra of DNA at the lower and higher temperatures T (20°C or 80°C) were obtained by subtracting the absorbance of the buffer from absorbance of the DNA at each wavelength λ:

$$Abs(\lambda, T) = Abs_{DNA}(\lambda, T) - Abs_{Buffer}(\lambda, T) \tag{2.1}$$

Difference spectral curves were obtained from the arithmetic difference of absorbance values between high (80°C) and low (20°C) temperatures after correction for any buffer absorption.

$$\Delta Abs(\lambda) = Abs(\lambda, T_{high}) - Abs(\lambda, T_{low}) \tag{2.2}$$

In order to facilitate the comparison of all the spectral signatures, all spectra were normalized by dividing the raw data ($\Delta Abs(\lambda)$) by the maximum value across the entire wavelength range (ΔAbs_{max}), so that the highest positive peak is assigned a Y-value of +1. The final thermal difference spectra (TDS) were plotted as the normalized ΔAbs *versus* wavelength λ.

$$\text{Normalized } \Delta Abs(\lambda) = \Delta Abs(\lambda)/\Delta Abs_{max} \tag{2.3}$$

UV Absorbance Thermal Melting (Unfolding) Studies: To determine the overall global effects caused by substitution of specific guanine bases by 6MI, the thermal melting temperatures (Tm) for the substituted oligonucleotides were measured using UV-spectroscopy in 100mM KCl or NaCl cacodylate buffer. When the single-stranded modified telomeric DNA sequence folds to the tertiary-structured G-quadruplex, a hyperchromism, or increase of absorbance, around 285-305nm can be detected in the absorbance spectra. For melting studies, the wavelength of 295nm was used because it is where absorbance of the G-quadruplex decreases most as it unfolds [79] – and is also the minimum in the TDS at 295nm (Figure 2.2). Therefore the melting or annealing of the G-quadruplex structure can be monitored spectrophotometrically, and its Tm and thermodynamic values associated

with folding or unfolding can be extracted, by recording the reversible absorbance changes at 295nm during the heating or cooling process, respectively.

The Tm of 2μM quadruplex-DNA (with or without fluorophore) in different concentrations of KCl (from 0mM to 100mM) was determined by monitoring the absorbance hyperchromacity at 295nm using an HP 8452A Diode Array Spectrophotometer, equipped with an HP Peltier temperature controller, quartz cuvettes (1cm path length), and 845x UV-Visible System software. The samples were heated from 15°C to 90°C, with a ∼3min incubation time for each 1°C temperature increment [78]. To avoid evaporation of the buffer, the cuvette was tightly sealed using a Teflon plug.

Determination of Tm values: The "melting" temperatures (Tm) for the unfolding of the DNA quadruplex were determined based on analysis method described previously in [80]. Figure 2.1A shows a typical experimental quadruplex DNA melting profile, with measured absorbance values at 295nm *versus* temperature. To correct for the sloping baselines, melting curves at low and high temperatures were fitted to linear lines ($B(T) = y_0 + aT$) using Sigmaplot 10.0 (Systat Software, Inc.). Assuming the melting transition follows a two-state model (with only folded and unfolded states present), the fraction of folded $\alpha(T)$ at temperature T was calculated from

$$\alpha(T) = \frac{B_U(T) - A(T)}{B_U(T) - B_F(T)}, \tag{2.4}$$

where $A(T)$ is the measured intensity value (which may be absorbance or fluorescence), and $B_U(T)$ and $B_F(T)$ are the unfolded and folded baseline values, respectively, at temperature T. The melting temperature (Tm) is the temperature at the mid-point of the transition, where α equals to 0.5 (Figure 2.1B). This approach for determining Tm values was adopted over the usual first-derivative Tm determination, due to the sloping baseline issue. As suggested by Mergny *et al.* [78], first-derivative determined Tm values from samples with temperature-dependent baselines do not exactly correspond to the true Tm, especially when dealing with broad and cooperative melting transitions [81].

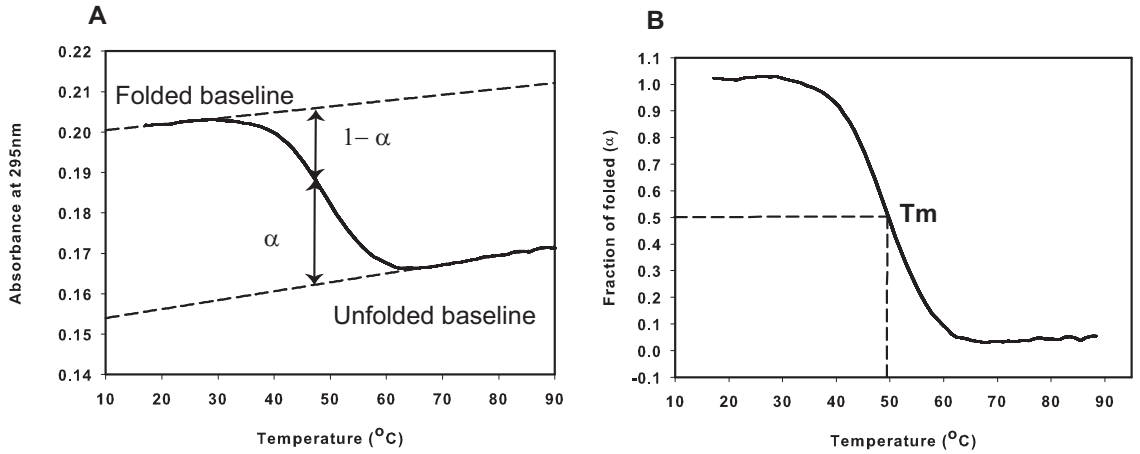

Figure 2.1. Determination of the fraction of G-quadruplex folded from thermal melting profiles. (A) Melting curve obtained from absorbance values *versus* temperature. The baselines for folded (at low temperature) and unfolded (at high temperature) states were fitted to linear sloping lines and extrapolated to higher and lower temperatures. (B) The fraction of folded quadruplex α is derived from data shown in (A). The melting point (Tm) corresponds to the temperature where α is 0.5.

Thermodynamic Analyses from Melting Studies: Since the fraction of folded quadruplex α is determined based on the all-or-none folding model for the melting transition, the equilibrium folding constant K for intramolecular quadruplex formation at each temperature T can be calculated from

$$K(T) = \frac{\alpha}{1-\alpha}, \tag{2.5}$$

where α falls in the range of $0.04 - 0.96$. The temperature-independent van't Hoff enthalpy and entropy changes (ΔH and ΔS, respectively) can then be determined according to the equation:

$$-RlnK(T) = \Delta H/T - \Delta S \tag{2.6}$$

Plotting $lnK(T)$ *versus* $1/T$ provides the values for ΔH and ΔS from the slope and the intercept, respectively. Free energies of quadruplex formation at 37°C and 20°C were calculated using the Gibbs equation: $\Delta G = \Delta H - T\Delta S$.

2.3 Results and discussions

A key issue when using 6MI as a fluorescence probe for studying conformational dynamics at locations for specific guanine residues, is to ensure that substitution by this guanine analog does not appreciably affect or perturb the HT_4 sequence from forming the native G-quadruplex structure. Other studies have shown that a single guanine mismatch within the DNA sequence can disrupt the quadruplex formation [71, 72]. However, the 6MI substitutions on the HT_4 oligonucleotide in our studies are less invasive to the quadruplex conformation, since the 6MI can Hoogsteen base pair with other neighboring bases to form the G-tetrad. To test for structural integrity and stabilities of G-quadruplexes formed by all 6MI-labeled sequences, we obtained both thermal difference spectra (TDS) [77] and UV-melting profiles [78, 79], and compared them with the G-quadruplex formed by the parent (unlabeled) sequence HT_4, which served as the positive control.

2.3.1 Quadruplex formation by 6MI-labeled HT_4 sequence

In the presence of 100mM KCl, the TDS spectra for the 6MI-labeled sequences are similar to the parent HT_4, with major positive absorption difference peaks at around 244nm and 272nm, a positive shoulder around 256nm and a minimum at 295nm (Figure 2.2A), which are characteristic of a hybrid quadruplex conformation reported previously [77]. In the presence of 100mM NaCl, characteristic absorption difference spectra were observed for six out of the eight labeled sequences: G2, 4, 5, 9, 11 and 12 (Figure 2.2B), which compared favorably with the parent HT_4 sequence. In general, the formation of the G-quadruplex structure stabilized in the presence of either Na^+ or K^+ cations is not significantly affected by 6MI substitution in the HT_4 sequence at these specific guanine positions, and suggests that these sequences can serve as appropriate models for G-quadruplex conformation and dynamic studies.

Differences in the TDS for the parent unlabeled HT_4 oligonucleotide in presence of Na^+ *versus* K^+ are most obvious around 245nm, where the normalized ΔAbs values appear

lower in the presence of Na^+ compared to that in K^+ cation (Figure 2.3A). The TDS difference at 245nm in the presence of differing cations has been attributed to G-quadruplex conformational affects, with the antiparallel basket quadruplex prevalent in Na^+ *versus* the mixed-hybrid quadruplex in K^+ [77]. Interestingly, the TDS spectra observed for the G1 and G7 sequences in the presence of Na^+ cation gave signatures very close to those which would ordinarily be observed in KCl (Figure 2.3B and C). These data suggest that in NaCl buffer, the G-quadruplexed conformations adopted by the G1 and G7 substituted oligonucleotides may prefer a mixed-hybrid conformation (normally seen in the presence of K^+ cations). For labeled position G7, this may reflect relief of potential strain resulting from the diagonal loop linking positions G6 and G7 in the basket conformation in NaCl (Figure 1.8 page 15).

As discussed in section 1.3 in Chapter 1, K^+ cations are able to better stabilize the G-quadruplex conformation over Na^+-ions. Thus 6MI substitutions at positions G1 and G7 in 100mM NaCl buffer are better tolerated by promoting a G-quadruplex conformational switch (to a mixed-hybrid conformation), resulting in observed higher Tm and more favorable $\Delta G_{folding}$ values than measured for other 6MI-labeled sequences in NaCl buffer (as discussed below).

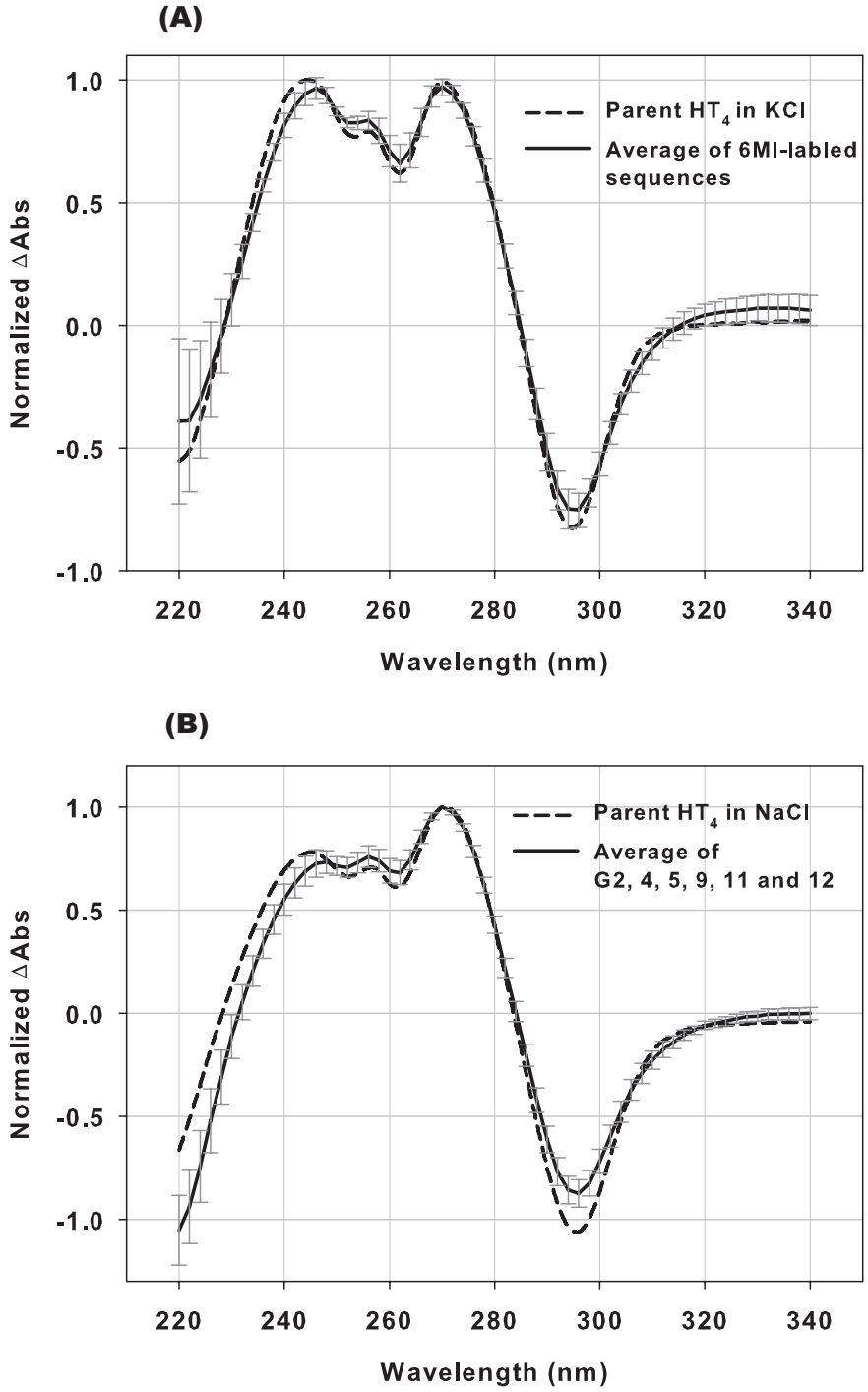

Figure 2.2. Thermal difference spectra in 10mM cacodylate (pH 7.2) with (A) 100mM KCl and (B) 100mM NaCl for unlabeled parent HT_4(broken line) and the average ($\pm$ standard deviation) spectrum for 6MI-labeled sequences (solid line). The average curve was calculated from all eight 6MI-labeled sequences (G1, 2, 4, 5, 7, 9, 11 and 12) in (A), and excludes G1 and G7 in (B). Differences of absorbance between unfolded and folded state were normalized to the range of -1 to $+1$.

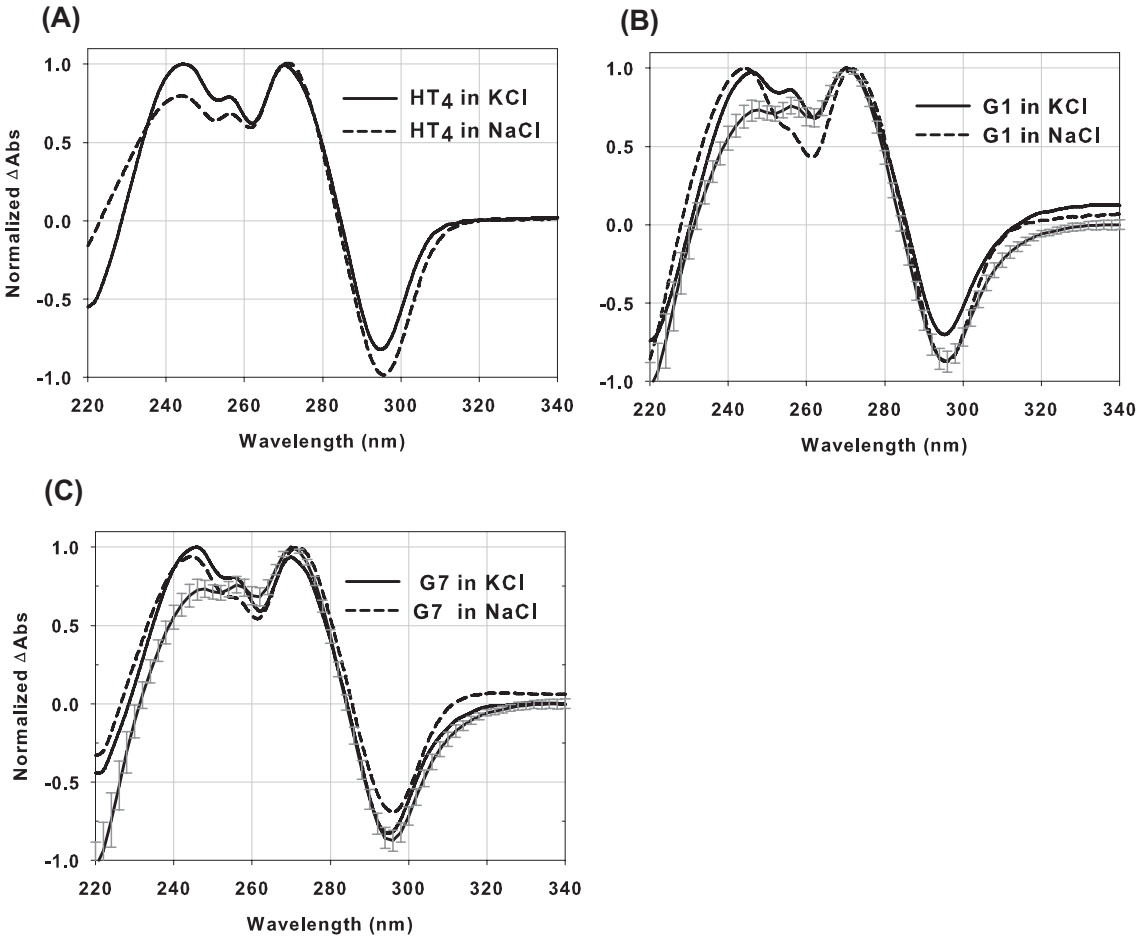

Figure 2.3. Thermal difference spectra of (A) parent in HT_4, (B) G1 and (C) G7 in 10mM cacodylate (pH 7.2) with 100mM either KCl (solid line) or NaCl (broken line), compared to the average TDS 6MI labeled sequences (G2, 4, 5, 9, 11 and 12) in 100mM NaCl shown in Figure 2.2B. Compared to the parent HT_4, the TDS of G1 and G7 in 100mM NaCl (broken lines) appear more similar to those observed in KCl (solid line).

2.3.2 Thermal melting points of 6MI-labeled G-quadruplex sequences in presence of 100mM KCl or NaCl

To examine how the single guanine "mutation" within the HT_4 sequence affects the global stability of the G-quadruplex, we measured the thermal melting temperatures for the unfolding of quadruplex structures formed from the parent/unsubstituted HT_4 and the 6MI-labeled sequences (G1, 2, 4, 5, 7, 9, 11 and 12) in 100mM KCl or NaCl. Table 2.1 and Figure 2.4 summarize the data. In general, Tm values are higher in 100mM K^+ (ranging from 47.7 to 61.9°C) than in 100mM Na^+ ($33.5 - 50.4$°C), reflecting the enhanced stability of the mixed-hybrid K^+-stabilized quadruplex conformation in solution over the antiparallel basket Na^+-conformation.

For each 6MI-labeled sequence, in the presence of either alkali cation, the melting points are lower than for the corresponding parent HT_4 sequence (61.9°C in K^+ and 49.1°C in Na^+), suggesting that substitution of guanine by 6MI within the sequence reduces global conformational stability of G-quadruplex, although the quadruplex conformation is preserved.

However, thermal melting/unfolding temperatures (Tm) for the 6MI-substituted sequences differ from the parent HT_4 to varying extents. Comparison of Tm values can provide insights into how specific guanine positions contribute to the overall thermal quadruplex stability. If one guanine position is critical for stabilizing the entire quadruplex structure, its Tm value can be greatly affected and *vice versa*.

In 100mM K^+, Tm values for the oligonucleotides follow the order:

$$HT_4 > \boxed{\text{G1}\sim\ \text{G5}\sim\ \text{G7}} > \boxed{\text{G2}\sim\ \text{G4}\sim\text{G11}} > \boxed{\text{G9}\sim\ \text{G12}}.$$

The highest Tm values (reflecting a greater degree of stability, although still less than the parent unlabeled sequence) were observed (∼54°C) when positions G5, G7 and G1 were substituted, followed by G4, G2 and G11 (∼51°C), and lowest (least conformationally stable) for G9 and G12 (∼48°C). Given the variability of the thermal stabilities for 6MI substitutions at different positions, this lends weight to our hypothesis that different guanine positions of the quadruplex can play different roles in the formation and stabilization of the

G-quadruplex.

Interestingly, substitution at positions G1 (5'-end) and G7 (next to the second loop) as discussed above, are better tolerated than replacement at positions G9 (next to the third loop) and G12 (located at the 3'-end) of the telomeric sequence. Previously Dai *et al.* have suggested that the "adenine triple platform", formed by the three adenines – A3, A9 and A21 (Figure 1.8), plays an important role in formation and maintenance the stability of the hybrid G-quadruplex conformation in K^+, by capping and protecting the top G-tetrad [55]. In our study, the 6MI substitution at guanine position G1 located near the 5'-end results in higher Tm, and thus is better accommodated than near the 3'-end (G12). Hence, the 5'-end flanking adenine involved in forming the "adenine triple platform" appears to minimize any destabilizing effects arising from 6MI substitution at position G1, which is absent at the 3'-end.

Positions G2, G5 and G11 are all located within the center tetrad of the G-quadruplex (Figure 1.8 on page 15). However, global Tm values for positions G2 and G11 are lower than for G5. This suggests that 6MI substitution at guanine positions 2 and 11 located near the terminal oligonucleotide ends perturb the global stabilities of the quadruplex more severely than the internal G5 position. Therefore, the middle-tetrad guanines 2 and 11 by virtue of their potential fraying nature near the terminal ends appear to play a significant role in maintaining the overall stabilization of the quadruplex.

G4, G7 and G9 are all located near TTA loop regions, but their Tm values appear substantially distinct (G7 > G4 > G9). The difference may result from their different (*syn versus anti*) glycosidic bond angles (GBA) and the strain on the loops, with G9 participating in a possibly more strained in-face diagonal loop *versus* the end loops for G4 and G7 for the hybrid-2 conformation. In addition, Gros *et al.* have suggested that 6MI modification at guanine positions with *syn* GBA are more favored than *anti* [71]. As shown in Figure 2.5B, the proximity and the possible electrostatic repulsion between the O7 and the O' may attribute to less stability for the *anti* 6MI than the *syn*. Hence, when 6MI is substituted into guanine positions with the *syn*-GBA, possible structural perturbations of the overall

conformational stabilization of the quadruplex can be better tolerated over the *anti*-GBA. For the hybrid-1 or hybrid-2 G-quadruplex formed in the presence of K^+-ions (Figure 1.8A and B on page 15), both G4 and G7 have the *syn* glycosidic bond angle, while G9 has the *anti* GBA. Hence, mutation or alteration at the *anti*-guanine G9 appears more destructive to the HT_4 quadruplex than substitution at *syn* G4 and G7; G9 is a critical guanine for productive quadruplex formation. Similar trends were also observed in the fluorescence melting study discussed in Chapter 3.

With 100mM Na^+ present, the order of Tm values changes to:

$$\boxed{\text{G7}\sim\text{HT}_4}>\text{G1}>\text{G12}>\boxed{\text{G4}\sim\text{G9}}>\boxed{\text{G2}>\text{G5}\sim\text{G11}}.$$

The altered Tm values measured in the presence of Na^+-ions appear to be related to the particular G-tetrad where the substituted guanines are located within the antiparallel basket quadruplex conformation (basket model shown in Figure 1.8D on page 15). Guanines 1, 7 and 12, which are located within the top G-tetrad result in the highest Tm values (most stable), followed by G4 and G9 on the bottom tetrad, and lowest (least stable) for G2, 5 and 11 within the center tetrad.

In the native Na^+-stabilized basket quadruplex conformation (Figure 1.8 on page 15), guanine 7 is located next to the only diagonal loop and on the same top G-tetrad as G1, which both have the *anti* glycosidic bond angle (GBA). It is interesting to note that with switching cations from K^+ to Na^+, the Tm values for G1 and G7 substituted quadruplex sequences both exhibited a decrease, but less than measured for the parent HT_4 sequence, as shown by the values of $\Delta T_{m(K^+-Na^+)}$ in Table 2.1. One possible explanation is that the 6MI substitutions at these two positions can promote the glycosidic bond angle on the base from *anti* to *syn*, resulting in the switching of the quadruplex conformation from an antiparallel basket conformation. These data support the TDS data described previously. Therefore, it appears that guanine bases located within positions 1 and 7 of the telomeric oligonucleotide may be described as "key players" and appear to be involved in promoting a conformational switching to a K^+-ion stabilized conformation when substituted within the sequence in the presence of Na^+-ion, rendering a more stable quadruplex conformation.

On the other hand, guanine substitutions at positions G2, G5 and G11 located within the middle tetrad and stabilized by the Na^+-ion, have the lowest Tm values, suggesting that these guanine positions strongly interact with the Na^+ cations and are key in stabilizing the Na^+-induced basket quadruplex conformation.

Table 2.1. Absorbance melting temperatures (Tm) for G-quadruplexes by human telomeric sequences in presence of 100mM KCl or NaCl

Sequence	Tm (°C)[a]		$\Delta T_{m(K^+-Na^+)}$(°C)[b]
	In 100mM K^+	In 100mM Na^+	
HT_4	61.9	49.1	12.8
G1	53.7	45.0	8.7
G2	51.2	36.7	14.2
G4	51.5	38.4	13.1
G5	54.1	34.6	19.5
G7	54.0	50.4	3.6
G9	48.4	37.5	10.9
G11	50.5	33.5	17.0
G12	47.7	41.6	6.1

[a] Tm values were extracted using the analysis described on page 23. Buffer was 10mM cacodylate (pH 7.2) with 100mM KCl or NaCl.

[b] $\Delta T_{m(K^+-Na^+)}$ is the difference in melting points between the same sequence in different cation (100mM KCl and NaCl).

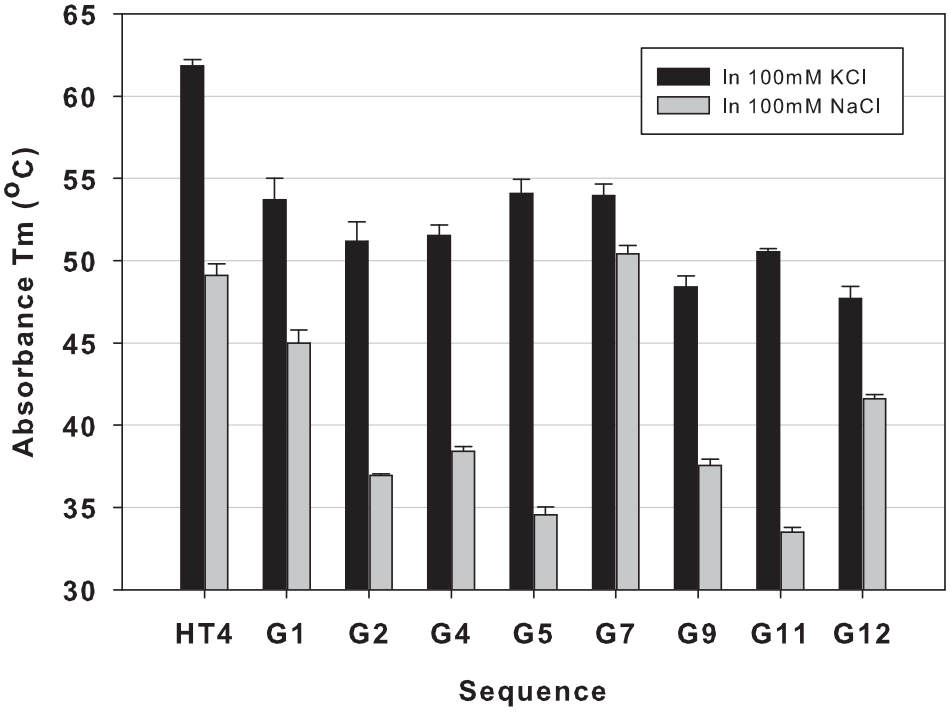

Figure 2.4. Absorbance melting temperatures (Tm) for G-quadruplexes formed by HT_4 and each 6MI-labeled oligonucleotide in presence of 100mM KCl or NaCl. Data are from Table 2.1 with standard deviations for three trials.

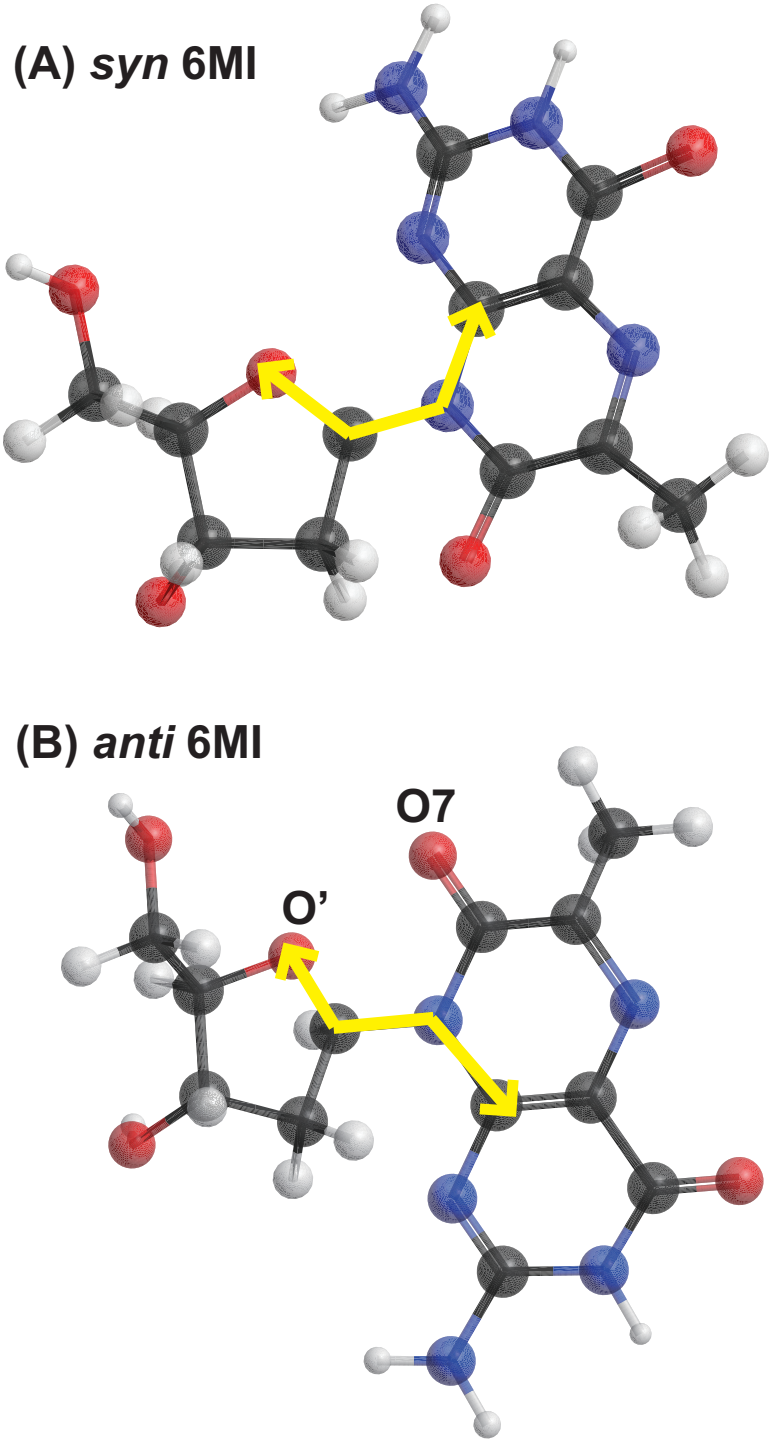

Figure 2.5. 6MI with (A) *syn* or (B) *anti* glycosidic bond angle, which is defined as the angle between the two yellow arrows. 6MI with the *anti* glycosidic bond angle will be less stable due to the repulsion between the two oxygen atoms O' and O7. Carbon, hydrogen, nitrogen and oxygen atoms are represented using black, white, blue and red balls, respectively.

2.3.3 Thermodynamic stability of 6MI-labeled G-quadruplex

To quantify the effects of 6MI substitution at varying guanine positions on the overall global thermal stability of the G-quadruplex, the Gibbs free energies for quadruplex formation ($\Delta G_{folding}$) were determined from the UV absorbance unfolding/melting studies, under physiological conditions (37°C in either 100mM KCl or NaCl (pH 7.2)). Figure 2.6 summarizes the calculated ΔH and $T\Delta S$, and Figure 2.7 shows the corresponding $\Delta G_{folding}$ at 37°C in 100mM KCl or NaCl. A more negative $\Delta G_{(fold,37°C)}$ value for indicates a more stable G-quadruplex. In general, the quadruplex folding in 100mM KCl is an enthalpy-driven process for each sequence, with a more negative value for ΔH over $T\Delta S$, as shown in Figures 2.6A. Under physiological conditions, the conformational stabilities ($\Delta G_{(fold,37°C)}$) of the 6MI substituted G-quadruplexes formed by the DNA sequences with varying monovalent cations follow the order:

$$\mathrm{HT_4} > \mathrm{G5} > \mathrm{G1} > \boxed{\mathrm{G2{\sim}G4}} > \mathrm{G7} > \mathrm{G11} > \mathrm{G12} > \mathrm{G9}\ \text{(in 100mM KCl)},$$

and

$$\mathrm{HT_4} > \mathrm{G7} > \mathrm{G1} > \mathrm{G12} > \boxed{\mathrm{G4{\sim}G9}} > \boxed{\mathrm{G2{\sim}G5{\sim}G11}}\ \text{(in 100mM NaCl)}.$$

In general for 100mM KCl conditions, the order of $\Delta \mathrm{G}_{(fold,37°C)}$ values for the 6MI-labeled oligonucleotides were similar to the ordering of Tm values. Interestingly, for the G2, G5 and G11 substituted guanine positions in 100mM NaCl (Table 2.1), the quadruplex sequences were not fully folded at 37°C, and their corresponding ΔG values are positive (Figure 2.7B). Only the control (no guanine replacement) and positions G1, G7 and G11 demonstrate quadruplex folding; as discussed previously, alteration of these positions appears to promote a conformational switch to a hybrid-like conformation. Thus, under physiological 37°C conditions, the Na^+-stabilized quadruplex conformation is expected to be less stable than for the corresponding K^+-stabilized conformation, and alteration or perturbation around any of the guanine positions can lead to quadruplex unfolding. Hence, it is anticipated that the K^+-ion stabilized mixed-hybrid will be the prevalent quadruplex cellular conformation in a cellular environment at physiological temperatures.

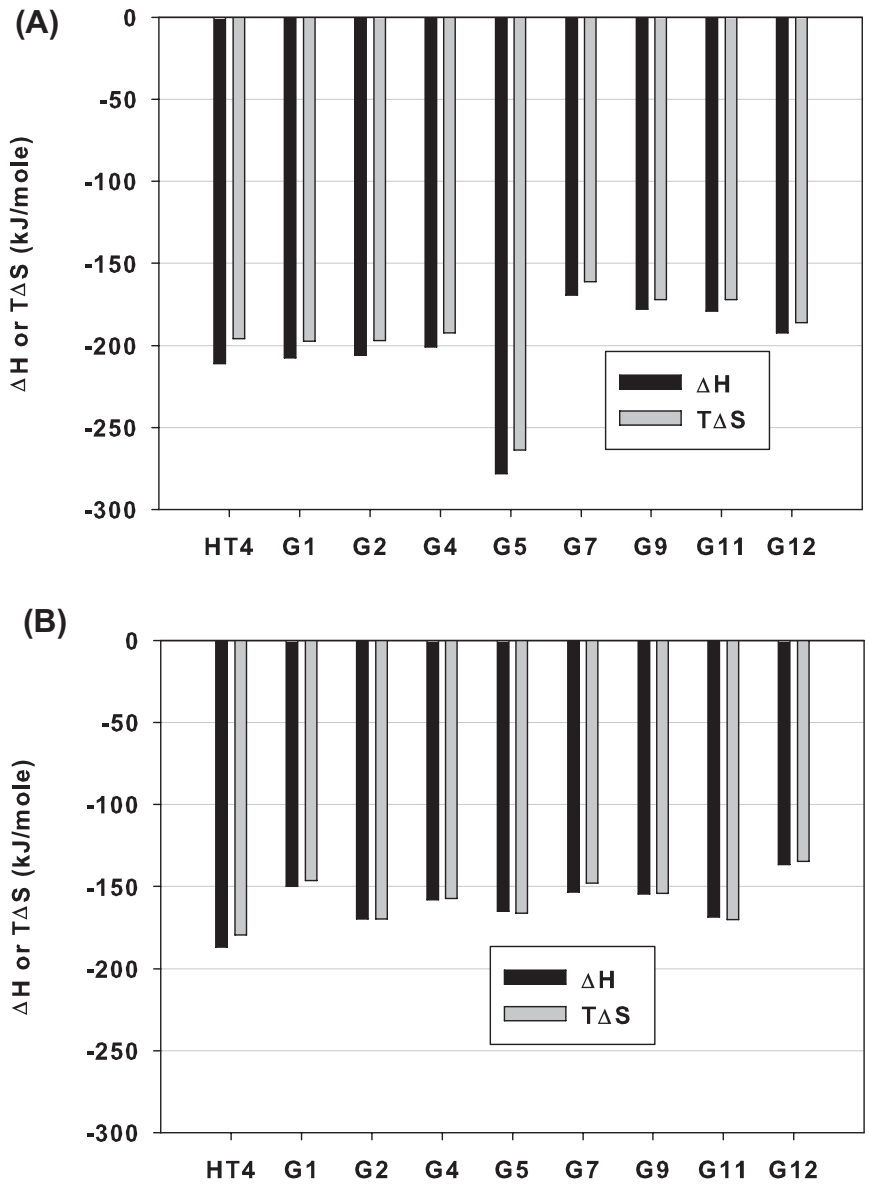

Figure 2.6. Enthalpy (ΔH) and entropy (TΔS) contributions for folding of quadruplex at 37°C in (A) 100mM KCl and (B) NaCl.

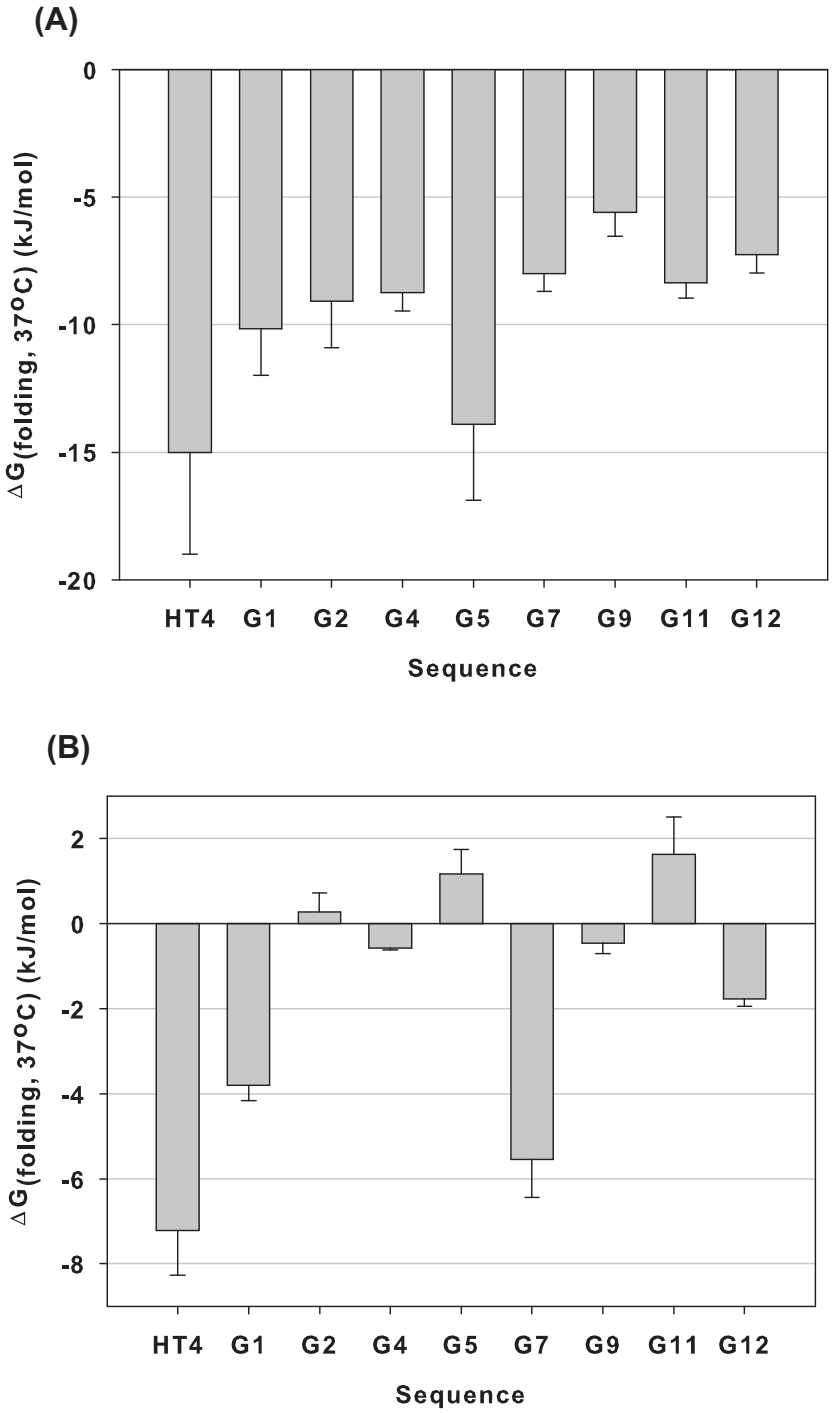

Figure 2.7. Gibbs free energy for folding of quadruplex at 37°C in (A) 100mM KCl and (B) NaCl. Gibbs free energy (ΔG) for folding in Figure 2.7 is calculated from $\Delta G = \Delta H - T\Delta S$.

To better compare the spontaneity for quadruplex folding among these 6MI-labeled sequences, we also obtained the ΔG values for folding at 20°C (Figure 2.8) in the presence of Na^+-ions. The free energy values at 20°C follow the order:

$$HT_4 > G7 > G1 > \boxed{G2{\sim}G4{\sim}G9{\sim}G12} > \boxed{G5{\sim}G11} \text{ (in 100mM NaCl at 20°C).}$$

At 20°C in presence of Na^+-ions, the quadruplex conformation by each sequence is promoted, with free energy values of folding more favorable than for the corresponding value at 37°C. In addition, the free energies of folding are consistent with the order of Tm values (shown above) in the presence of 100mM NaCl. Again, substitution at positions G1 and G7 are thermodynamically more stable and tolerated over the other 6MI-labeled sequences.

2.4 Summary

TDS studies have confirmed that the G-quadruplex conformation can be formed in 100mM KCl or 100mM NaCl at 20°C, with single guanine residue substitutions by the 6MI fluorophore along the HT_4 sequence.

We also examined the global stability (Tm and $\Delta G_{folding}$) of the quadruplex conformations formed by 6MI-substituted oligonucleotides and compared these parameters to the unlabeled parent HT_4. In general, the Tm value of each labeled sequence is lower than for the parent HT_4, suggesting the 6MI substitution within the oligonucleotide results in some degree of perturbation to the quadruplex conformational stability. However, the extents to which Tm and $\Delta G_{folding}$ vary for the 6MI-labeled sequences suggest that different guanine positions of the quadruplex play distinct roles in the formation and stabilization of the G-quadruplex, which is relevant for the development of potential quadruplex interactive agents.

The 6MI substitution sites based on their locations within the Na^+-induced basket and K^+-induced hybrid-1 quadruplex are shown in Figure 2.9. In 100mM KCl buffer, G1 substitution (green circle in Figure 2.9A) near the 5'-end offers a greater stability (higher Tm value) than observed for G12 substitution on the 3'-end. This preferential stabilization

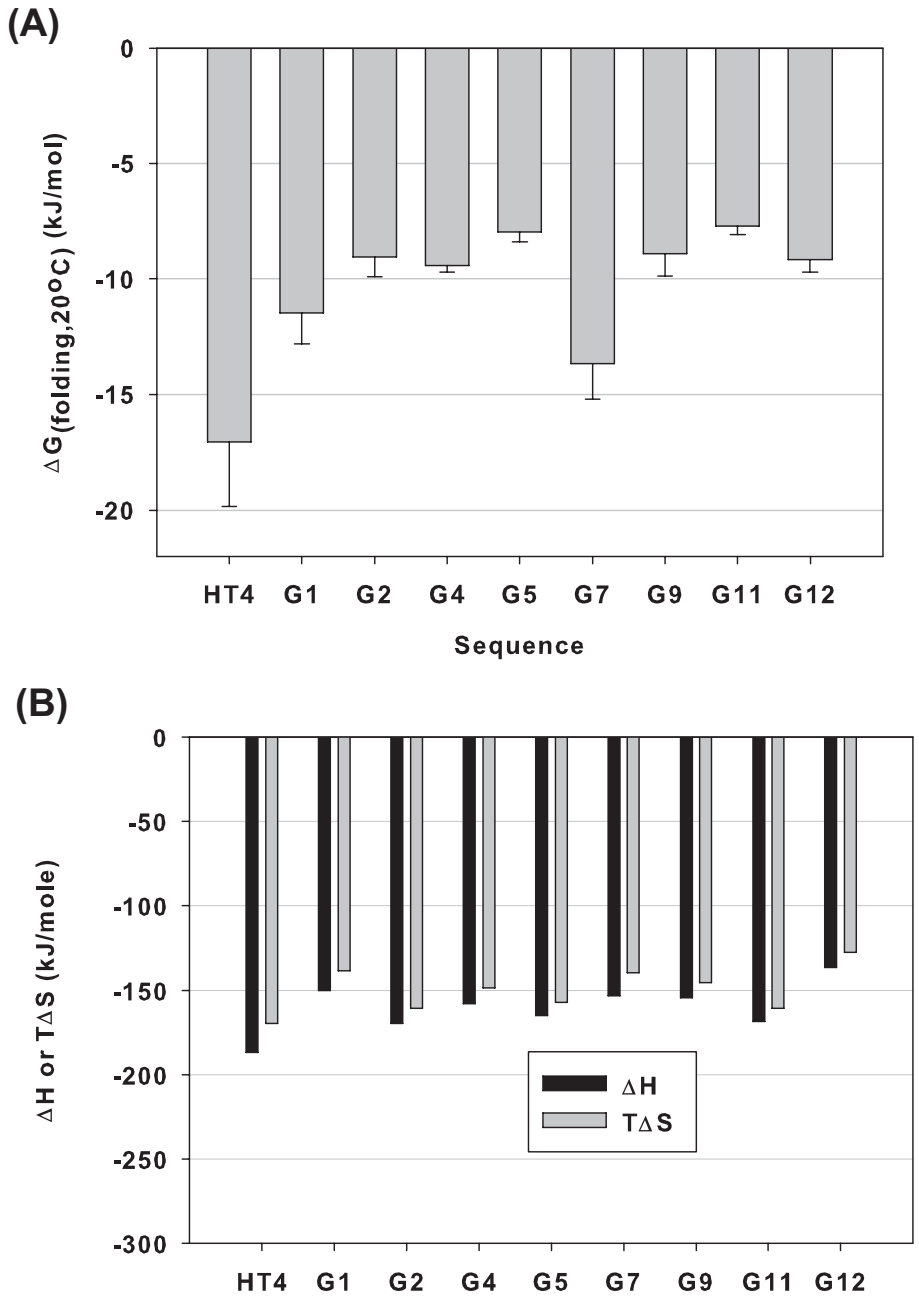

Figure 2.8. (A) Gibbs free energies (ΔG) and (B) enthalpy (ΔH) and entropy $T\Delta S$ contributions for folding of 6MI-labeled quadruplex sequences at 20°C in 100mM NaCl.

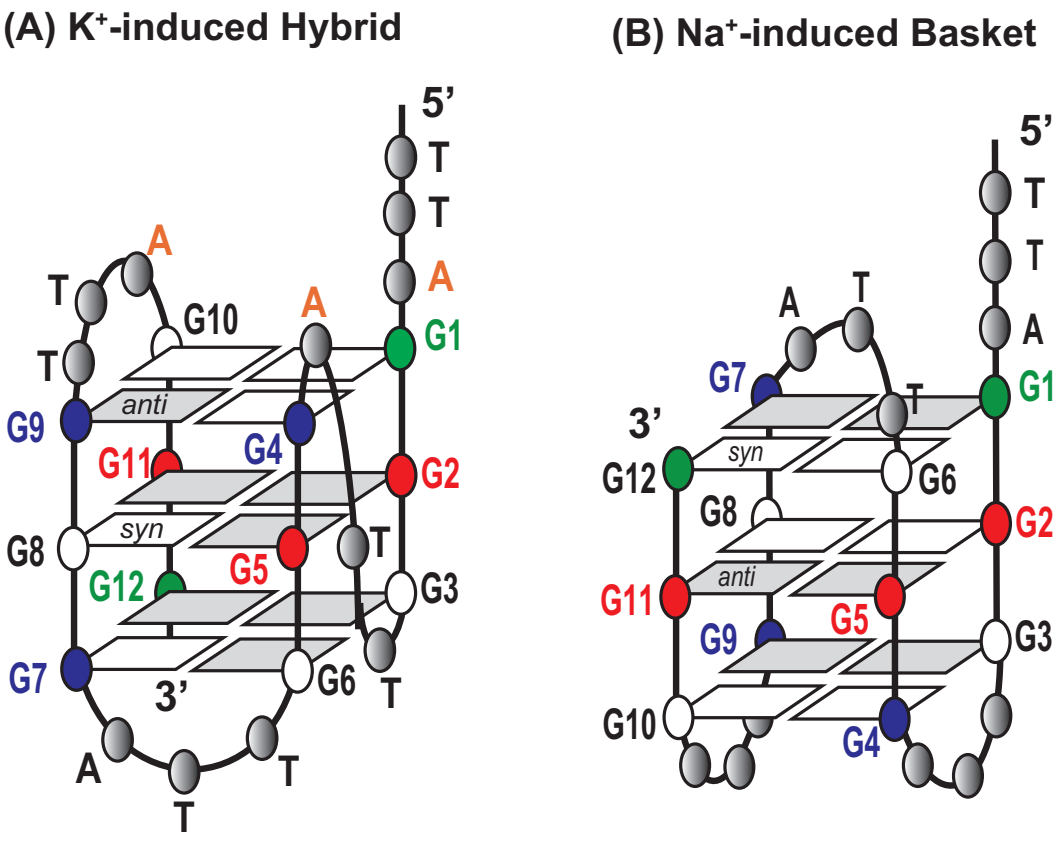

Figure 2.9. Schemes of G-quadruplex formed by the HT_4 in the (A) hybrid-1 (in K^+) and (B) basket (in Na^+) conformations. Substituted guanine positions shown in colored circles.

of the 5'-end, may be due to the stabilization by the nearby "adenine triple platform" (three "A"s marked in orange in Figure 2.9A).

Guanine substitutions within the center tetrad (positions G2, G5 and G11; red circles in Figure 2.9A) are in general well tolerated in the K^+-stabilized hybrid conformation at 37°C, with G5 the best. 6MI substitutions at positions G2 and G11 reduce the thermal stability compared with G5, suggesting that these two guanine residues with the potential for fraying near the termini are significant for maintaining quadruplex stability. Substitution near the loop regions (positions G4, G7 and G9; blue circles) are also conformationally well tolerated for the K^+-stabilized quadruplex. However, of the three loop substitutions, G9 is less tolerated than G4 or G7, due to 6MI's perturbation of the native *anti* glycosidic bond angle at the G9 position arising presumably from its involvement in diagonal loop formation in the hybrid-2 conformation (Figure1.8, page 15).

In general, the quadruplex stability is compromised when folded in the presence of Na^+-ions. In 100mM NaCl, guanine substitutions at G1, G7 and G12 have least conformational impact, although situated at the diagonal loop or terminal end positions. Interestingly, the TDS in 100mM NaCl for positions G1 and G7 are similar to their corresponding TDS in 100mM KCl. In addition, the melting point differences between quadruplexes in K^+ and in Na^+—$Tm_{(K^+-Na^+)}$ are lower than those for the parent HT_4. These results suggest that 6MI substitutions at these two positions (G1 and G7) may promote a quadruplex conformational switch to a hybrid like conformation. The typical Na^+-induced basket conformation may not tolerate alterations at positions G1 and G7 very well due to steric hindrances. Point mutations at positions other than G1 or G7 in Na^+-ions at physiological temperature (37°C), result in poor folding of the quadruplex, which may have physiological relevance. Indeed, alterations at positions G2, G5 and G11 have the most impact on the global stability, suggesting that the middle G-tetrad is critical for coordinating with Na^+ ions and therefore stabilizing the overall anti-parallel quadruplex solution conformation.

Chapter 3

LOCAL ENVIRONMENT OF GUANINE RESIDUES WITHIN THE HUMAN TELOMERIC G-QUADRUPLEX FORMING SEQUENCE

3.1 Introduction

With knowledge of how the global stability of the G-quadruplex conformation can be modulated by varying guanine substitutions using 6MI, we focused our studies on examining the local environment around key guanine positions of the quadruplex by exploiting the environmental sensitivity of the 6MI fluorescence signal. We have monitored the steady-state fluorescence signal for each 6MI-substituted sequence on folding to the G-quadruplex conformation, as a function of both temperature or cation concentration in the buffer. With 6MI substituted at different positions throughout the sequence, the relative extent of local interactions can be compared among the different guanine positions. Furthermore, results of these fluorescence studies can provide insights into local dynamics around each guanine residue on the HT_4 sequence with folding into the G-quadruplex conformation under physiological-like conditions. Such information can provide a better rationale for small-molecule drug design that can aid in targeting and stabilizing the G-quadruplex formation by the HT_4 DNA sequence.

Previous studies by other groups have shown that 6MI provides an environmentally sensitive probe for studying DNA interactions, given that its fluorescence signal is quenched

as a result of base stacking and hydrogen bonding with neighboring bases arising from conformational folding [76, 82, 83]. We have examined fluorescence intensity changes as a function of varying temperature: increasing temperature (heating) induces quadruplex melting/unfolding, whereas cooling promotes formation/annealing of the folded quadruplex conformation. In contrast to the melting profiles measured using absorbance values, which focuses on the global structural alterations of the entire quadruplex, we expect that the fluorescence thermal folding/unfolding data will provide important information about local environmental changes surrounding a particular guanine position as reported *via* the fluorescent signal from 6MI.

3.2 Materials and methods

Potassium-ion Titration Studies: As discussed in Chapter 1, it is well recognized that *in vitro* quadruplex formation requires the presence of cations, usually the monocovalent Na^+ or K^+-ion, for productive folding. However, differences in the magnitudes of fluorescence intensity quenching were observed for each 6MI-labeled sequence in the presence (100mM) and absence of KCl. In the current study we have quantified the observed intensity quenching effects as induced by the presence of K^+, to examine the role of this cation on quadruplex folding.

6MI-labeled oligonucleotides solutions were prepared at concentrations around 2 to 3μM in 10mM cacodylate (pH 7.2) buffer. Potassium-ion titrations were performed by measuring the fluorescence emissions from 6MI-containing oligonucleotides with addition of aliquots (every 1μl for the first 20μls; 2μl after 20μl; and 5μl after 30μls total addition) of K^+-containing buffer (10mM cacodylate and 2M KCl at pH 7.2) to the samples. This resulted in a total added volume of 105μl to 2ml (5% total volume change), providing a final KCl concentration around 100mM for each oligonucleotide sample. Intensity changes arising from dilution effects were thus small compared with the observed intensity effects arising from quadruplex folding. After incubation with stirring in the cuvette at 25°C for 5 minutes, fluorescence emission spectra were recorded using a Fluorolog-Tau3 (Spex/Horiba/Jovin).

Emission spectra were collected by scanning from 360 to 560nm using an excitation wavelength of 340nm (8nm excitation and 4nm emission slits) with a 1cm path-length quartz cuvette, at 25°C regulated using a Peltier temperature controller. Formation of quadruplex by each 6MI-labeled sequence following K^+ titration (i.e. final K^+ concentration 100mM) was confirmed from thermal absorption melting profiles.

Center of spectral mass (csm) from fluorescence emission spectrum: For the G1-substituted oligonucleotide, significant changes in peak emission wavelength were observed in both thermal unfolding and potassium-ion titration studies. Measurement of spectral shifts in the fluorescence emission spectra as a function of added potassium-ion, were analyzed from the center of spectral mass (csm):

$$\nu_{csm} = \frac{\sum \nu_i I_i}{\sum I_i}, \tag{3.1}$$

where I_i stands for the fluorescence intensity emitted at wavenumber ν_i [84]. In our study, csm was expressed as wavelength λ_{csm}, where $\lambda_{csm} = 1/\nu_{csm}$.

Analysis of Titration Data: A simple two-state model was assumed for the G-quadruplex conformation folding/unfolding transition, induced by K^+:

$$U + nM^+ \rightleftarrows FM_n^+$$

where U and F represent 6MI-labeled sequences in the unfolded and folded quadruplex conformations, respectively. M is the cation, which in the current study is the potassium cation. Assuming that the quadruplex is unfolded without K^+, and completely folded after saturation with 100mM KCl (as judged by no further change in fluorescence intensity values), the fraction of folded conformation α_i after each K^+ addition can be expressed as:

$$\alpha_i = \frac{I_i - I_0}{\Delta I_{max}} \tag{3.2}$$

where I_i is the integrated fluorescence intensity calculated from the area under the emission

curve after each K^+-addition using Sigmaplot 10. I_0 is the initial integrated intensity for DNA sample alone without K^+ and ΔI_{max} is the maximum difference between I_i and I_0. The fractions of folded quadruplex conformation α_i can be plotted against the $log_{10}[K^+]$ to provide a titration curve. Preliminary analysis of the sigmoidal-shaped titration curve indicates that the K^+-induced folding is cooperative. We therefore fit the titration curve to a Hill equation using the nonlinear least squares module of the program Origin 8.0 (OriginLab Corp., Northampton, MA, USA) to optimize values of the adjustable constants n and $K_{0.5}$:

$$\alpha_i = \frac{[M]_i^n}{K_{0.5}^n + [M]_i^n} \tag{3.3}$$

where: α_i is the fraction of folded quadruplex conformation; $[M]_i$ is the concentration of K^+ at α_i; $K_{0.5}$ is the K^+ concentration needed for half-saturation where $\alpha_i = 0.5$; and n is the Hill coefficient, which describes the cooperativity of the cation M^+ binding to the oligonucleotide. If $n > 1$, the K^+ binding exhibits positive cooperativity, indicating that once one K^+ cation binds to the unfolded HT_4 oligonucleotide, its affinity for further K^+ binding is increased. This usually arises due to conformational changes induced by ligand binding, leading to increased binding constants. Conversely, if $n < 1$, binding of the ligand exhibits negative cooperativity, where K^+ binding actually reduces the affinity of the oligonucleotide for further cation binding. When $n = 1$, the reaction is described as non-cooperative, and the ligand affinity does not depend on its concentration [85].

Fluorescence Melting Studies: 6MI-substituted oligonucleotide samples were prepared (DNA molecular concentration around 2μM in 10mM cacodylate (pH 7.2) buffer) with varying concentration of KCl or NaCl. To minimize solvent evaporation during the thermal studies, mineral oil was carefully layered on the surface of the solutions in the cuvette. Fluorescence emission spectra were recorded in a 1×1cm quartz cuvette using a Fluorolog-Tau3 (Horiba Scientific, Edison, NJ) spectrofluorometer equipped with a Peltier temperature controller. Fluorescence emission spectra were collected over the spectral range 360 to 560nm using an excitation wavelength of 340nm (with excitation slit=8nm; emission

slit=4nm), following a three minute incubation period with stirring, after each temperature change. The temperatures were changed, for both the unfolding or annealing process, over the range 10-70°C with 1°C interval. Fluorescence thermal unfolding "melting" profiles were obtained by plotting the integrated fluorescence intensity *versus* incubation temperature as reported on the Peltier controller. No significant differences were noted between the incubation temperature and the actual temperature of each sample recorded after each temperature change.

Determination of the midpoint of the thermal "melt" profiles—$T_{1/2}$ from fluorescence melting curves: Midpoint temperatures for the thermally induced unfolding/folding transitions of the quadruplex were extracted from the fluorescence/temperature data and denoted as the thermal melt transition temperature ($T_{1/2}$). $T_{1/2}$ values were determined as described for analysis of absorbance melting profiles (equation 2.4; 23). Briefly, the proportions of folded or unfolded quadruplex were determined from applying equation 2.4 to the fluorescence data after correction for non-zero baselines. Assuming that the change of fluorescence intensity observed is proportional to the extent of 6MI probe involved in G-quadruplex formation on each oligonucleotide, $T_{1/2}$ represents the mid-point transition temperature for the local conformational transition around the specific guanine substitution site. The local Gibbs free energy for folding (ΔG_{local}), the associated ΔH and ΔS were also extracted from the melting profiles as described previously in Chapter 2 (Equation 2.6 on page 24).

3.3 Results and discussions

We have examined the effects of both K^+ cations and temperature on the folding/unfolding transitions for the G-quadruplex conformation and at specific guanine locations along the quadruplex. Experiments were performed using K^+ ions since this cation dominates the intracellular ionic concentrations ($[K^+]$ = 139mM; $[Na^+]$ = 12mM; $[Mg^{2+}]$ = 0.8mM) for somatic cells [86]). Unlike previous studies using fluorescent quadruplex probes, which have examined the loop regions of the quadruplex using 2-AP [67, 68], our fluores-

cence studies have focused on the possible local environmental heterogeneity of the guanine positions within the quadruplex. To accomplish this aim, the sensitivity of the fluorescence signals (intensities and wavelength spectral shifts) from 6MI-substituted guanine positions within the HT_4 oligonucleotide have been used as a potential assay to examine the local conformational effects on the 6MI base during DNA oligonucleotide folding/unfolding.

3.3.1 Studies of quadruplex folding through potassium ion titration measurements

The fluorescence emission spectra for all 6MI-labeled oligonucleotides examined except G1, are shown in Figures 3.1 and 3.2 both in the absence and presence of varying concentrations of K^+-ion up to 100mM. A decrease in fluorescence intensity at 422 nm was observed for all the quadruplex sequences (G2, G4, G5, G7, G9, G11 and G12) except G1, with quadruplex folding promoted by addition of K^+. As discussed earlier (section 1.4), the fluorescence intensity of 6MI is exquisitely sensitive to quenching effects resulting from enhanced base-stacking, electron repulsion and H-bonding effects, and can provide a convenient fluorescence assay for following the folding/unfolding conformations of the G-quadruplex structure.

The fluorescence emission intensity values of the substituted 6MI-labeled oligonucleotides in the absence of KCl (that is, essentially unfolded) appear to be correlated with their locations within the HT_4 sequence. Indeed, the integrated emission intensity values for substituted 6MI are strongly dependent on the their neighboring bases and fall into three classes (Table 3.1): (1) single guanine on the 5'-side of the 6MI; (2) single guanine on the 3'-side of 6MI; (3) guanine residues sandwiching the 6MI.

When 6MI is positioned between two guanines (G2, G5 and G11) or between A and G (G4 and G7 with G on the 3'-side), a greater fluorescence intensity quenching effect is observed (lower apparent quantum yield), compared to when sandwiched between G and T (G9) or without a 3'-neighbor (G12) (Table 3.1). Thus it appears that a guanine residue positioned on the 3'-side of 6MI influences the electron distribution of the guanine residue, resulting in a reduced fluorescence intensity. Since 6MI is typically an electron acceptor [87],

the possibility of rapid electron transfer (possibly photoinduced) from neighboring bases could result in a lowered fluorescence intensity. It has been previously reported that guanine is a particularly good quencher of 2AP (a fluorescent analog of adenine) through an electron transfer mechanism between guanine and 2AP [88–91]. This might also be the case for 6MI. Indeed, previous studies by Narayanan *et al.* have reported that the photoinduced electron transfer between 6MI and guanine is thermodynamically more favorable than with adenine, thymine or cytosine [87].

With K^+-induced folding of the quadruplex forming oligonucleotide, the order of relative fluorescence quenching observed for the 6MI-labeled oligonucleotides appears to be independent of the neighboring bases and dependent on position within the quadruplex:

$$\text{G11}>\text{G4}\sim\text{G5}>\text{G9}\sim\text{G2}>\text{G7}>\text{G12},$$

with quenching values ranging from 53% (for G12) up to 83% (for G11) from the initial signal (100% in 0mM K^+) on folding in 100mM K^+ (Figure 3.3). As a control, the effect of K^+-ion on the free 6MI (0.2μM) with similar fluorescence intensity was significantly less, with an intensity quenching of $\sim$25% of the original intensity at 100mM KCl. Such variations in quenching efficiencies suggest altered abilities of 6MI positions to participate in base stacking with neighboring bases on folding, with the G11 and G5 substitutions within the center tetrad exhibiting the greatest quenching effects. Interestingly, as shown in Figure 3.3, the quenching of the fluorescence occurs within a rather narrow K^+-ion concentration range (0-20mM KCl). Hence, nucleation of the quadruplex appears to occur at lower K^+-ion concentrations, although higher concentrations of K^+-ion are required to better stabilize the quadruplex conformation [92].

Effects of Quadruplex Folding on G1 Substitution: For the labeled sequence G1, where the 6MI is situated near the 5'-end, a surprising enhancement in fluorescence intensity was observed as a result of quadruplex folding as induced by the addition of 100mM KCl relative to the unfolded concentration (absence of K^+-ion) (Figure 3.4A). In fact, the fluorescence intensity of G1 shows a two-stage change from 0mM to 100mM [K^+] (Figure 3.4B). Initially, quenching of the intensity is observed, but within a very narrow range

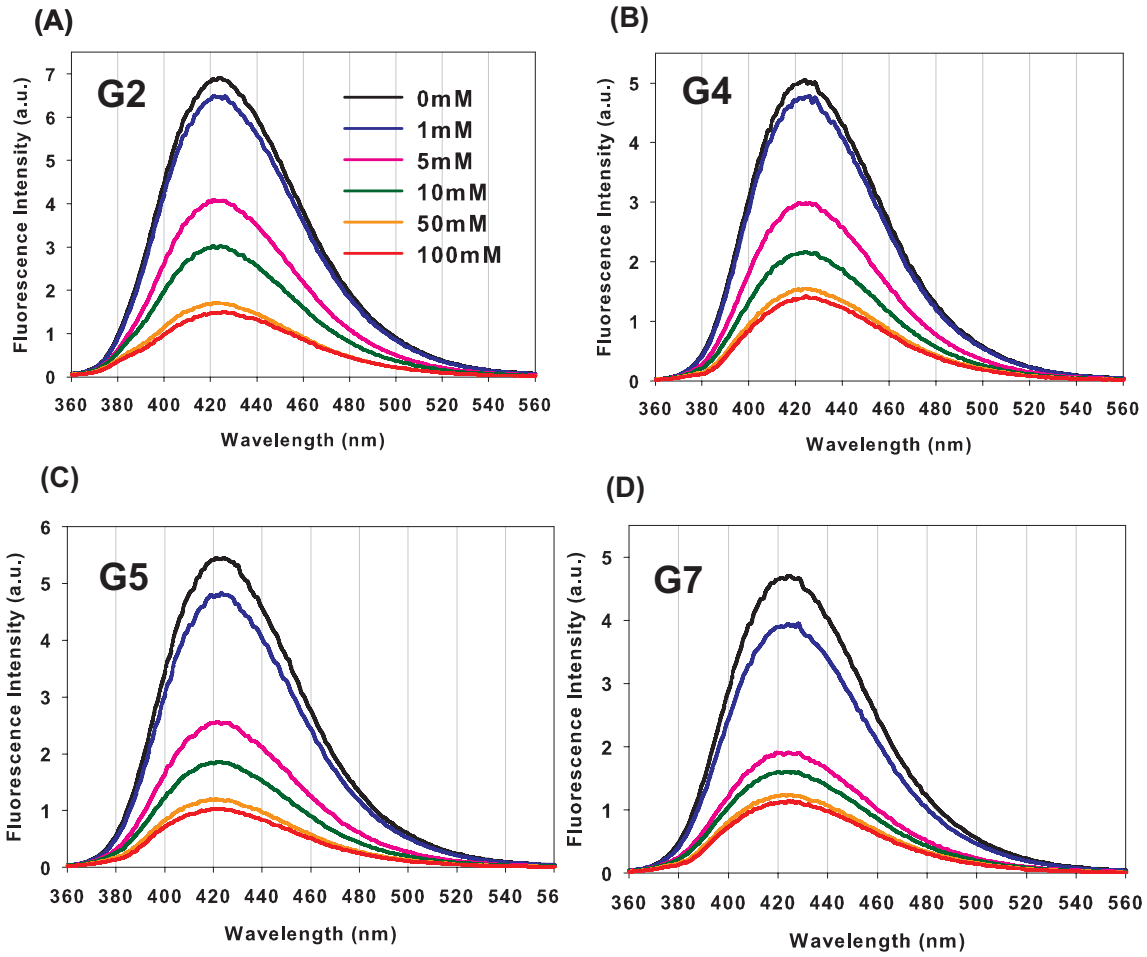

Figure 3.1. Fluorescence spectra of (A) G2; (B) G4; (C) G5; (D) G7; with KCl titration. Aliquots of KCl-containing buffer (10mM cacodylate and 2M KCl at pH 7.2) were titrated to 6MI-labeled DNA sequences (2 to 3 μM) in 10mM cacodylate buffer (pH 7.2). Fluorescence spectra were scanned at 25°C from 360 to 560nm with excitation wavelength 340nm. Excitation and emission slits were 8nm and 4nm, respectively. Fluorescence emission spectra in presence of 0mM (black line), 1mM (blue line), 5mM (pink line), 10mM (green line), 50mM (orange line) and 100mM (red line) KCl are shown.

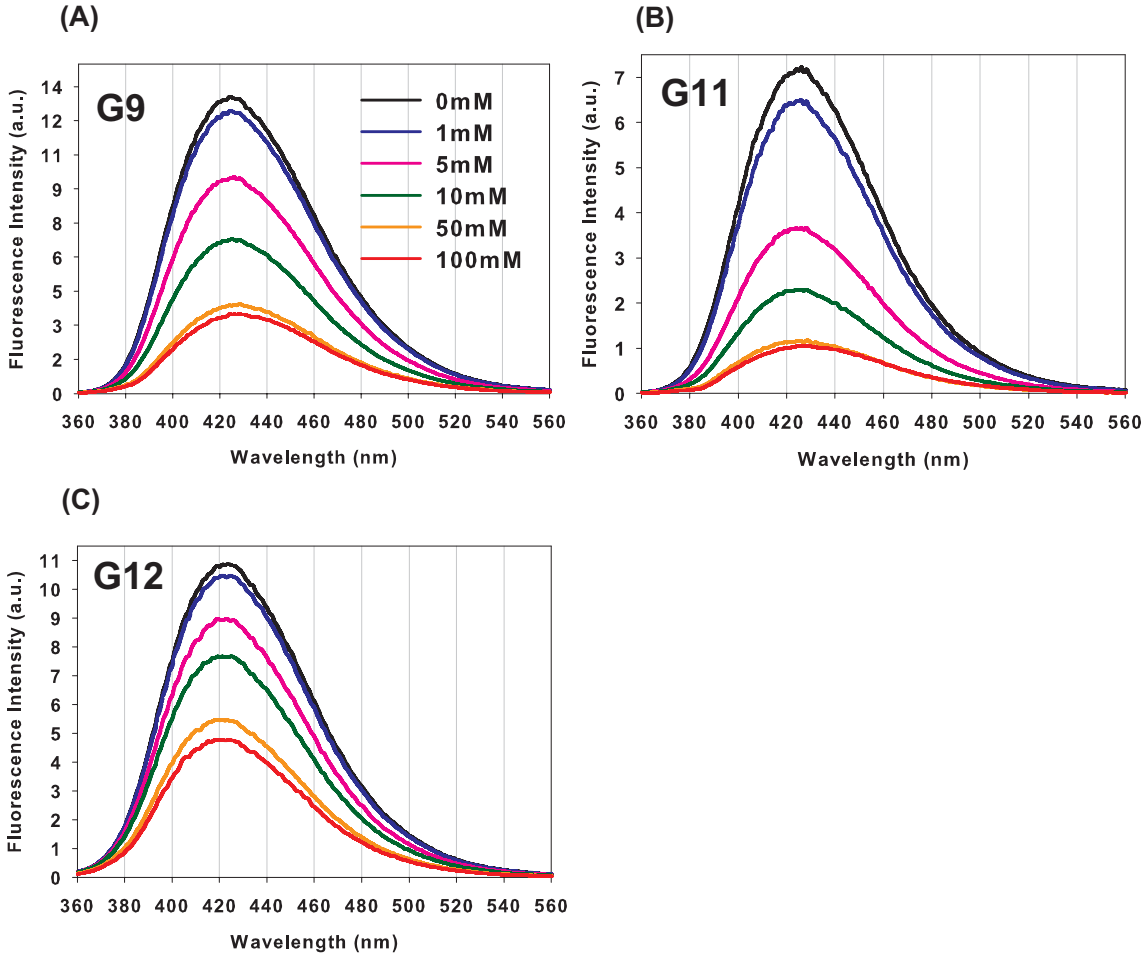

Figure 3.2. Fluorescence spectra of (A) G9; (B) G11; (C) G12; with KCl titration. Aliquots of KCl-containing buffer (10mM cacodylate and 2M KCl at pH 7.2) were titrated to 6MI-labeled DNA sequences (2 to 3 μM) in 10mM cacodylate buffer (pH 7.2). Fluorescence spectra were scanned at 25°C from 360 to 560nm with excitation wavelength 340nm. Excitation and emission bandwidths were 8nm and 4nm, respectively. Fluorescence emission spectra in presence of 0mM (black line), 1mM (blue line), 5mM (pink line), 10mM (green line), 50mM (orange line) and 100mM (red line) KCl are shown.

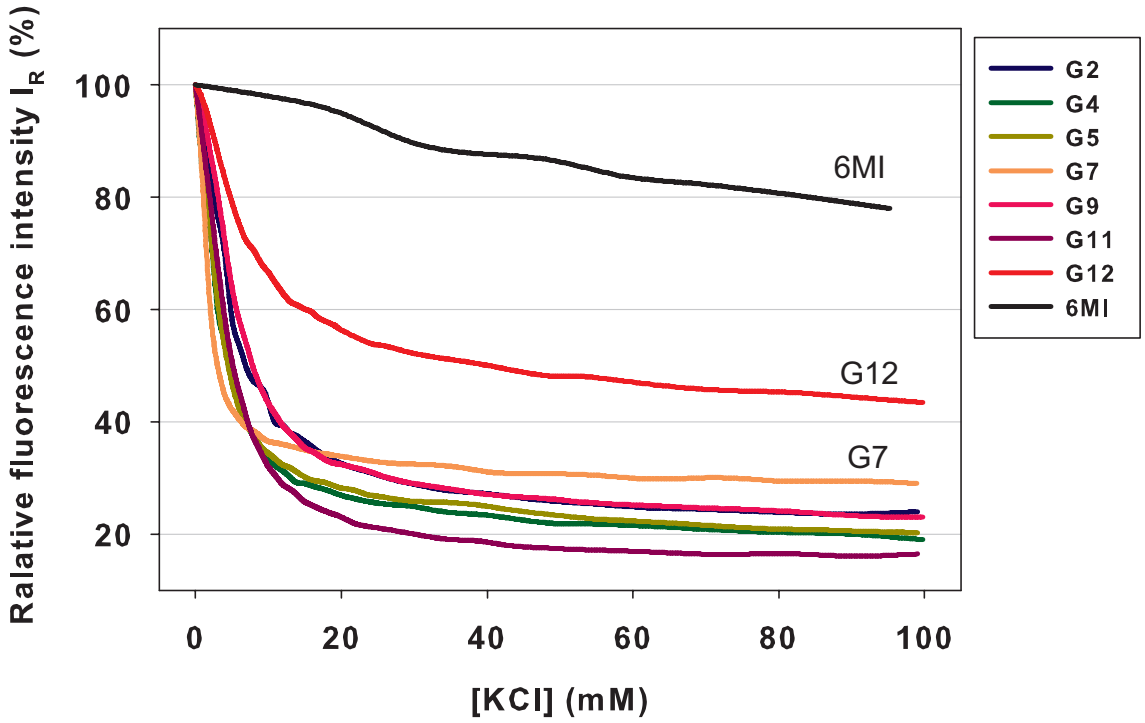

Figure 3.3. Relative integrated fluorescence intensity I_R for 6MI alone and 6MI-labeled sequences as a function of KCl concentrations. The relative integrated fluorescence intensity I_R for each 6MI-labeled sequence was calculated from $I_R = I_X/I_0 \times 100\%$, where I_X and I_0 are the integrated fluorescence intensities with XmM and 0mM KCl, respectively.

Table 3.1. Neighboring bases and integrated emission intensity at 0mM KCl for 6MI-labeled sequences

6MI-substituted sequence	Bases sandwiching 6MI (5'→ 3')[a]	Integrated emission intensity in 0mM KCl per μM DNA
G9	GFT	3.83
G12	GF	3.51
G2	GFG	2.01
G11		1.94
G5		1.63
G1	AFG	1.89
G7		1.63
G4		1.50

[a] F = 6MI fluorophore.

of (0mM to 4mM) KCl. With higher K^+-ion concentrations, we observed an increase in fluorescence intensity (from 5mM up to 100mM KCl in Figure 3.4B). The initial intensity quenching observed with $[K^+]< 4$mM may result from random base stacking interactions of G1 with other nucleotide bases, before the bases become involved in quadruplex formation. However, with higher K^+-ion concentrations (>5mM) promoting quadruplex formation, G1 does not participate in base stacking with other bases in the folded quadruplex, which may arise from 5'-end strand fraying and flexibility, although quadruplex formation does occur (from TDS data in Chapter 2).

In addition to the observed fluorescence intensity enhancement, the emission spectrum for G1 reveals a significant shift to longer wavelengths from 430nm (at 0mM $[K^+]$) to 442nm (at 100mM) on quadruplex folding, as shown in Figure 3.4A, suggesting possible involvement in solvent interactions. The center of spectral mass (csm) was plotted as a function of K^+ concentrations for each labeled sequence as shown in Figure 3.5. For G1, the peak shifting to longer wavelength corresponds exactly with the intensity changes observed where the K^+ concentration increases from 5mM to 30mM (Figure 3.5A). For other labeled sequences, the emission peaks revealed only a slight 1-2nm red (longer) wavelength shift for G4, G9 and G11, or to the blue (shorter) wavelength for substituted positions: G2, G5 and G12 (Figure 3.5B), suggesting minimal solvent interaction with folding.

Fits of K^+-titration curve to Hill's equation We have adapted the Hill Plot—usually used for measuring the binding of a ligand to a macromolecule, for examining the influence of K^+-ion on the folding pathway of the G-quadruplex as detected by specific guanine-substituted positions along the quadruplex sequence. Fits of the Hill equation to the fraction of quadruplex folded as a function of increasing K^+-ion concentration revealed the Hill coefficients, n, with values all greater than 1, suggesting that the quadruplex folding process as promoted by K^+ exhibits positive cooperativity (Figure 3.6 and 3.7). The concentration of K^+-ions required to achieve 50% folding as judged by fluorescence intensity quenching (or signal enhancement in the case of G1 sequence), $K_{0.5}$ follows the order (Table

3.2):

$$G7<G5<G11\sim G4<G2<G9<G12<G1.$$

Differences in $K_{0.5}$ values presumably reflect the sensitivity of 6MI along the HT_4 sequence to its local environment (Figure 1.8 on page 15) during K^+-induced quadruplex formation, which initiates (as described above) at relatively low K^+-ion concentrations. The variations in $K_{0.5}$ values suggest that the quadruplex folding process may proceed through local conformational intermediates. Indeed, the low $K_{0.5}$ values obtained for positions G7 (next to the adenine in the third TTA segment) and G5 (located in the middle G-tetrad), suggest that these two guanine positions may play a significant role in nucleating quadruplex folding, through enhanced base-stacking with neighboring bases as promoted by K^+ cations, even before the entire quadruplex conformation is fully formed and stabilized at higher (100mM) salt concentration. The nucleation process is then extended to other guanine positions—G2 and G11, which are located on the same middle tetrad as G5 in the HT_4 quadruplex, and G4 and G9 adjacent to the TTA loop regions. On the other hand, G9 and G12 are only folded when relatively high concentrations of K^+-ion have been added. This compares favorably with global stability studies described above (Figure 2.4), which showed that positions G9 (on the diagonal loop) and G12, at the 3'-end are relatively unstable guanine sites. Interestingly, both G7 and G5 guanine bases exist in the *syn*-orientation within the hybrid-2 K^+-ion stabilized quadruplex conformation and demonstrated the greatest thermal stabilities from global stability studies.

G1 and G12, located at the flexible 5'- or 3'-ends respectively of the HT_4 sequence give rise to the highest $K_{0.5}$ values, suggesting that these terminal guanine positions are somewhat insensitive to the folding process, with weaker neighboring base interactions. After all the other guanine positions are essentially "locked" into the quadruplex conformation, these two terminal end positions appear to be involved in "fraying".

In summary, K^+-ion titration measurements for each 6MI-labeled quadruplex forming sequence suggest that guanines 5, 7, 2 and 11 are the initial and critical guanine positions for quadruplex formation in the presence of relatively low K^+ cation concentrations. The

Table 3.2. Optimal fitting parameters for the K^+ titration curve shown in Figure 3.6

Sequence	$K_{0.5}$ (mM)	n
G1	14.65±0.06	6.20±0.50
G2	4.83±0.12	1.49±0.01
G4	4.16±0.02	1.64±0.05
G5	3.16±0.01	1.35±0.07
G7	1.91±0.21	1.43±0.03
G9	6.01±0.79	1.64±0.01
G11	4.11±0.05	1.53±0.01
G12	8.98±1.28	1.23±0.05

interactions with K^+ cations are further extended to the guanines adjacent to the TTA loop regions (G4 and G9) and proceed last for the terminal guanines (G1 and G12).

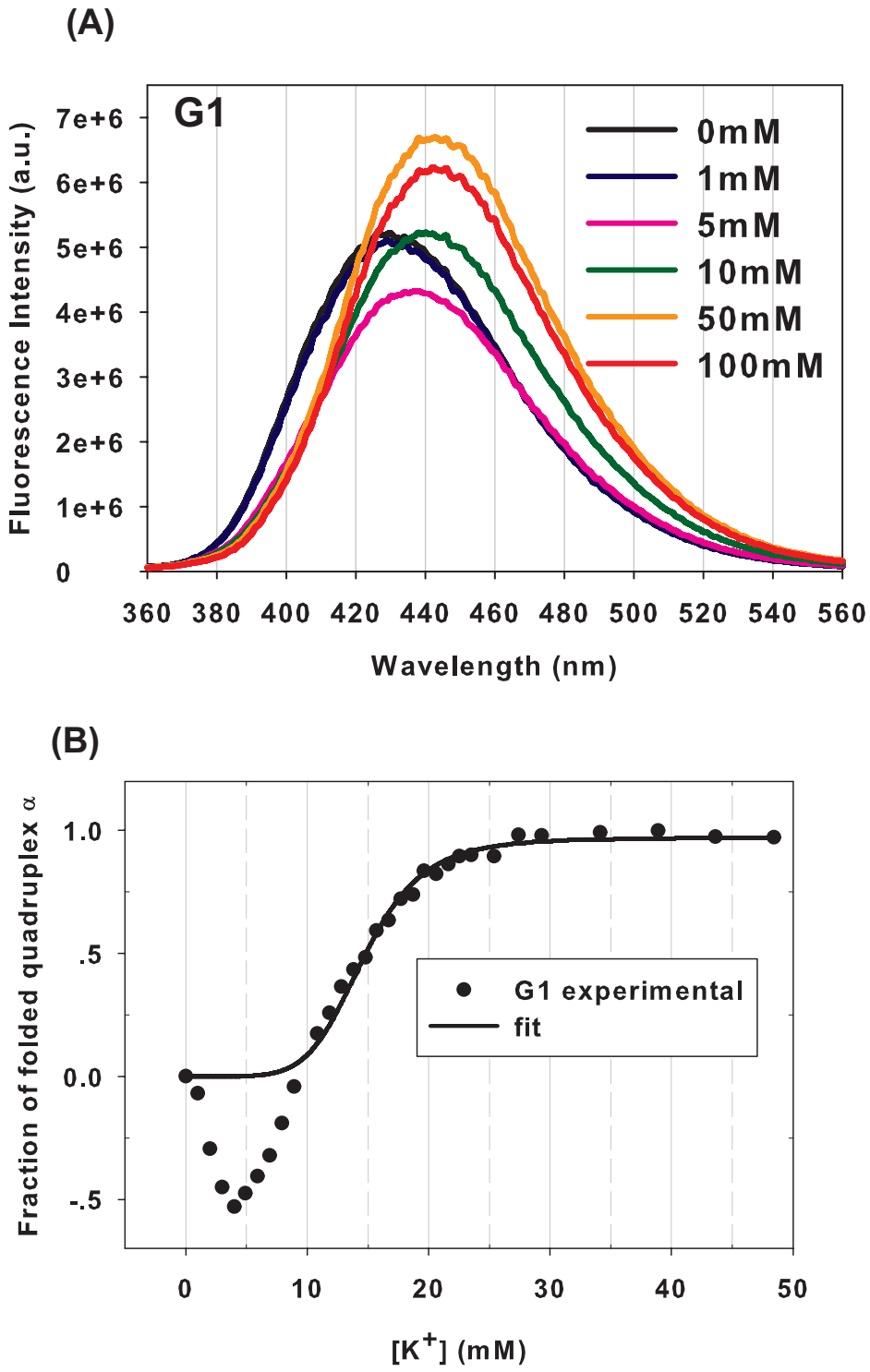

Figure 3.4. (A) Fluorescence emission spectra of G1 in presence of 0mM (black line), 1mM (blue line), 5mM (pink line), 10mM (green line), 50mM (orange line) and 100mM (red line) with excitation wavelength 340nm. (B) Fraction of folded quadruplex α is derived from (A). The negative values of α for $[K^+]$ lower than 10mM result from the emission intensity quenching relative to 0mM.

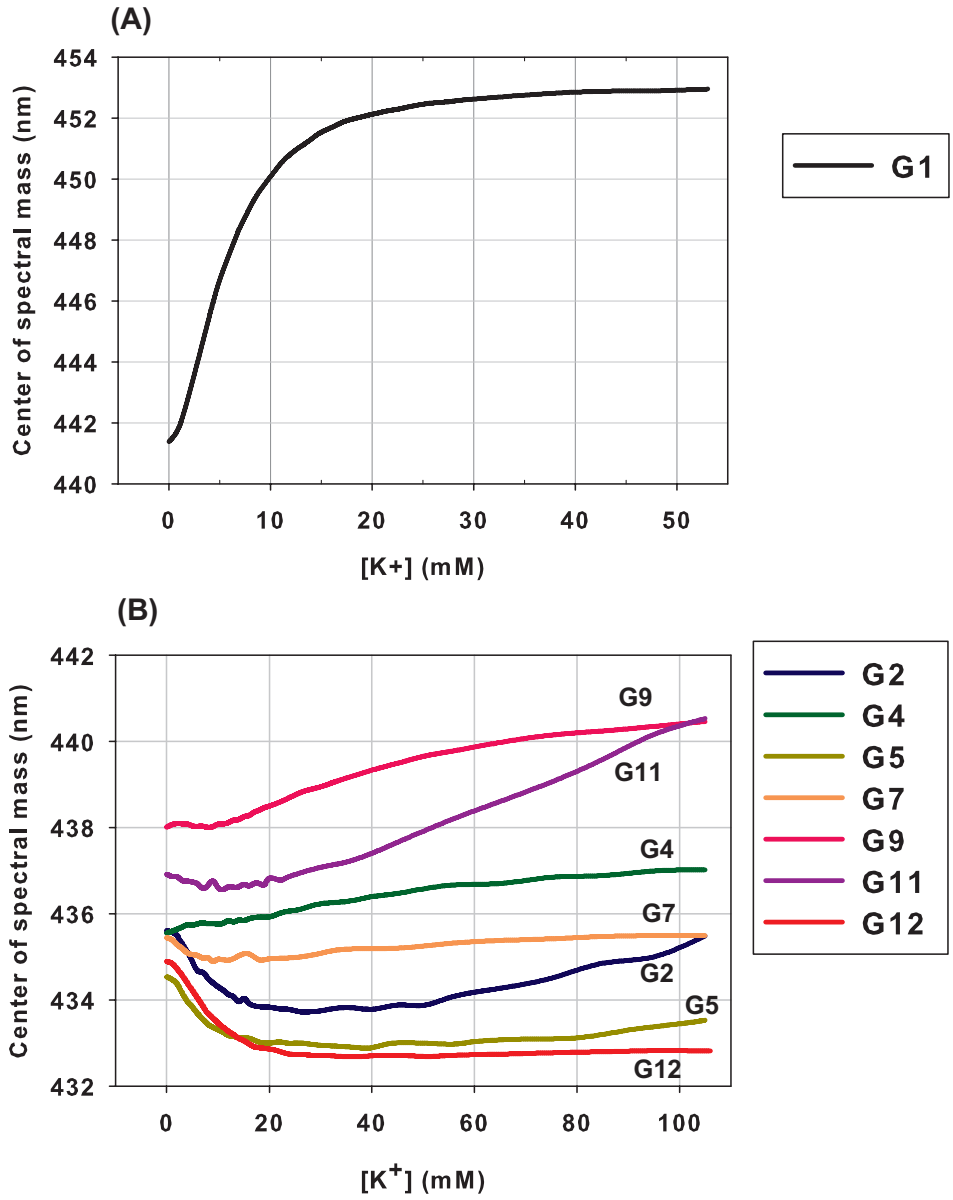

Figure 3.5. Center of spectral mass as a function of KCl concentration for (A) G1 and (B) all other 6MI-labeled sequences, is calculated from $\frac{\sum \lambda_i I_i}{I_i}$, where I_i stands for the fluorescence intensity emitted at wavelength λ_i.

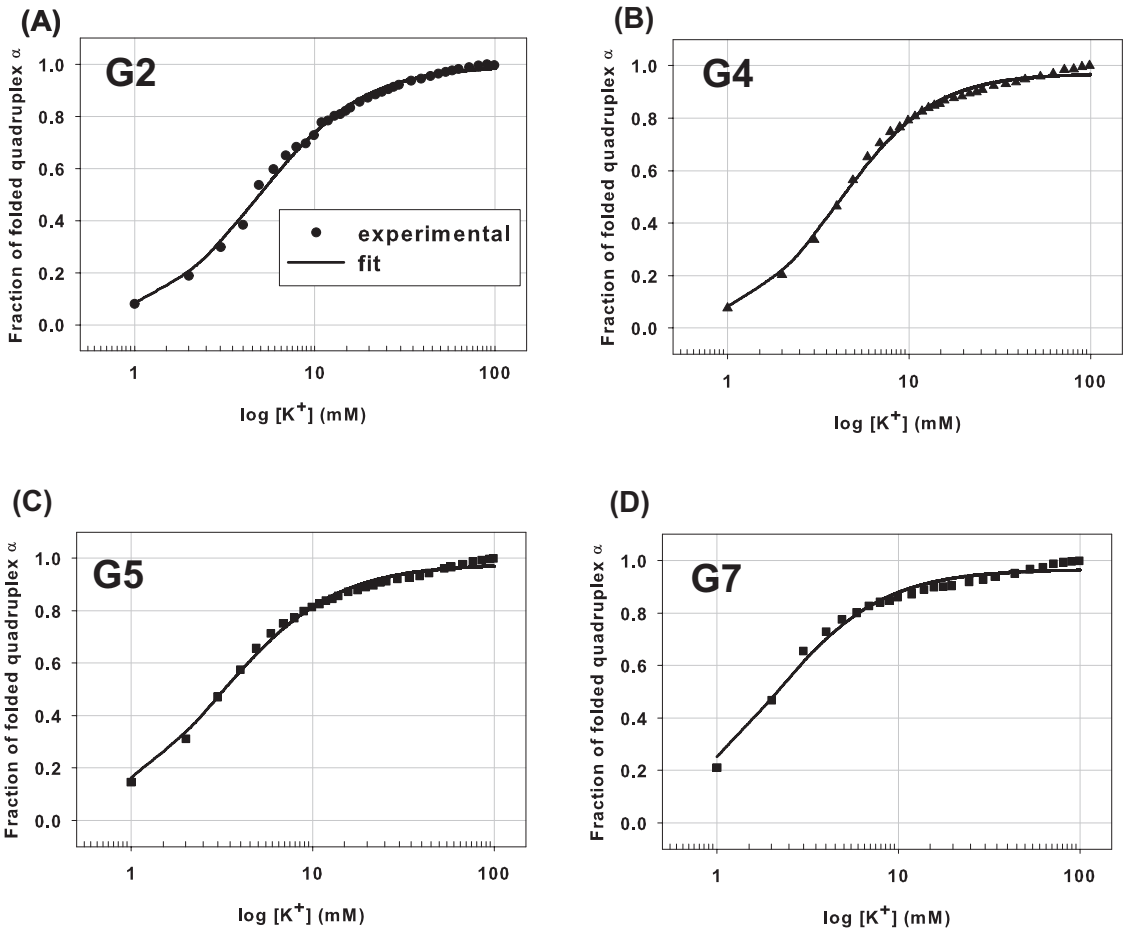

Figure 3.6. Fraction of folded quadruplex α was derived from the fluorescence intensity change shown in Figure 3.1, assuming quadruplex was completely unfolded and folded at initial and end points. Fitting curves were derived by fitting the points to Hill equation as described in method for A) G2; B) G4; C) G5; D) G7. Experimental data are shown as symbols and the fitted curves are shown as the solid lines. Incubation temperature was 25°C.

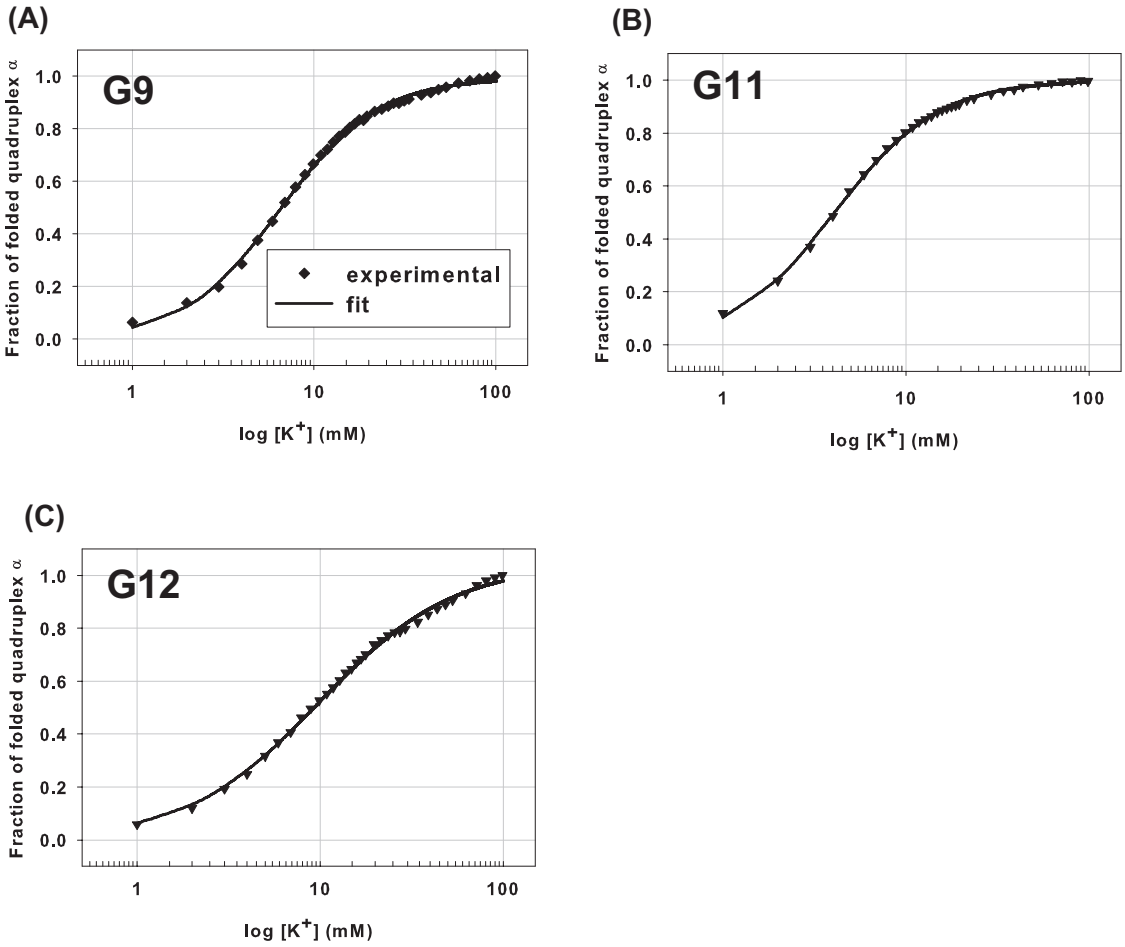

Figure 3.7. Fraction of folded quadruplex α is derived from the fluorescence intensity change shown in Figure 3.2 for A) G9; B) G11; C) G12. Experimental data are shown as symbols and the fitted curves are shown as the solid lines. Incubation temperature was 25°C.

3.3.2 Fluorescence folding studies of 6MI-labeled HT_4 G-quadruplex

Fluorescence-based thermal annealing (folding) transitions were obtained in 100mM KCl or NaCl are shown in Figure 3.8. With decreasing temperature, folding of the quadruplex sequence is promoted in the presence of 100mM KCl. As expected, on folding, all the 6MI-labeled sequences except G1, revealed quenching of fluorescence intensities relative to their intensities at 70°C (Figure 3.8A). Given that the fluorescence intensity for 6MI is quenched as it base stacks with neighboring nucleotides, this observation indicates that enhanced local base stacking interactions occur around the substituted guanine positions when folding occurs.

Interestingly, when buffer conditions are changed from KCl to NaCl, three oligonucleotide sequences—G1, G2 and G12 all showed fluorescence intensity enhancements with oligonucleotide folding (resulting from a decrease in temperature). In contrast, the other five sequences studied—G4, G5, G7, G9 and G11 exhibit the expected fluorescence intensity quenching with folding, similar to those observed for KCl (Figure 3.8B).

The observed enhancement of fluorescence intensity in NaCl for G2 and G12 labeled sequences at temperatures below 30°C, was unexpected. Additionally, G2 was surprisingly insensitive to temperature changes (Figure 3.9A) in the range of 30-48°C. As a negative control, the effect of temperature on the fluorescence signal of the fluorophore was examined for the unfolded G2 sequence. In buffer alone without NaCl (no folding), G2 showed an almost linear increase of fluorescence intensity (Figure 3.9A). To correct for this linear temperature (thermal) effect on the measured (raw data; Figure 3.9A) fluorescence intensity of the 6MI fluorophore, which is unrelated to quadruplex folding, we calculated the relative fluorescence intensity change of G2 in 100mM NaCl to that without, as shown in Figure 3.9C. After correction for thermal quenching effects of the 6-MI fluorophore, a small intensity quenching is observed around 30-48°C. This indicates that the fluorescence intensity change observed with decreasing temperature (shown in Figure 3.9A) is a combination of the thermal effects (relief of quenching with decreasing temperature) on the intrinsic florescence of the 6MI fluorophore, and the fluorescence quenching of G2 arising from quadruplex folding. As a

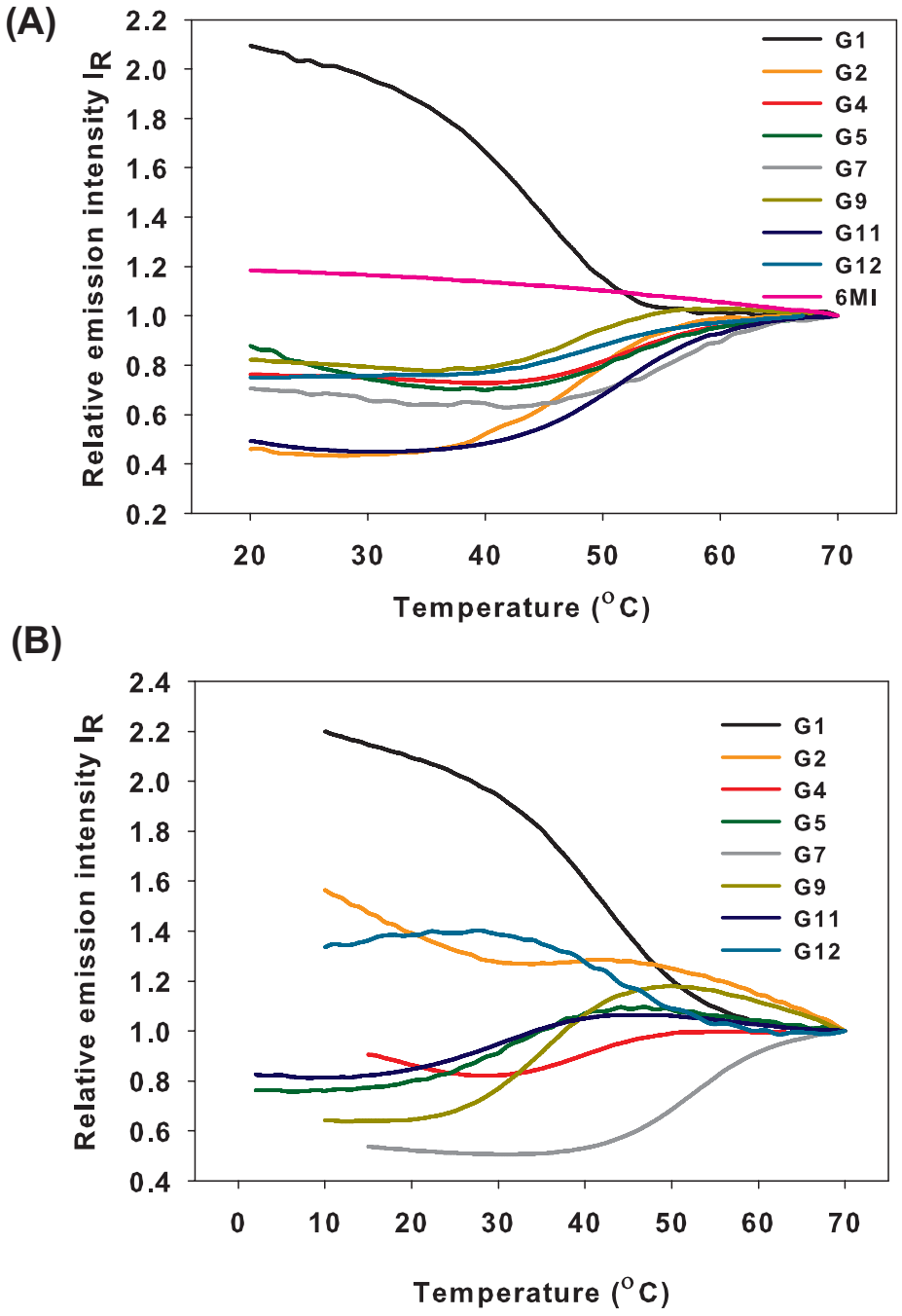

Figure 3.8. Relative emission intensity for 6MI and 6MI-labeled oligonucleotides as a function of decreasing temperature from 70°C to 20°C in 10mM cacodylate buffer(pH 7.2) with (A) 100mM KCl or (B) 100mM NaCl. Relative emission intensity I_R was calculated from $I_R = I_T/I_0$, where I_T and I_0 are the integrated emission intensities at temperature T and 70°C respectively.

result, the experimentally observed "constant" intensity around 30-48°C is a result of these two processes, and data were corrected for thermal effects as discussed below.

The continuing intensity increase with temperature lower than 30°C suggests that after its involvement in quadruplex formation, G2 is not totally buried into the Na^+-stabilized antiparallel quadruplex conformation through base stacking with other residues. Similarly, the fluorescence annealing curve of G12 in the presence of 100mM NaCl (Figure 3.11) also exhibit intensity enhancement on decreasing temperature/quadruplex folding. Therefore, the intensity enhancements observed the fluorescence annealing curves for G1, G2 and G12 in NaCl suggest that guanines near two ends within the quadruplex are not involved in strong interactions with other bases and exist in more "open and loose" conformational states.

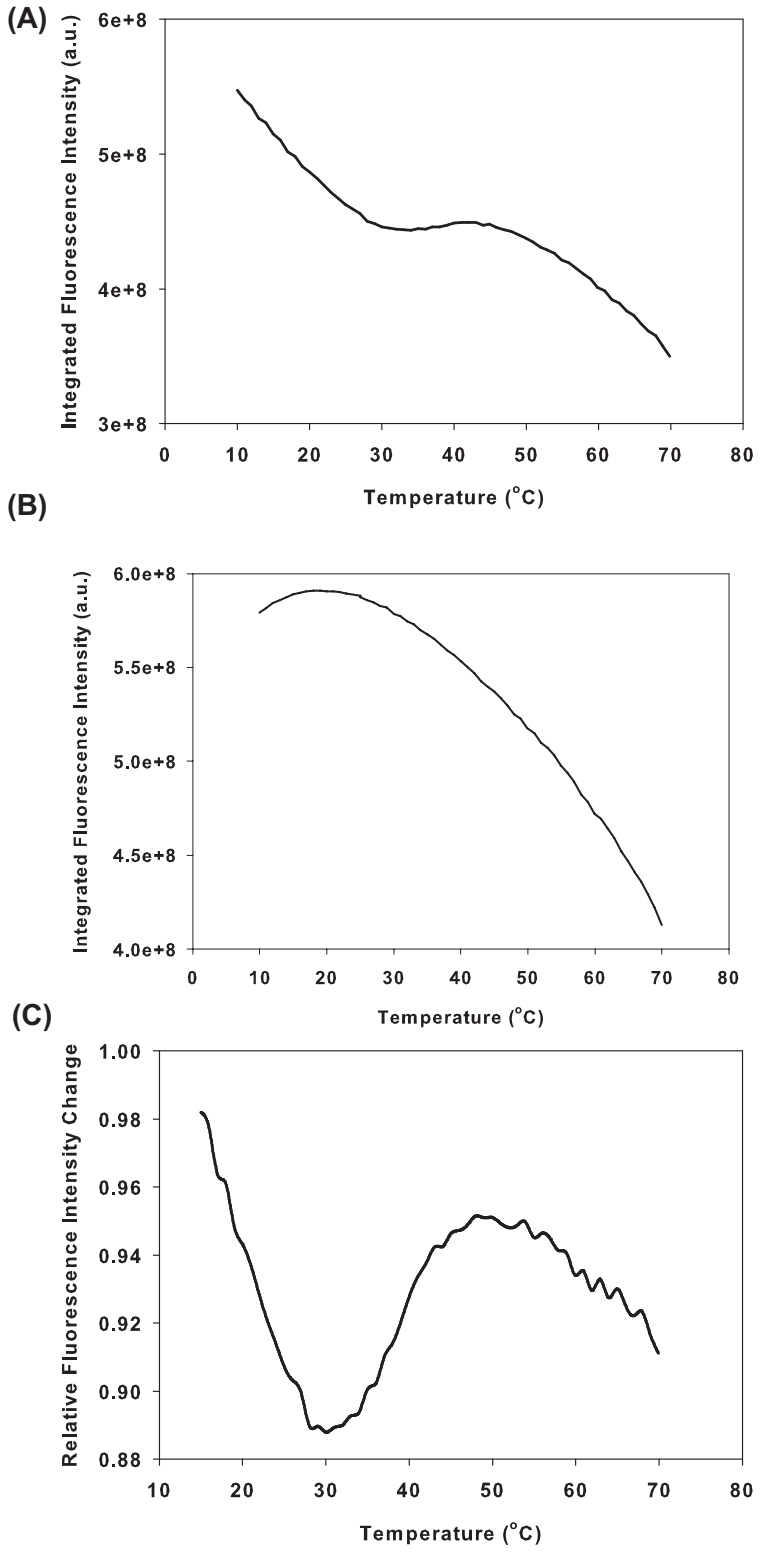

Figure 3.9. Fluorescence annealing curve of G2 in 10mM cacodylate (pH 7.2) with (A) 100mM NaCl; (B) without any other cation. (C) Relative fluorescence intensity was calculated from F_{NaCl}/F_0, where F_{NaCl} and F_0 are the intensity of G2 in (A) and (B) respectively on same temperature.

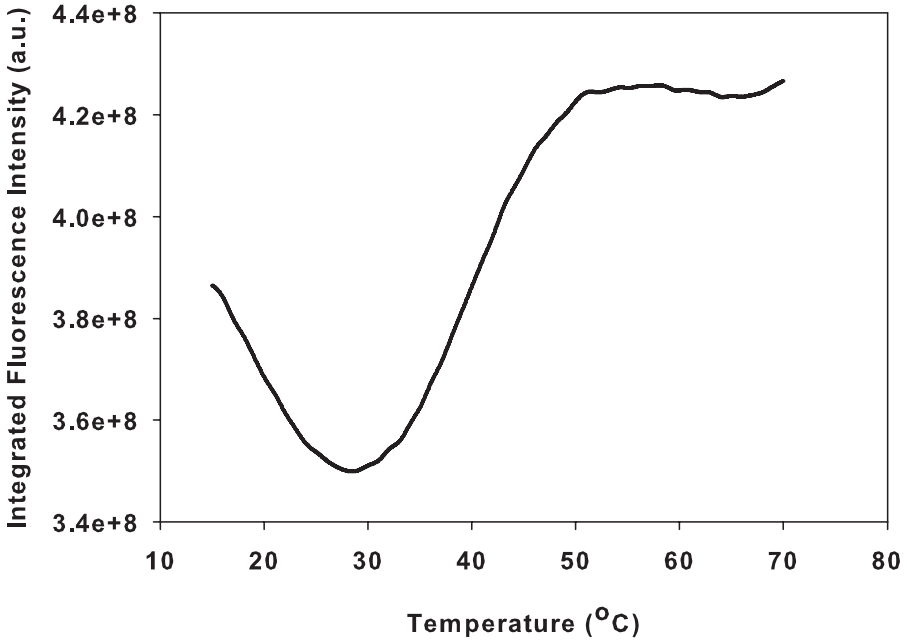

Figure 3.10. Fluorescence annealing curve for G4 in 100mM NaCl.

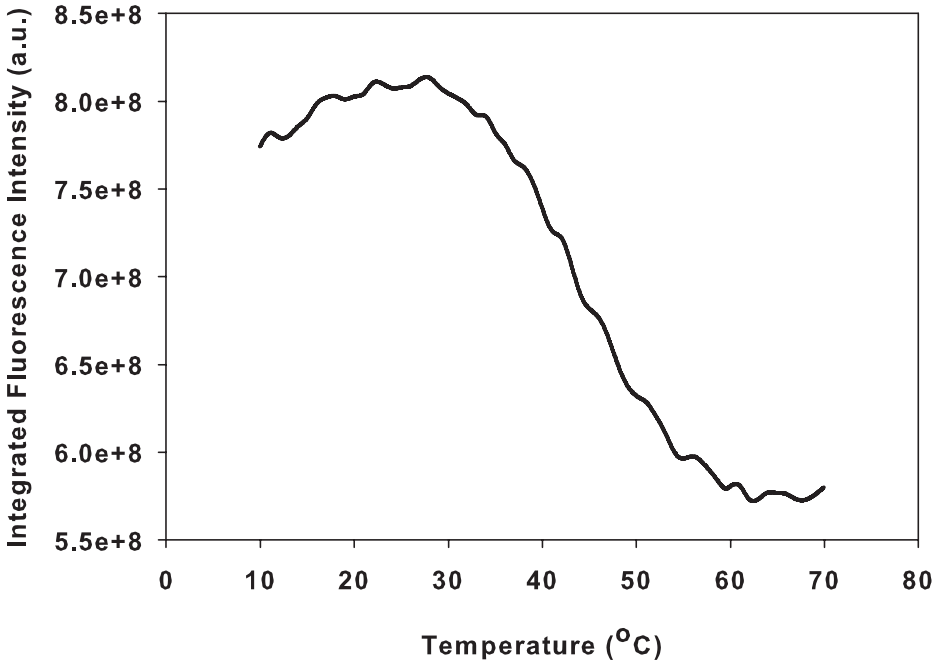

Figure 3.11. Fluorescence annealing curve for G12 in 100mM NaCl.

Thermal transition temperatures ($T_{1/2}$) and associated local thermodynamics of labeled oligonucleotides from fluorescence folding curves in KCl and NaCl: Melting points, $T_{1/2}$, extracted from the fluorescence folding curves (after correction for the de-quenching of 6MI from decreasing temperature as shown Figure 3.12) for 6MI labeled telomeric sequences in the presence of either 100mM KCl or NaCl, are summarized in Table 3.3. $T_{1/2}$ values for the 6MI-labeled sequences follow the orders below:

G7>$\boxed{\text{G5}\sim\text{ G4}\sim\text{ G11}}$>$\boxed{\text{G9}\sim\text{ G12}}$>G2>G1 (in 100mM KCl), and

G7>$\boxed{\text{G1}\sim\text{ G12}}$>$\boxed{\text{G4}\sim\text{ G2}}$>G9>$\boxed{\text{G5}\sim\text{ G11}}$ (in 100mM NaCl).

Since no hysteresis was observed, the $T_{1/2}$ values extracted from unfolding profiles were comparable with those values from the corresponding folding pathways. The $T_{1/2}$ values extracted here, represent the involvement of the substitution positions in base interactions during the folding process. The $T_{1/2}$ values in 100mM KCl suggest that formation of the hybrid quadruplex conformation may proceed through nucleation *via* base interactions at the center tetrad (G5 and G11) followed by loop formation via the *syn*-guanine residues. Folding at the terminal ends (G1, G2 and G12) proceeds last. Interestingly, the order of $T_{1/2}$ values measured from fluorescence studies do not give exactly the same ordering of Tm values measured from UV-spectroscopic measurements, which focus on overall global stability effects. For example, substitution at position G1 is well tolerated in the overall quadruplex formation (high Tm from Chapter 2), but has the lowest $T_{1/2}$ determined by 6MI fluorescence. Hence, guanine 1 may not participate strongly in the quadruplex annealing process, and may be "fraying" at the 5'-end, which can be well tolerated in the overall "global" conformation.

When buffer conditions are changed to 100mM NaCl, the $T_{1/2}$ values for the folding process suggest that base interactions of guanine positions located on the top G-tetrad (G1, G12 and G7) play significant roles in productive folding into a quadruplex conformation, whereas guanines located within the middle tetrad (G2, G5 and G11) are reduced, contributing to a less stable quadruplex.

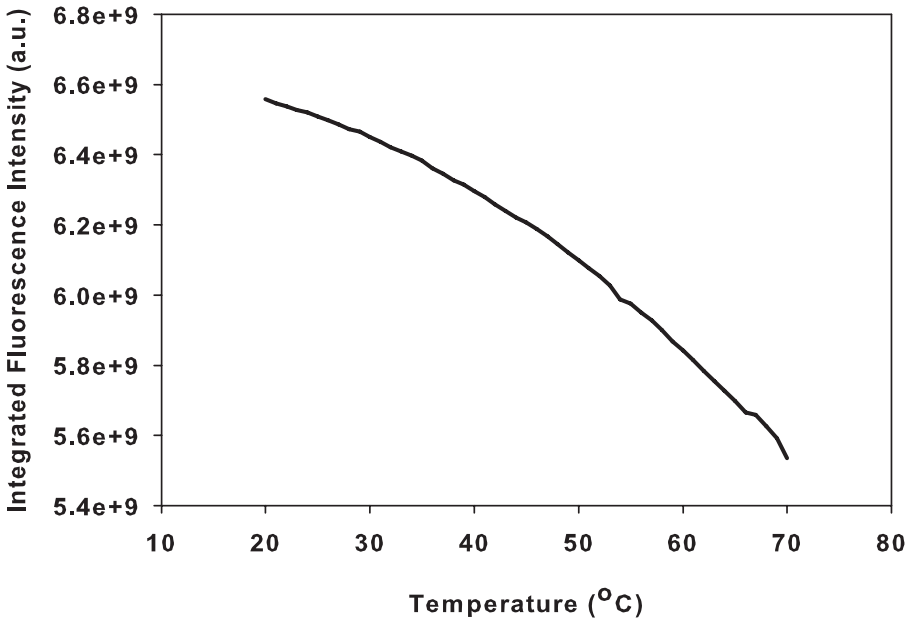

Figure 3.12. Fluorescence intensity of 6MI monomer in 10mM cacodylate buffer across the temperature range 20-70°C.

Comparing a specific substitution site in the presence of either K^+ or Na^+ cations also demonstrates differences in the unfolding/folding effects experienced at the substituted sites, as exhibited through differences in their fluorescence melting transitions. As shown above, and in comparison with observed differences in absorbance melting points ($\Delta T_{m(K^+-Na^+)}$ shown in Table 2.1 on page 32), the differences in fluorescence melting curve—$\Delta T_{1/2(K^+-Na^+)}$ are greatest in G5 and G11, moderate in G2, G4 and G9, and least in G1, G7 and G12. However, as discussed above, substitution at the G1 and G7 positions by 6MI may result in a conformational switch from the Na^+-ion stabilized basket conformation to the K^+-ion stabilized mixed hybrid-2 conformation.

Local free energy values (ΔG_{local}) were determined from the fluorescence unfolding/annealing profiles of 6MI-labeled oligonucleotides at 37°C in 100mM KCl as described above in Equation 2.6 on page 24. Values for ΔG_{local} and the associated ΔH and $T\Delta S$ values are summarized in Figure 3.13. The local folding for each guanine residue is also enthalpy-driven, as observed from the absorption data presented in Chapter 2. In the case

of fluorescence data, the intensity quenching arises predominantly from base stacking effects. Thus, the free energies are expected to reflect the thermodynamics associated with single guanine residue, with G1 and G2 less stable than G11 (Figure 3.13B). As expected, ΔG_{local} values are less favorable for terminal guanine residues, but more significant for center tetrad and loop regions. The magnitudes of ΔH, $T\Delta S$ and $T\Delta G$ values are similar to global UV data, suggesting base interaction is a predominant and significant stabilizing influence on the overall "global" conformation as the quadruplex folds.

Table 3.3. Fluorescence melting temperatures for G-quadruplexes by 6MI-labeled human telomeric sequences in the presence of 100mM KCl or NaCl

Sequence	$T_{1/2}$ (°C)[a]		$\Delta T_{1/2(K^+-Na^+)}$(°C)[b]
	In 100mM K^+	In 100mM Na^+	
G1	44.6[c]	42.6[c]	2.0
G2	46.4	38.0[d]	8.4
G4	49.5	40.7	8.8
G5	51.9	30.5	21.4
G7	53.5	51.0	2.5
G9	47.6	34.8	12.8
G11	50.4	29.7	20.7
G12	48.8	42.3[c]	6.5

[a] $T_{1/2}$ was determined by analysis described on page 23 from the fluorescence melting curves, after corrections of simple thermal effects on 6MI fluorophore. Buffer condition was 10mM cacodylate (pH 7.2) with 100mM KCl or NaCl.

[b] $\Delta T_{1/2(K^+-Na^+)}$ is the difference of fluorescence melting points ($T_{1/2}$) between 100mM KCl and NaCl for same sequence.

[c] Fluorescence intensity increase on decreasing temperature for G1 in 100mM KCl or NaCl, and G12 in 100mM NaCl.

[d] Due to the obvious intensity change in G2's fluorescence melting curve (Figure 3.9A), $T_{1/2}$ of G2 in 100mM NaCl was roughly determined as the mid-point from the intensity quenching segment around 30-48°C in Figure 3.9C.

[e] Tm values for unlabeled HT_4 (from Chapter 2) are 61.9°C (in 100mM KCl) and 49.1°C (in 100mM NaCl).

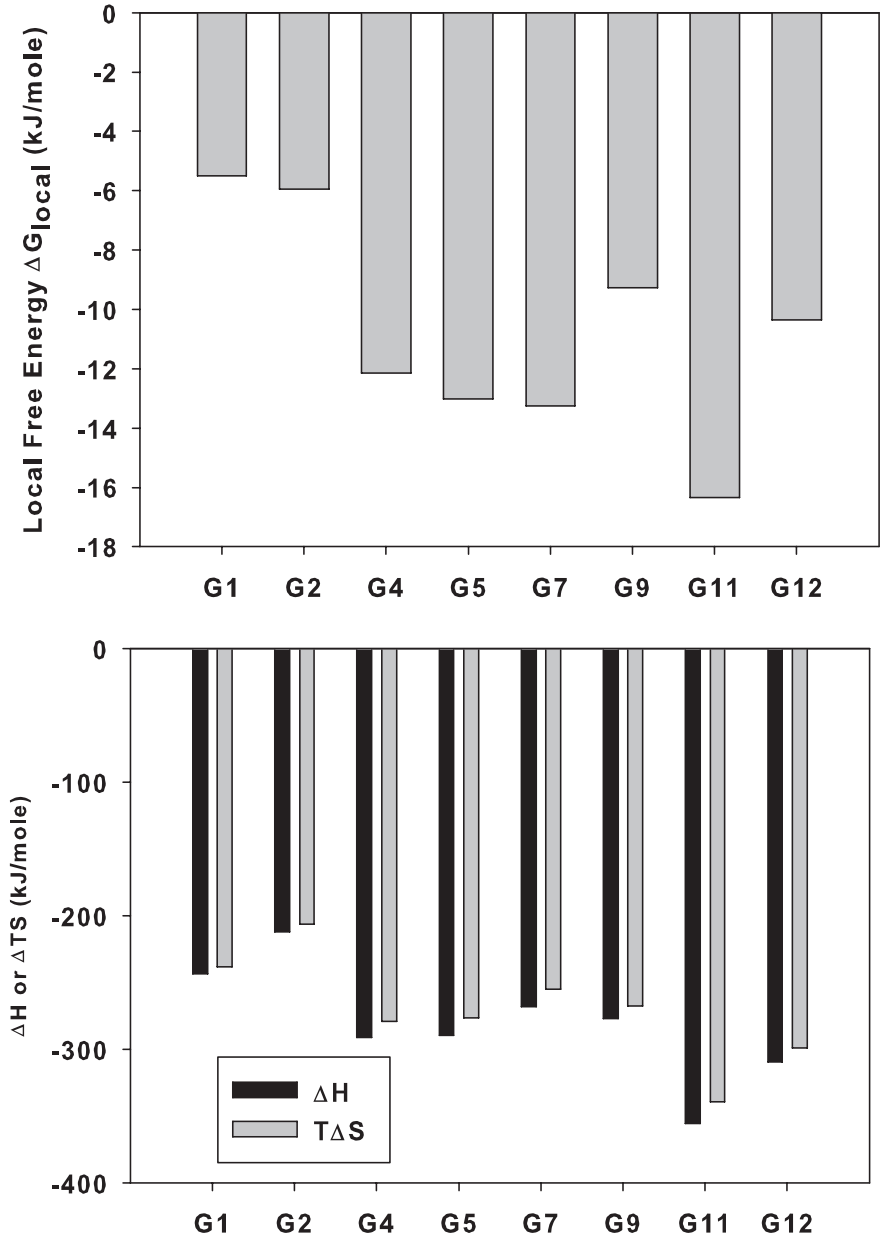

Figure 3.13. (A) Local free energy (ΔG_{local}) and (B) contributions of enthalpy (ΔH) and entropy ($T\Delta S$) at 37°C in 100mM KCl around 6MI probe to the folding of each labeled oligonucleotide to the quadruplex conformation.

3.3.3 Special case of G1

Substitution of the first guanine (G1) in the HT_4 sequence with 6MI, is an interesting and exceptional location within the sequence, which exhibits not only fluorescence intensity enhancement, but also spectral shifts to longer (red) wavelengths with quadruplex folding. This section will focus on the change of fluorescence intensity and peak wavelength shift of G1 with decreasing temperature that promotes quadruplex (annealing) formation.

Fluorescence intensity enhancement with quadruplex folding With 6MI substitution of guanine at G1 position, an increase in fluorescence intensity is observed on folding promoted by the presence of either KCl or NaCl in the buffer (Figure 3.14). However, for thermal studies in the absence of cation, where G-quadruplex exists in a random coiled/unfolded conformation across the temperature range examined, an increase in fluorescence intensity is also observed for G1 (Figure 3.14A) as a result of decreased thermal quenching of the incorporated 6MI fluorophore. An increase in intensity (thermal dequenching) is also observed for parent 6MI monomer (Figure 3.12) with decreasing temperature. Thus, the observed enhancement of fluorescent signal for G1-substituted oligonucleotide on addition of up to 100mM K^+ or Na^+-ions, reflects both a combination of fluorescence intensity changes (Figure 3.14A and B) arising from conformational changes (folding) together with intensity enhancement due to decreased thermal quenching of 6MI.

To test that the observed fluorescence intensity enhancement was related to quadruplex formation arising from annealing of the oligonucleotide samples, we examined the intensity changes in 40mM KCl or NaCl buffer and compared the results to those noted in the presence of 100mM. As expected, with lower concentration (40mM) of KCl or NaCl, the sigmoidal folding curves are shifted to lower temperatures relative to that noted in 100mM, resulting in lower $T_{1/2}$ values, which agrees with the observed lower absorption Tm values in the presence of reduced concentrations of KCl or NaCl. Studies by other groups have shown that a lower cation concentration results in a weaker stability of the quadruplex [93]. Our data also shows that with decreasing concentrations of K^+ or Na^+ cation, the thermodynamic stability of

the quadruplex is weaker, which is reflected by the fluorescence sensitivity of G1. Thus, the sigmoidal intensity-temperature profiles observed in the presence of monovalent cations are related to conformational effects reported by the 6MI fluorophore located at G1 position and engaged in quadruplex formation, and may not be accounted exclusively by simple thermal effects on the reported fluorescence intensities.

Emission spectral shifts on quadruplex folding: For studies of thermal effects on the folding of the G1-substituted quadruplex, we also observed a long (red) wavelength shift in its emission spectra accompanying the fluorescence intensity enhancement, resulting from quadruplex folding with a decrease in temperature. In 100mM KCl, around a 10nm shift to longer wavelengths is observed for the folded (<40°C) relative to the unfolded (>60°C) conformation (Figure 3.15B). In 100mM NaCl, this long wavelength spectral shift decreases to around 5nm (Figure 3.15B). Interestingly, no peak wavelength shifts were detected for the G1 sequence in the absence of K^+ or Na^+ (Figure 3.15A), suggesting that the observed spectral shifts are a direct result of quadruplex formation that arise from an altered micro-environment around the 6MI. Figure 3.16 summarizes the center of spectral mass versus temperature profiles for G1 with KCl or NaCl. Remarkably, the csm for G1 appears to mirror the folding/unfolding sigmoidal-profile (Figure 3.16), and demonstrates sensitivity of G1 to the conformational state of the quadruplex. No significant wavelength shifts were observed for the negative control (G1 without KCl or NaCl).

Table 3.4 summarizes the transition temperatures obtained from the csm-temperature data (T_{csm}) shown in Figure 3.16. Similar to T_m (from absorbance melting) and $T_{1/2}$ (from fluorescence melting), T_{csm} is also dependent on the type (K^+ *vs.* Na^+) and concentration (40mM *vs.* 100mM) of cation. Under the same concentration (40mM or 100mM) of cations, T_{csm} in K^+ is higher than for Na^+. In presence of same type of cation (K^+ or Na^+), T_{csm} in 100mM is higher than in 40mM. The origins of the enhanced fluorescence intensity for G1 during folding, appear to reflect local solvent effects given that additional base stacking from neighboring bases (from intensity quenching) appears minimal with folding. A possible

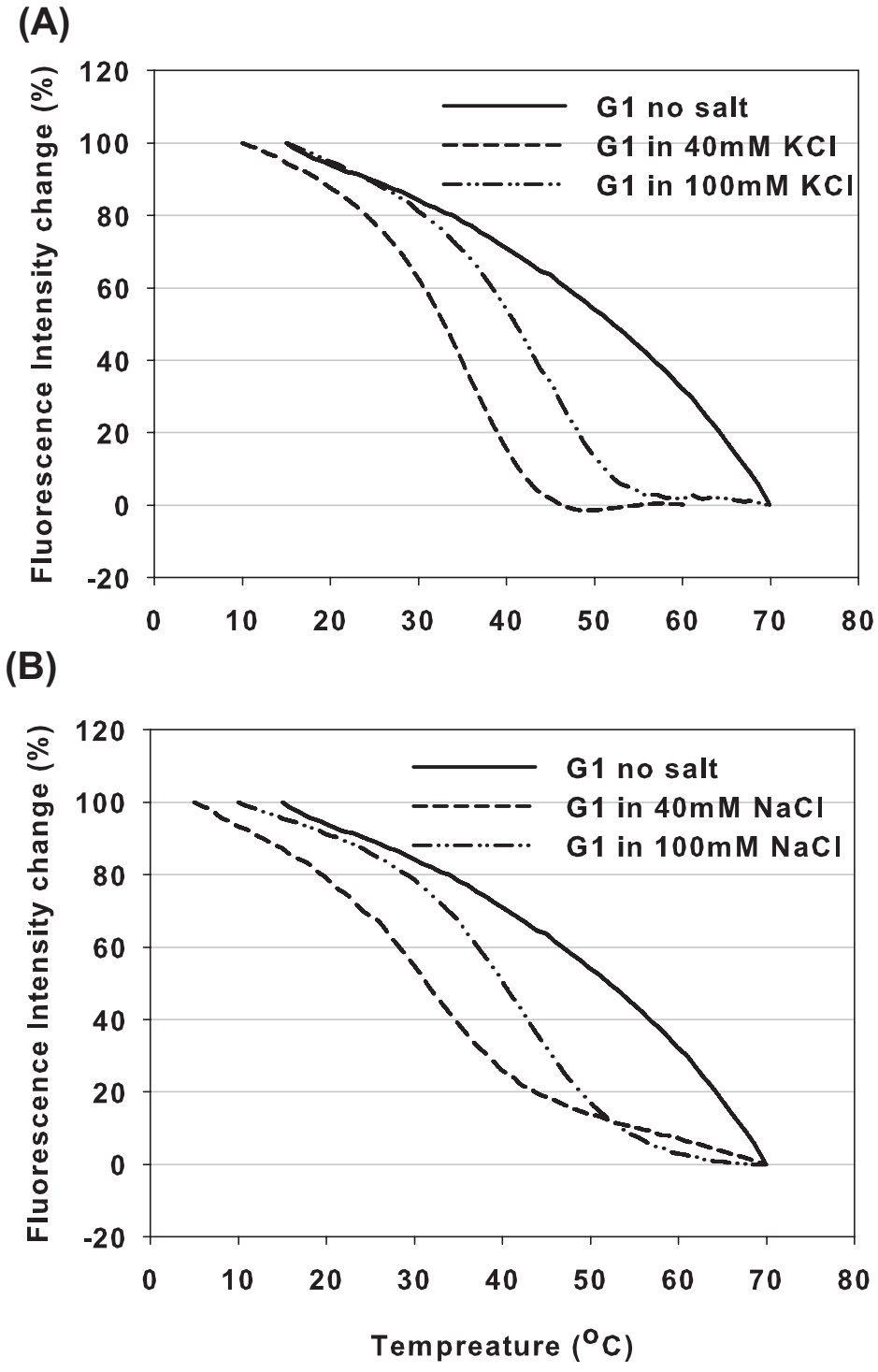

Figure 3.14. Normalized fluorescence intensity change for G1 in cacodylate buffer (pH 7.2) alone ("no salt"), and with 40mM or 100mM (A) KCl or (B) NaCl. Fluorescence intensity change percentage was calculated from $(F_T - F_{100})/(F_0 - F_{100})$, where F_T is the integrated fluorescence intensity at temperature T, and F_0 and F_{100} are the intensity values at the lowest and highest temperatures, respectively.

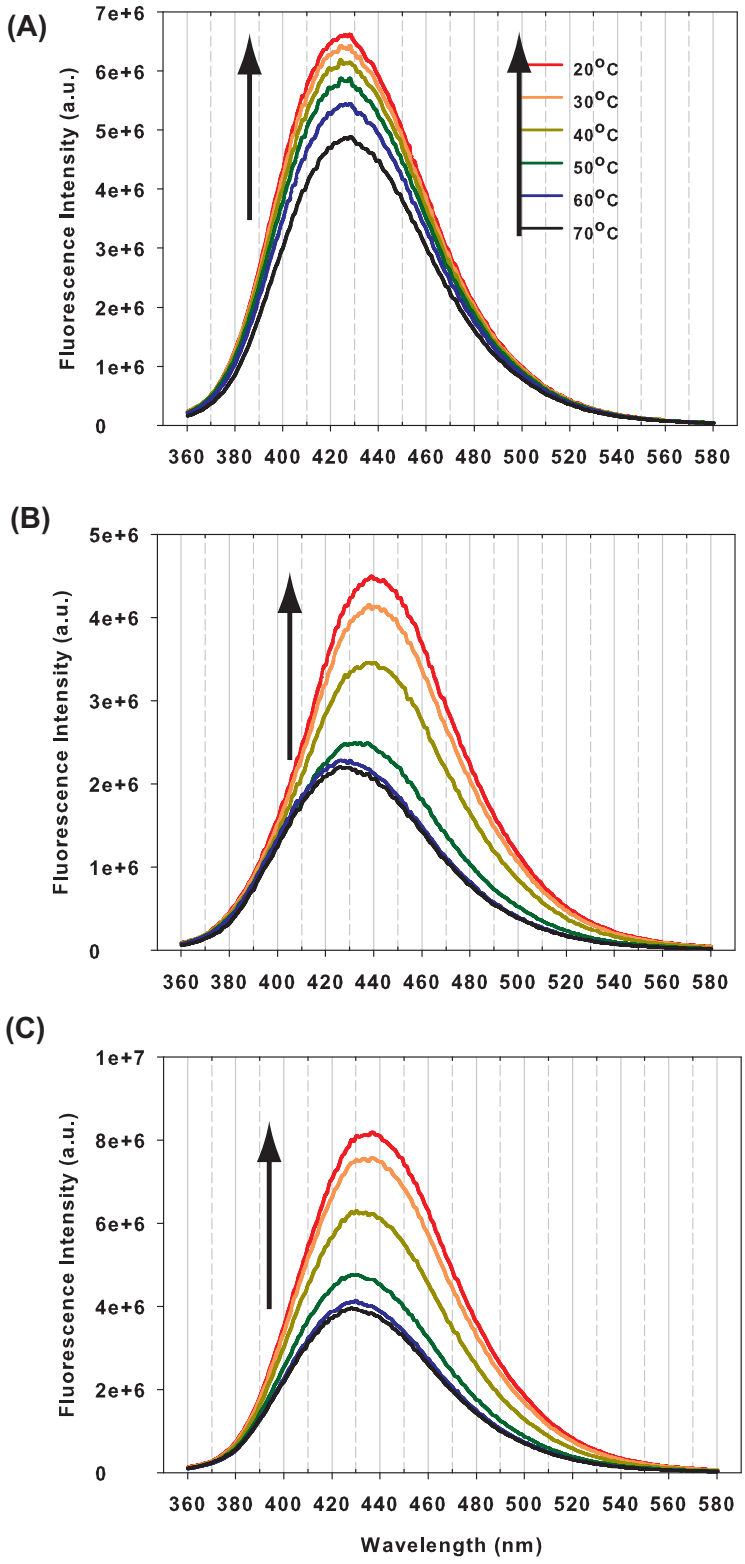

Figure 3.15. Fluorescence spectra of G1 in (A) 10mM cacodylate(pH 7.2) or (B) with additional 100mM KCl or (C) with additional 100mM NaCl every 10°C. Arrows point to spectra with decreasing temperature from 70 to 20°C.

model involves a ground-state H-bonding species for G1, with a corresponding enhanced quantum yield for the deprotonated form of G1. Further models are discussed in Chapter 6.

Table 3.4. Center of spectral mass melting temperatures for G1 in the presence of KCl or NaCl

Buffer condition[a]	T_{csm} (°C)[b]	CSM[c]		Spectral shift (nm)[d]
		Unfolded (nm)	Folded (nm)	
100mM KCl	47.9	438.7	448.3	9.6
40mM KCl	40.2	439.2	450	10.8
100mM NaCl	41.5	440.4	445.5	5.1
40mM NaCl	31.6	437.5	443.5	6.0

[a] Buffer condition was 10mM cacodylate (pH 7.2) with different concentration of KCl or NaCl.

[b] T_{csm} was determined as the mid-point temperature from the csm melting curve in Figure 3.16.

[c] Assuming the fluorescence melting study of G1 follows the all-or-none model, the CSM of the unfolded and folded state were determined from the CSM at the lowest (∼15°C) and highest(∼70°C) temperature respectively.

[d] Spectral shift was calculated from CSM_F-CSM_U, where CSM_F and CSM_U were the CSM of folded and unfolded state.

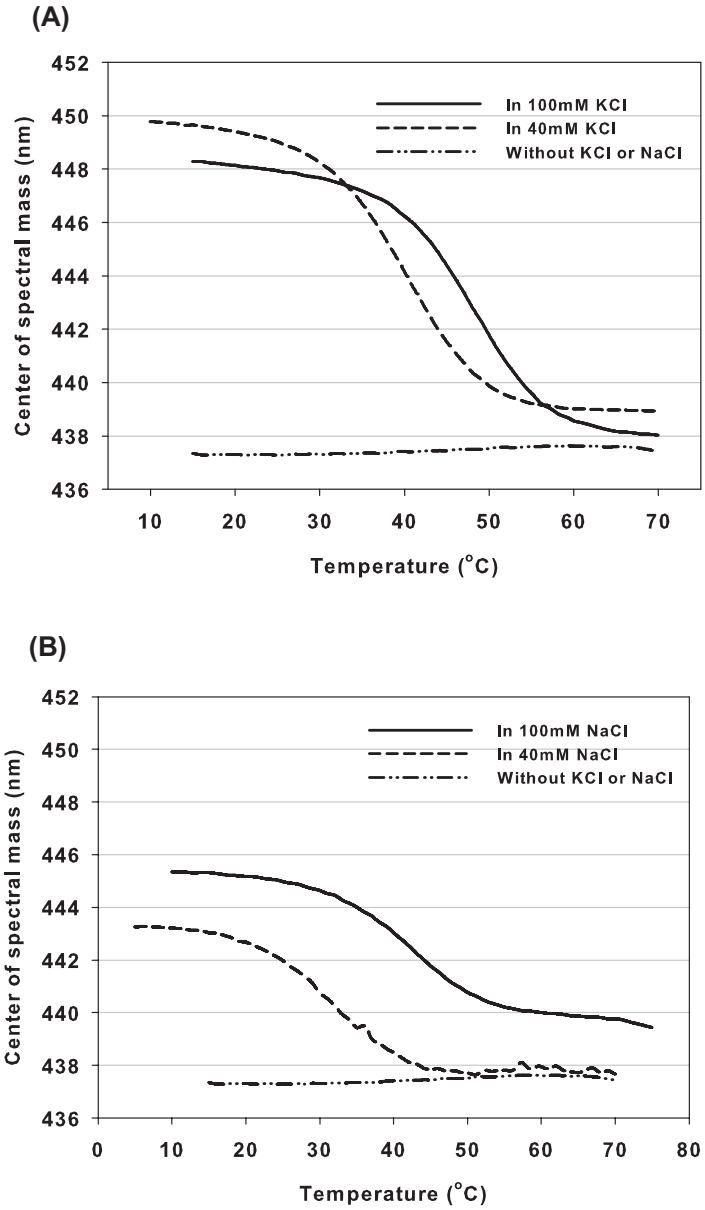

Figure 3.16. Center of spectral mass against temperature for G1 in absence of KCl or NaCl, and in 40mM and 100mM of (A)KCl or (B)NaCl. Center of spectral mass(csm) was calculated from $\frac{\sum \lambda_i I_i}{I_i}$, where I_i stands for the fluorescence intensity emitted at wavelength λ_i.

Three quadruplex folding/unfolding profiles of G1 We have used three different spectroscopic parameters: absorbance values; integrated fluorescence intensity; and center of spectra mass to monitor the effects of altered temperature of the formation of the G-quadruplex using the 6MI probe substituted at the G1 sequence. For G1, if each of these properties represents measurement of a special conformational event, the three events can be separated thermodynamically from each other. The special conformational events include: global quadruplex formation (measured by absorbance values change); local base pairing (fluorescence intensity measurements); interaction with solvent (wavelength shifts of emission spectra) or other local interactions around G1 involved during quadruplex folding.

As shown in Figure 3.17 and Table 3.5, the absorbance, fluorescence intensity and csm phase data have been converted into fractions of quadruplex folded in the presence of KCl. The these three folding profiles and their corresponding mid-point transition temperatures are well separated from each other, following the order: $T_{Abs} > T_{csm} > T_{1/2}$.

The unexpected enhancement of fluorescence intensity of G1 upon folding into the G-quadruplex, as a result of either decreasing temperature (Figure 3.14) or increased concentration of K^+-ion concentration (Figure 3.4A on page 55), suggests that guanine 1 is not significantly involved in neighboring base stacking interactions. Furthermore, the emission spectral shift to longer wavelength provides additional evidence that G1 is flexible and solvent accessible in the folded quadruplex conformation. Therefore, the relatively high T_{Abs} value may arise as a result of minimal participation of G1 in the overall global thermodynamics of folding.

From the quadruplex folding plots (Figures 3.17 and 3.18), the temperature values for T_{csm} and $T_{1/2}$ suggest sensitivity of the G1 position to local events occurring prior to the main unfolding transition and possible local strand fraying of the 5'-end prior to global unfolding of the quadruplex. The sensitivity of the quadruplex at position G1 to local effects is dependent on the cation concentration and nature of the cation present. For K^+-stabilized quadruplex, solvent effects, reflected by T_{csm} is on the order of $\sim$4°C higher than measured for $T_{1/2}$, in both 40mM and 100mM KCl. Hence solvent rearrangements appear to occur

after folding. On switching to Na^+-ion in the buffer, T_{csm} and T_{FL} converge with each other. Therefore, the two local events for G1 occur simultaneously for the Na^+-stabilized quadruplex.

Although the origins of the fluorescence intensity enhancement and the emission spectral shifts for G1 on quadruplex folding are still unclear, change of these two spectrophotometric properties for G1 can provide insights into the local interactions, other than base stacking, that are involved in quadruplex formation, and also serve as a novel indicator for quadruplex formation as induced by QIAs.

Table 3.5. Summary of three melting points for G1

Buffer condition	T_{Abs} (°C)[a]	T_{FL} (°C)[b]	T_{csm} (°C)[c]
100mM KCl	53.7	44.5	47.9
40mM KCl	44.7	36.0	40.2
100mM NaCl	45.0	42.6	41.5
40mM NaCl	35.1	32.1	31.6

Note: T_{Abs} is the from absorbance melting profile (Table 2.1 on page 32), T_{FL} is from fluorescence melting profile (Table 3.3 on page 66) and T_{csm} is from CSM transition (Table 3.4 on page 72).

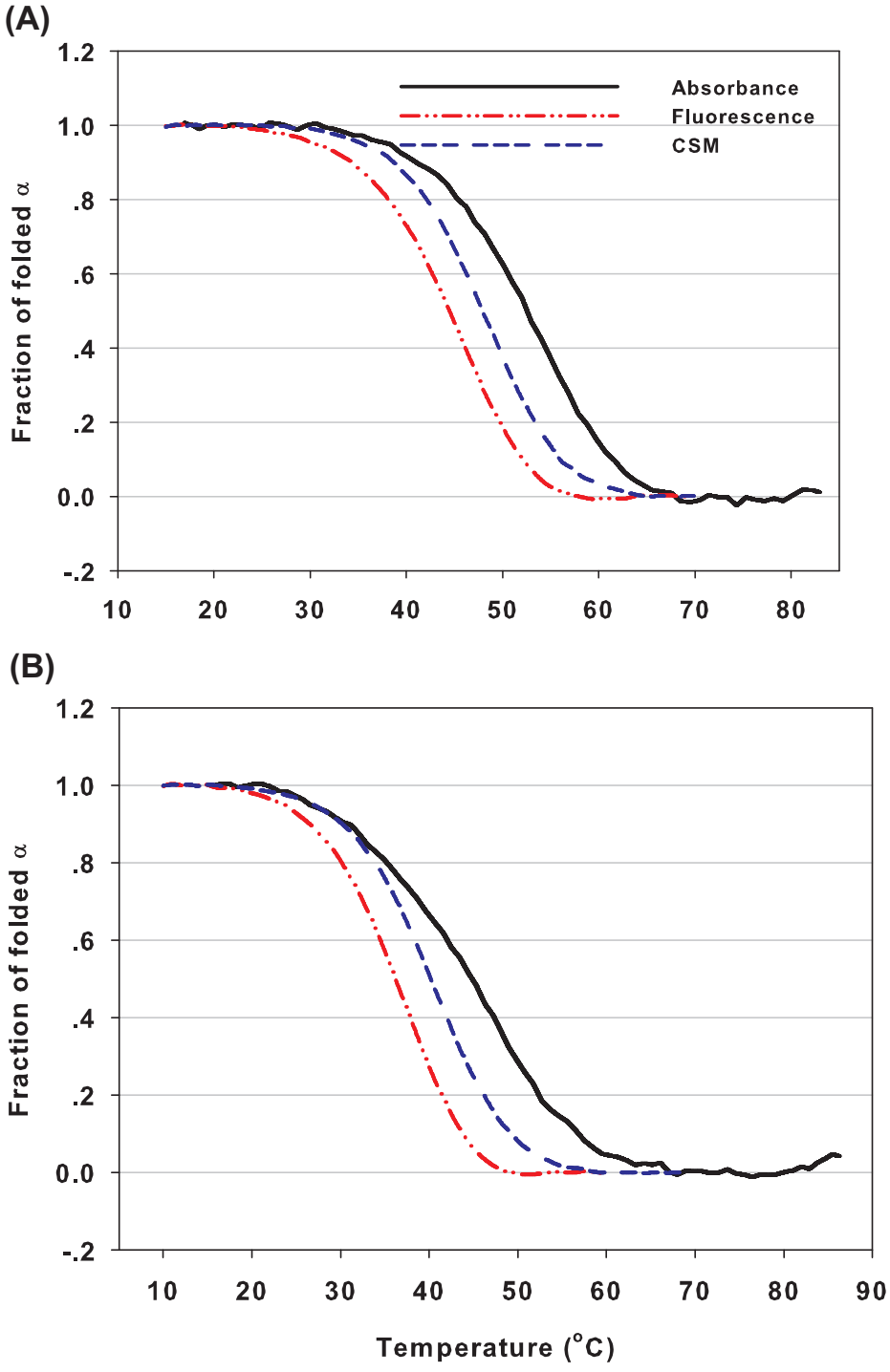

Figure 3.17. Fractions of folded α against temperature from absorbance, fluorescence and csm melting curves in (A)100mM or (B)40mM KCl.

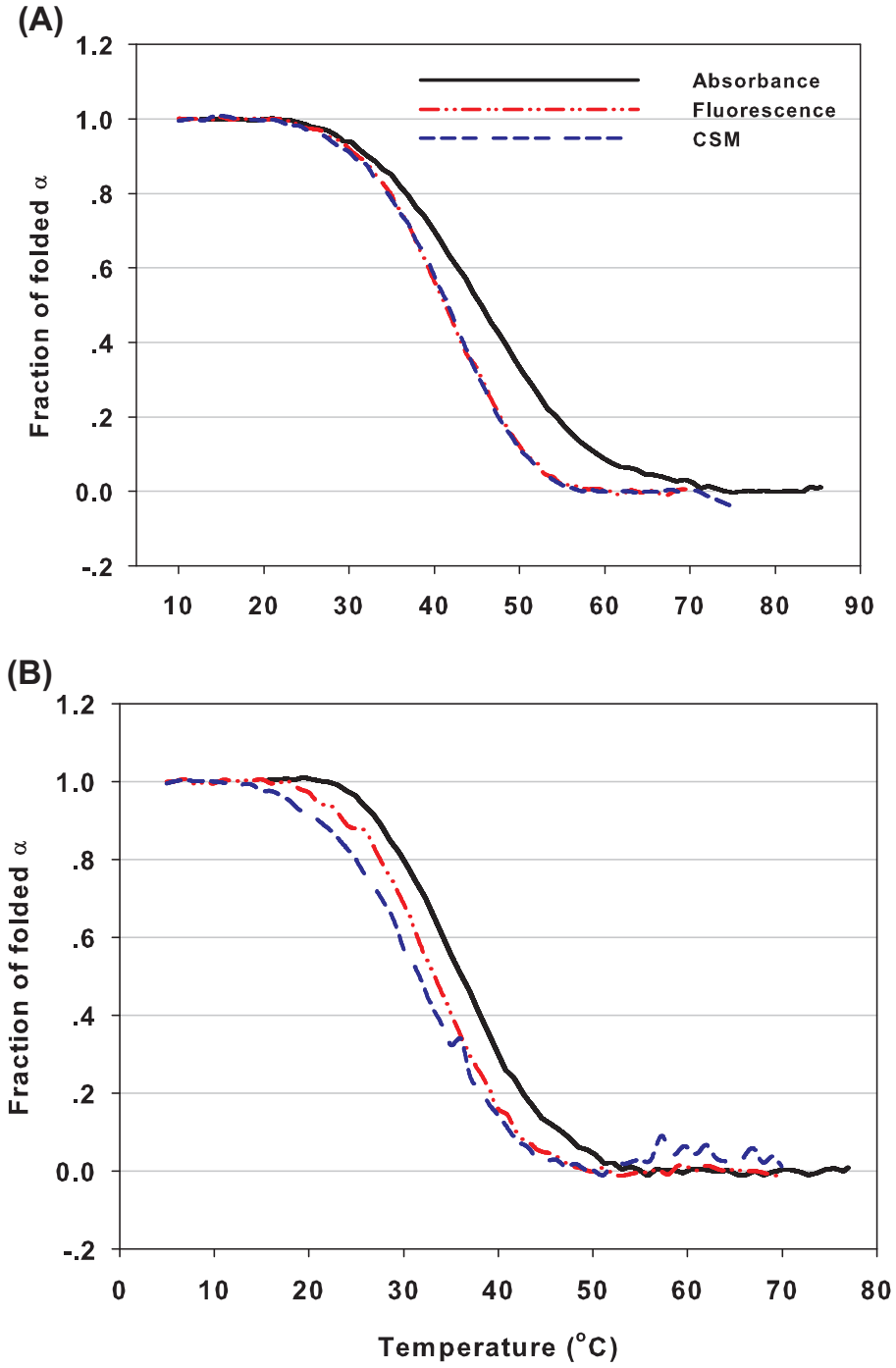

Figure 3.18. Fractions of folded α against temperature from absorbance, fluorescence and csm melting curves in (A)100mM or (B)40mM NaCl.

3.4 Summary

We have investigated local environmental changes around individual guanine positions using fluorescence signals from 6MI as a sensitive probe of its local environment. Upon decreasing temperature or addition of K^+, which promotes folding of the G-quadruplex, measured fluorescence intensity changes are different for each 6MI-labeled sequences, suggesting varying extents of base stacking interactions around the guanine positions.

Different values of $T_{1/2}$ from the fluorescence melting study and $K_{0.5}$ from the K^+ titration study for each 6MI-labeled sequence suggest a nucleation order for guanine participation in productive quadruplex folding. For quadruplex conformations stabilized by K^+, folding may initiate in the center tetrad involving G5 and G11, followed by G4 and G9 near the loop regions, and finally placing the terminal ends (G1, G2 and G12), which overall are quite flexible. Nucleation appears to occur at low K^+ concentrations whereas further stabilization requires higher (100mM) [K^+].

In contrast, for Na^+ initiated folding, guanine positions on the top G-tetrad (G1, G7 and G12) are able to participate and lock into the quadruplex conformation, followed by guanine positions located within the middle G-tetrad (G2, G5 and G11), although G1 and G7 labeled sequences appear to prefer a hybrid conformation usually stabilized by K^+-ions.

The G1 substituted sequence exhibits fluorescence intensity enhancement and spectral shift to longer wavelength upon quadruplex formation, suggesting that base stacking interactions are less significant for guanine position 1 and may actually fray in solution, which may play an important role in biological function. Understanding the local interactions around each guanine residues can provide insights into the HT_4 quadruplex conformation dynamics under physiological relevant conditions and a better rationale for anti-cancer drug design that target binding to the HT_4 G-quadruplex.

Chapter 4

TIME-RESOLVED STUDY OF 6MI FLUORESCENCE DECAY

4.1 Introduction

Fluorescence intensity quenching of 6MI is observed with folding of the 6MI-labeled sequences on addition of K^+ cations. To better understand the origins for the observed steady-state intensity quenching in terms of dynamic or static quenching mechanisms, we investigated the fluorescence intensity decay profiles for 6MI in the 6MI-labeled sequences (G1, G4, G5, G9 and G11) in either the presence or absence of K^+-ions (100mM). K^+ ions were used as the stabilizing cations, due to its physiological relevance with higher intracellular concentrations than Na^+. In general, our fluorescence lifetime measurements revealed a triple-exponential fluorescence decay for each 6MI-labeled oligonucleotide, either in the unfolded or folded quadruplex conformation, but a mono-exponential decay profile for the parent 6MI fluorophore. To examine the degree of lifetime heterogeneity, we collected decay-associated spectra (DAS) for G1 (near the 5'-end), G4 (loop region) and 6MI monomer, where lifetime components can be associated to spectral envelopes that contribute to the overall observed steady-state fluorescence emission spectra.

4.2 Materials and methods

Fluorescence Decay Measurements: Time-resolved fluorescence measurements were performed using time-correlated single-photon counting (TCSPC). Samples were excited at 335nm using an argon-ion laser synchronously pumping a frequency doubled, cavity dumped dye laser (repetition rate 4MHz, pulse width 2ps, average UV power <200 μW). Fluorescence decays were collected using magic angle polarization conditions with the emission monochromator set at 440nm using a GG400 filter in the emission path. The excitation pulse ("lamp") profiles were obtained with a light-scattering suspension (Ludox). Figure 4.1 shows a typical experimental fluorescence decay for G4 in 100mM KCl buffer collected together with the lamp excitation pulse. Typical peak counts were around 10000 photons. The channel width on the multichannel analyzer was 38ps, and data were collected using 512 channels.

Measured fluorescence decay profiles are distorted by lamp profile convolution artifacts, and the collected fluorescence intensity $R(t)$ (shown as red dots in Figure 4.1) is expressed as

$$R(t) = \int_0^t L(t')I(t'-t)dt' \tag{4.1}$$

where $I(t)$ is "the true fluorescence decay" of the fluorophore, $L(t)$ is the lamp function (response of the instrument to the laser excitation pulse) and $R(t)$ is the experimental response collected by the instrument after the excitation pulse from the lamp profile $L(t)$ [94]. Analysis of decay data includes both deconvolution of $L(t)$ from $R(t)$ to extract the true fluorescence decay $I(t)$, and the fitting of $I(t)$ to the following exponential decay expression:

$$I(t) = \sum_{i=1}^{n} \alpha_i e^{-t/\tau_i} \tag{4.2}$$

where $I(t)$ is the fluorescence intensity, α_i are the pre-exponential terms associated with the fluorescence lifetimes, τ_i. The data analysis were performed using in house analysis software *DecayFit 2.9.9*. "Goodness of fit" was assessed from residual and autocorrelation

functions combined with the χ^2 function. Total fluorescence intensity, $I = \sum_{i=1}^{n} \alpha_i \tau_i$, and the percentage intensity from each component contributing to the multiexponential decay model is given by: $\%I_i = (\alpha_i \tau_i / \sum_{i=1}^{n} \alpha_i \tau_i) \times 100$. Mean lifetimes (species weighted mean lifetime), $\langle \tau \rangle$ and radiative lifetime τ_{rad} are defined as

$$\langle \tau \rangle = \frac{\sum_{i=1}^{n} \alpha_i \tau_i}{\sum_{i=1}^{n} \alpha_i} \tag{4.3}$$

and

$$\tau_{rad} = \frac{\langle \tau \rangle}{\Phi}. \tag{4.4}$$

Absolute alpha (pre-exponential) values for each component were normalized to Φ as:

$$A_i = \alpha_i \left(\frac{\Phi}{\sum_{i=1}^{n} \alpha_i \tau_i}\right) \tag{4.5}$$

where Φ is the steady-state quantum yield value for the fluorophore. Absolute values for the alpha dark (A_{dark}) component arising from non-emissive decay pathways were calculated as

$$A_{dark} = \left(\frac{\tau_{std}^{exp}}{\tau_{rad}^{std}} - 1\right) \sum_{i=1}^{n} A_i, \tag{4.6}$$

where τ_{std}^{exp} is the radiative lifetime determined experimentally from equation 4.4, and τ_{rad}^{std} refers to the radiative lifetime of standard 6MI in buffer (8.7 ns).

Quantum Yield Measurement: Fluorescence quantum yields, Φ for each oligonucleotide in 10mM cacodylate (pH 7.2) buffer without or with 100mM KCl were determined relative to 6MI alone at 25°C, using the following equation:

$$\Phi = \frac{\Phi_{6MI} I_{DNA} Ab_{6MI}}{I_{6MI} Ab_{DNA}} \tag{4.7}$$

where Φ is the relative fluorescence quantum yield, subscripts 6MI and DNA denote 6MI alone and 6MI-containing oligonucleotide, respectively, I is the integrated fluorescence intensity, Ab is the absorbance at the excitation wavelength. The quantum yield for 6MI was

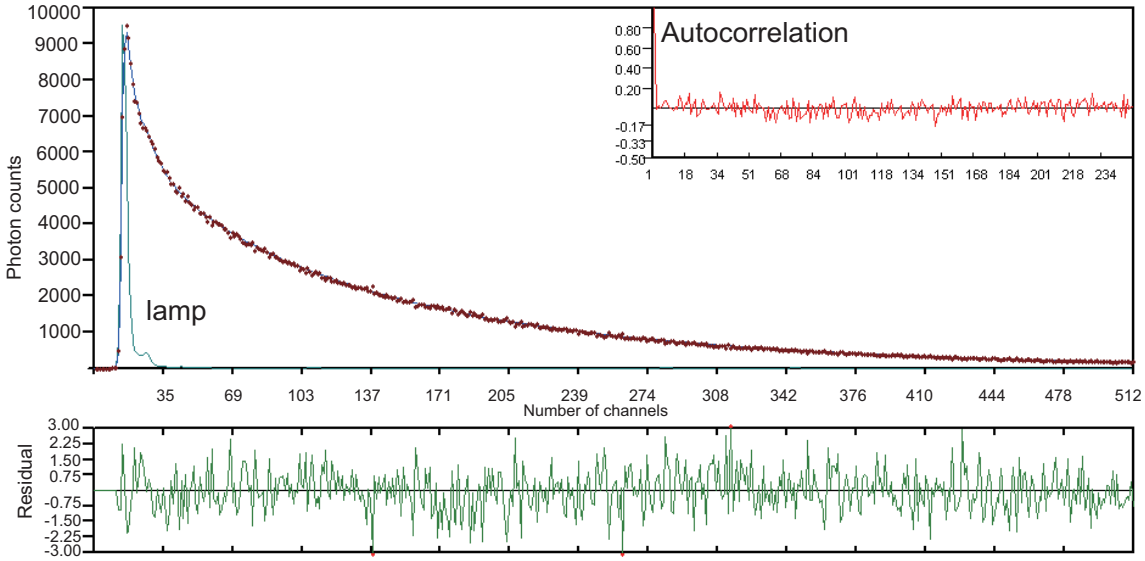

Figure 4.1. The instrument response $R(t)$ of G4 oligonucleotide in 10mM cacodylate (pH 7.2) and 100mM KCl after the lamp excitation pulse (initial peak in blue line) are shown in red dots. After the deconvolution analysis, the true fluorescence intensity $I(t)$ of the 6MI fluorophore were fitted to $I(t) = \sum_{i=1}^{n} \alpha_i e^{-t/\tau_i}$, where α_i are the pre-exponential terms associated with the fluorescence lifetimes, τ_i. Goodness of the fit is assessed by the randomness of the autocorrelation function (inset) and the residual plot (bottom). X-axis is shown as number of channels on the multichannel analyzer where each channel has a 38ps time width.

taken to be 0.70 as reported previously [76].

Decay associated spectra (DAS) measurements: DAS were resolved from fluorescence decay profiles, collected across the emission wavelength ranges from 390nm to 540nm with 10nm increment and laser excitation at 335nm. The intensity decays were then fit using the in house software *DAS 1.0.0* over the entire wavelength/decay 3D-matrix, using global analysis with linked τ values across the wavelengths:

$$I(\lambda, t) = \sum_i \alpha_i(\lambda) exp(-t/\tau_i), \tag{4.8}$$

where $\alpha_i(\lambda)$ are the emission wavelength-dependent pre-exponential factors and τ_i is the associated fluorescence decay times across the emission wavelength envelope [95]. Plots of $\alpha_i(\lambda)\tau_i$ *versus* λ provide the decay-associated spectra (DAS) and represent the spectral envelope associated with a particular decay component, or rate constant. The steady-state emission intensity contributed from component i at wavelength λ, $I_i(\lambda)$ can be expressed as

$$I_i(\lambda) = \frac{\alpha_i(\lambda)\tau_i I(\lambda)}{\sum_j \alpha_j(\lambda)\tau_j} \tag{4.9}$$

The product $\alpha_i(\lambda)\tau_i$ appears in the numerator because the steady-state intensity is proportional to this product, and the sum in the denominator is proportional to the total intensity.

4.3 Results and discussions

The steady-state fluorescence intensity of the 6MI fluorophore for each labeled HT_4 oligonucleotides examined is sensitive to local environmental effects arising from conformational changes during folding, as shown in Chapter 3. Generally, the origins for the observed fluorescence intensity quenching can arise from either static or dynamic effects. There are several experimental parameters which allow us to distinguish which mechanism is dominating, including any dependence of lifetime on solvent viscosity, concentration of quenchers and temperature. Thus, measuring the fluorescence lifetime decay in the absence and presence of a quencher, provides a convenient method for resolving a specific quenching mechanism.

In the current study, quenching of the 6MI-labeled oligonucleotides arises from G-quadruplex formation induced by addition of K^+ cations. Hence, our experiments compared the 6MI lifetime values for each oligonucleotide in 10mM cacodylate buffer without or with 100mM KCl, where the G-quadruplex is unfolded or folded, respectively.

4.3.1 Background of static and dynamic quenching

Quenching of the emission intensity, i.e. decrease of the quantum yield of a fluorophore F in the presence of quencher molecules Q can arise from either static or dynamic quenching. For static quenching, the fluorescence intensity decrease arises from the formation of the non-emitting FQ complex in ground state (Figure 4.2), within a critical radius surrounding F. With resulting decreasing numbers of free F molecules in solution, the observed intensity will decrease. However, when measuring the fluorescence lifetime, only those uncomplexed fluorophores will contribute to the fluorescence decay. Hence, the fluorescence lifetime values of the fluorophore F remains unchanged by the presence of static quencher. In general, a decrease in fluorescence quantum yield in the presence of a quencher, resulting in unchanged lifetime value suggests a static quenching mechanism; for a heterogeneous solution, $\langle\tau\rangle/\Phi > \tau_{rad}$ [96].

For dynamic quenching, the quencher species Q transiently collides and interacts with

the fluorophores F during their excited state, therefore the decay from the excited state to the ground state is affected (Figure 4.3). Since each F molecule in solution may potentially collide with the quencher Q during the decay process, the fluorescence lifetime τ of all F molecules will be affected by the presence of a dynamic quencher and become shortened compared to that in the absence of quenchers, τ_0. Therefore, the decrease of lifetime values in the presence of the quencher suggests a dynamic quenching model (Equation 4.4: $\langle\tau\rangle/\Phi = \tau_{rad}$) [96].

4.3.2 Fluorescence lifetime measurements

We have measured the fluorescence intensity decay profiles for 6MI in each of our 6MI-labeled oligonucleotides in the presence or absence of K^+-ions (100mM), where the G-quadruplex forming sequence is unfolded or folded, respectively. A summary of the measured fluorescence lifetimes, mean lifetime ($\langle\tau\rangle$) and corrected amplitudes for the parent 6MI monomer and 6MI-labeled DNA sequences are shown in Table 4.1.

The fluorescence decay for the parent 6MI monomer may be essentially represented as a mono-exponential decay function with a lifetime value of 6.1ns in the absence of K^+ ions. There was almost no change in fluorescence decay lifetimes in the presence of K^+ (6.1ns). Hence, observed changes in fluorescence lifetime values observed for the 6MI-labeled oligonucleotides must originate from local conformational effects, which may include base-stacking, ring flipping, or electron-transfer effects.

For all the labeled oligonucleotides examined (Table 4.1), we noted that a multi-exponential decay profile with three fluorescence lifetimes provided the best fit to the data, requiring a long lifetime component (between 4 and 7ns), a medium lifetime component (around 2ns) and a short (< 0.5ns) "fast" lifetime component.

Generally for a homogeneous decaying population of fluorophores, the observed fluorescence lifetime (τ_0) is related to the quantum yield (Φ), through the radiative lifetime (τ_{rad}; comparable with Equation 4.4):

$$\tau_0 = \Phi \times \tau_{rad}.$$

Hence, with a quenching of fluorescence intensity (decrease in Φ), a concurrent decrease in

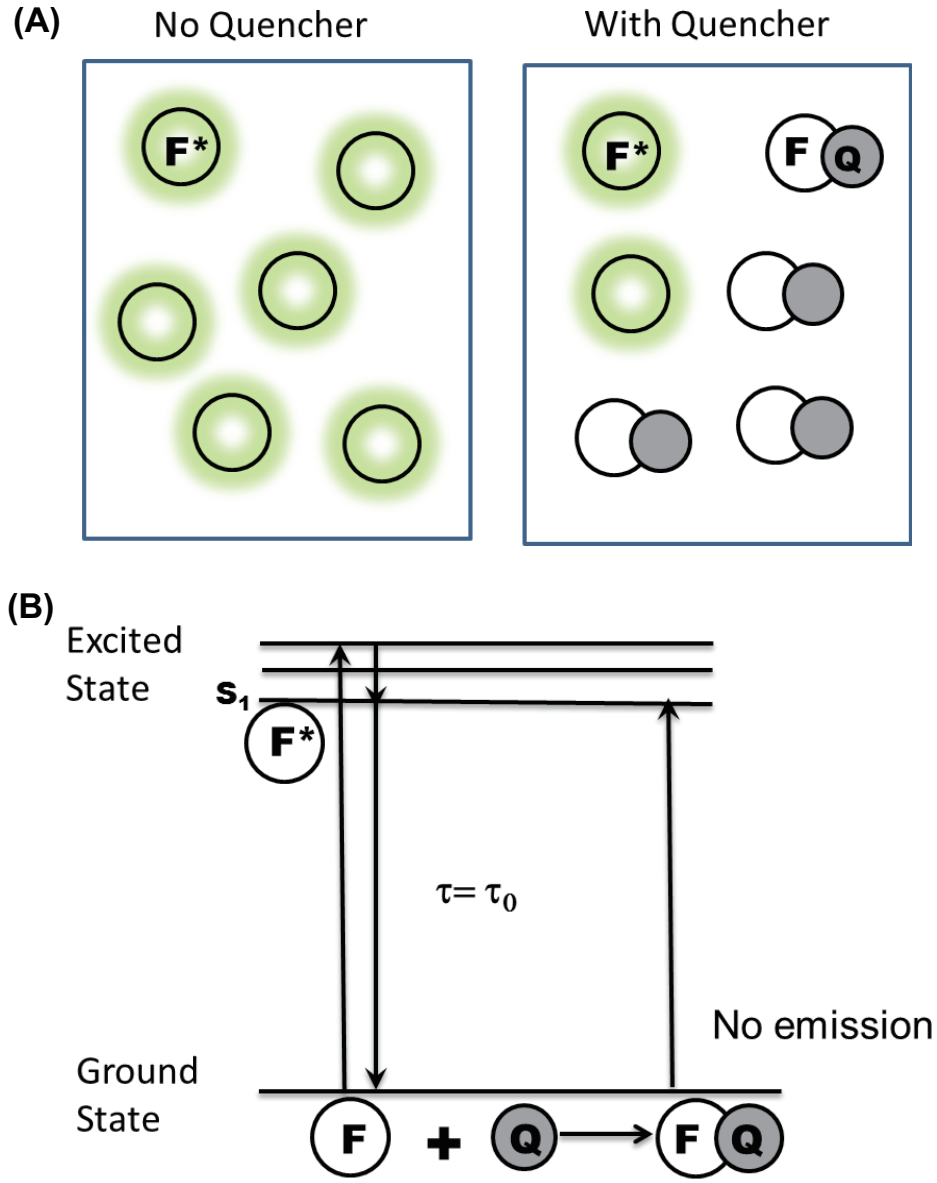

Figure 4.2. Scheme and Jablonski diagram of static quencher species Q interacting with fluorophores F in solution. (A) In the presence of quencher Q, the emission intensity per volume of concentration, i.e. quantum yield of the fluorophore F solution is quenched, due to the formation of the non-emitting FQ complex in ground state. (B) However, as shown in the Jablonski diagram, since the fluorescence lifetime measurement is based on the unbound fluorophore F in solution, the fluorescence lifetime value τ in the presence of quencher Q is unaffected and equals to τ_0, the lifetime of F measured in the absence of quencher Q. Thus, the fluorophores F shown in (A) in the absence or presence of quencher Q have the same decay lifetime values.

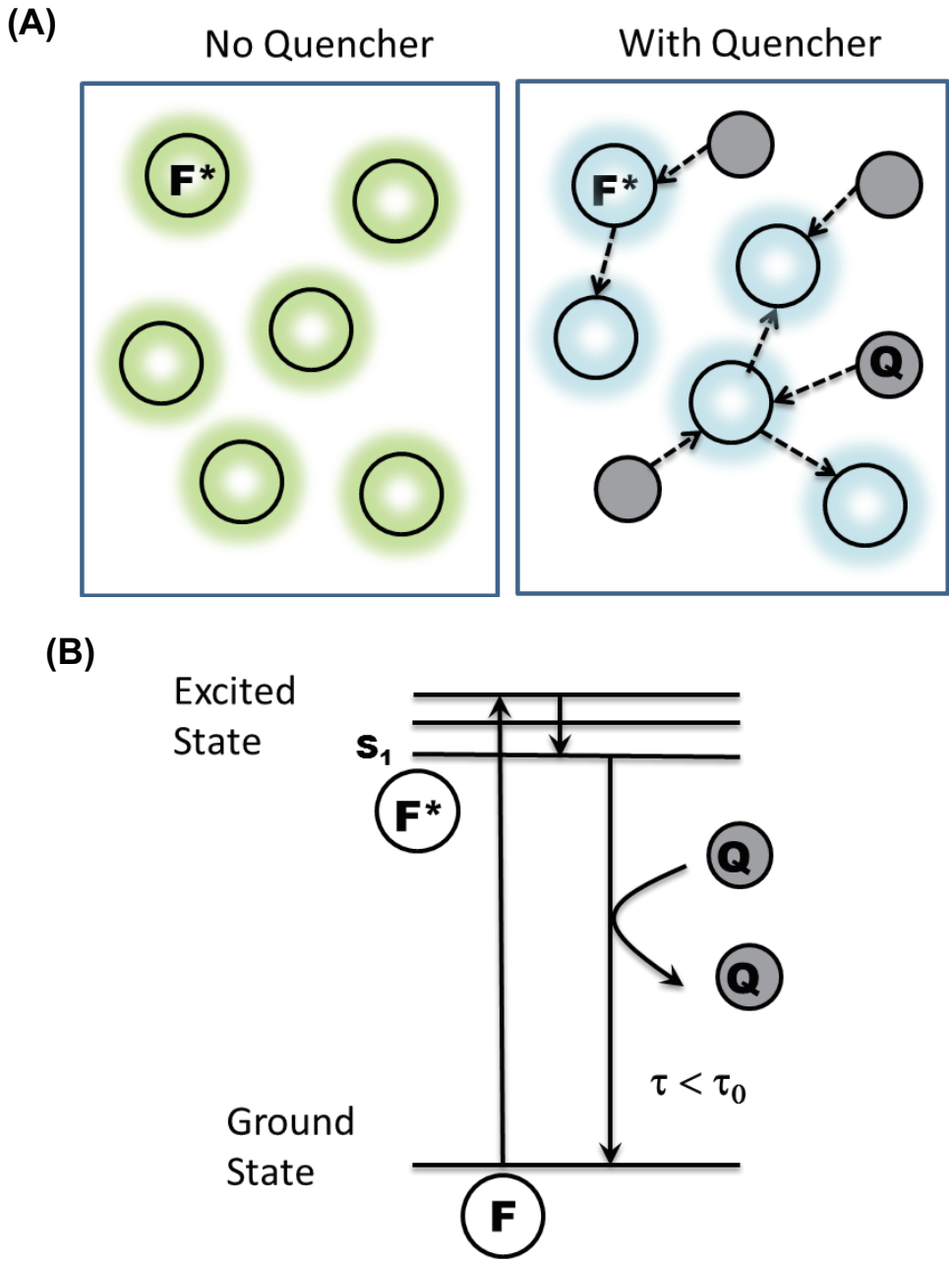

Figure 4.3. Scheme and Jablonski diagram of dynamic quencher species Q interacting with fluorophores F in solution. (A) In the absence of dynamic quencher Q, the fluorescence lifetime of the F fluorophores (green circles) is τ_0. In presence of Q, during the decay from the excited state to ground state, the fluorescence lifetime of F molecules (blue circles) will be affected due to the transient collisional interaction with quenchers Q in solution and shortened than τ_0.

the observed fluorescence lifetime (τ_0) is expected, since the radiative rate ($k_{rad} = 1/\tau_{rad}$) is an intrinsic property of the fluorophore and independent of macro-molecular conformation. For 6MI, using the published Φ value of 0.70 [76] combined with our measured (τ_0) lifetime value of $\sim$6.1ns, we have calculated a value of 8.7ns for τ_{rad} (see Table 4.1).

Table 4.1. Fluorescence lifetimes for 6MI monomer and 6MI-labeled oligonucleotides

Sequence	KCl present [a]	A_1	τ_1	A_2	τ_2	A_3	τ_3	A_{dark}	$\langle\tau\rangle$	Φ	τ_{rad}	χ^2 of fitting[b]
6MI	✓	0.1155	6.06							0.70[c]	8.66	1.05
		0.1150	6.09							0.70[c]	8.70	1.03
G1	✓	0.0045	7.01	0.0026	2.12	0.0043	0.37	0.1041	3.41	0.039	87.60	1.08
		0.0029	5.02	0.0030	1.54	0.0071	0.27	0.1026	1.61	0.021	77.55	1.13
G4	✓	0.0016	5.74	0.0007	2.01	0.0017	0.28	0.1116	2.75	0.011	256.00	1.09
		0.0025	4.70	0.0028	1.62	0.0109	0.26	0.0994	1.17	0.019	61.88	1.10
G5	✓	0.0009	5.87	0.0004	2.19	0.0004	0.40	0.1138	3.66	0.006	591.01	1.35
		0.0021	4.60	0.0027	1.90	0.0019	0.45	0.1087	2.33	0.016	147.66	0.98
G9	✓	0.0023	5.89	0.0013	1.77	0.0020	0.27	0.1098	2.92	0.017	175.76	1.01
		0.0061	4.54	0.0040	1.95	0.0032	0.33	0.1022	2.74	0.036	75.20	1.09
G11	✓	0.0019	6.59	0.0008	2.23	0.0008	0.27	0.1120	4.19	0.015	282.55	1.14
		0.0037	4.64	0.0036	2.42	0.0023	0.57	0.1060	2.83	0.027	105.14	1.22

[a] All measurements were taken at 25°C in 10mM cacodylate buffer, pH 7.2. KCl present indicates the presence (with tick) or absence (no tick) of 100mM KCl in the buffer.

[b] The χ^2 value is used to judge the goodness of fit, and is defined as $\chi^2 = \sum_{i=1}^{n} W_i[R(t)^{exp} - R(t)^{calc}]^2$, where W_i is the weighting factor on the data in the i^{th} channel of n total channels, $R(t)^{exp}$ and $R(t)^{calc}$ are the experimental and calculated fluorescence responses, respectively [94].

[c] Quantum yield value of 6MI monomer was taken from reference [76].

Abbreviations: A, absolute alpha values were corrected from $A_i = \alpha(\frac{\Phi}{\sum_{i=1}^{n} \alpha_i \tau_i})$, where α_i and τ_i are the pre-exponential and lifetime for each component of a multiexponential model respectively; A_{dark}, absolute alpha dark values calculated from Equation 4.6; $\langle\tau\rangle$, amplitude weighted mean lifetime; Φ, quantum yield; τ_{rad}, radiative lifetime.

4.3.3 Quasi static self quenching (QSSQ) in 6MI-labeled sequences

Quantum yield values for 6MI-containing oligonucleotides are significantly quenched, compared with the parent 6MI fluorophore (Table 4.1). Indeed, $\langle\tau\rangle/\Phi > \tau_{rad,6MI}$ for each labeled sequence, which suggests static quenching mechanism is a major contribution to the observed decreased quantum yield. With folding, $\tau_{rad,unfold} < \tau_{rad,fold}$, which indicates additional static quenching. In general, τ_2 and τ_3 were relatively insensitive to quadruplex folding in the presence of K^+, suggesting that the variation in observed amplitudes may reflect possible static (ground-state) quenching mechanisms (Table 4.1). However, comparison of the species weighted mean fluorescence lifetime values ($\langle\tau\rangle$, see Equation 4.3, page 81) for the labeled sequences in the folded (with K^+) quadruplex conformation *versus* the random conformation (without K^+), revealed a surprising increase in lifetime values (τ_1) coupled with the observed decrease in fluorescence intensity except for G1. Theory predicts that a decrease in the quantum yield Φ may not be coupled with an increase in fluorescence lifetime (Equation 4.4) [97]. Thus, the observed quenching of the steady-state fluorescence intensity of 6MI on folding to the quadruplex conformation (with K^+), is not adequately represented by either static (where lifetime values remain constant (Figure 4.2)), or dynamic mechanism (where both the quantum yield and lifetime values should decrease (Figure 4.3)).

A similar effect has been reported by Chen *et al.* [96], where the radiative lifetimes of several tryptophan dipeptides were unexpectedly longer than the lifetime measured for N-acetyltryptophan, the reference compound. The group proposed that the radiative lifetime inconsistency was a result of a "quasi static self quenching" (QSSQ) model. Here lifetime changes arising from QSSQ are excluded from a pure static quenching mechanism, and additionally can not be explained by a simple dynamic quenching mechanism. Rather, quasi static self quenching (QSSQ) arises from sub-picosecond ultrafast quenching processes (Figure 4.4), which occur immediately following the excitation of the fluorophore to the S_1 excited level. Suppose for a multi-component system, $\tau_2 << \tau_1$. As τ_2 approaches zero, $\alpha_2\tau_2$ is undetected. Under these conditions, one component would be effectively "quenched" through as apparent static method (QSSQ) [96]. Such rapid decay processes are difficult to

resolve from noise due to deconvolution difficulties. Hence, not all the lifetime components are resolved [96].

We have attributed the fluorescence quenching observed for 6MI in the labeled oligonucleotides arising from its incorporation into DNA to the QSSQ model, in addition to the intensity quenching observed as a result of K^+-induced quadruplex folding. In order to evaluate the magnitude of the "missing" ultra-fast decay component, from the quenched population for each oligonucleotide (with or without K^+), we calculated the pre-exponential amplitude associated with this "dark" decay component, "A_{dark}". Essentially,

$$A_{dark} = (\frac{\tau_{std}^{exp}}{\tau_{rad}^{std}} - 1) \sum_{i=1}^{n} A_i$$

where τ_{std}^{exp} is the radiative lifetime determined experimentally from equation 4.4 and shown in (Table 4.1), and τ_{rad}^{std} refers to the radiative lifetime of 6MI in buffer (8.7ns, as discussed previously). The absolute amplitudes (A_i) associated with the three extracted lifetimes for 6MI in the varying oligonucleotides (Table 4.1) were first corrected using the quantum yield values (equation 4.5, page 81), as summarized in Table 4.2 (shown as percentages).

As shown in Table 4.2, percentages for the "dark" deactivation state (A_{dark}) constitutes on average around 90% of the fluorescence decay for all the 6MI-labeled oligonucleotides in the unfolded state. The subpicosecond dark component is a major source for the decrease in quantum yields Φ values (from 0.7 for 6MI monomer to ~0.01 for G5 in Table 4.1) when 6MI is incorporated within the oligonucleotide environment. The dark component represents the extent of local base stacking interactions around the 6MI probe in the unfolded state. Interestingly, for the unfolded oligonucleotides, the weight of the "dark" deactivation pathway appears to vary with neighboring bases and is greatest for the base sequence -G-**F**-G- (G5, 94% and G11, 92%), and less for the sequences -A-**F**-G- (G1, 89% and G4, 86%) and -G-**F**-T- (G9, 86%), which are expected due to more efficient stacking of guanine-residues with 6MI [76].

As the 6MI-labeled oligonucleotides fold into quadruplex with addition of K^+, the per-

centage weights of A_{dark} further increase, due to enhanced base stacking and possible electron transfer deactivation from additional intrachain effects. The enhancement is greatest for base substitutions located near the TTA loop region (G4 and G9) in the bottom tetrad, over positions in the center tetrad (G5 and G11), and least for G1 near the 5'-end (Table 4.3). Such increases in the A_{dark} component on folding with K^+ addition suggest enhanced base interactions for 6MI-substituted guanine positions compared with the corresponding unfolded strands. No significant variation in the pre-exponential amplitudes with K^+ was seen for the 6MI monomer (A_1 equals to 0.1150 without K^+ and 0.1155 with K^+).

For G1, the 1% change of A_{dark} was less significant, which correlates with our observations that its emission intensity is not quenched with folding, but increases with K^+ addition on promoting quadruplex folding (Chapter 3), suggesting that the G1 position does not strongly base stack during the quadruplex folding process.

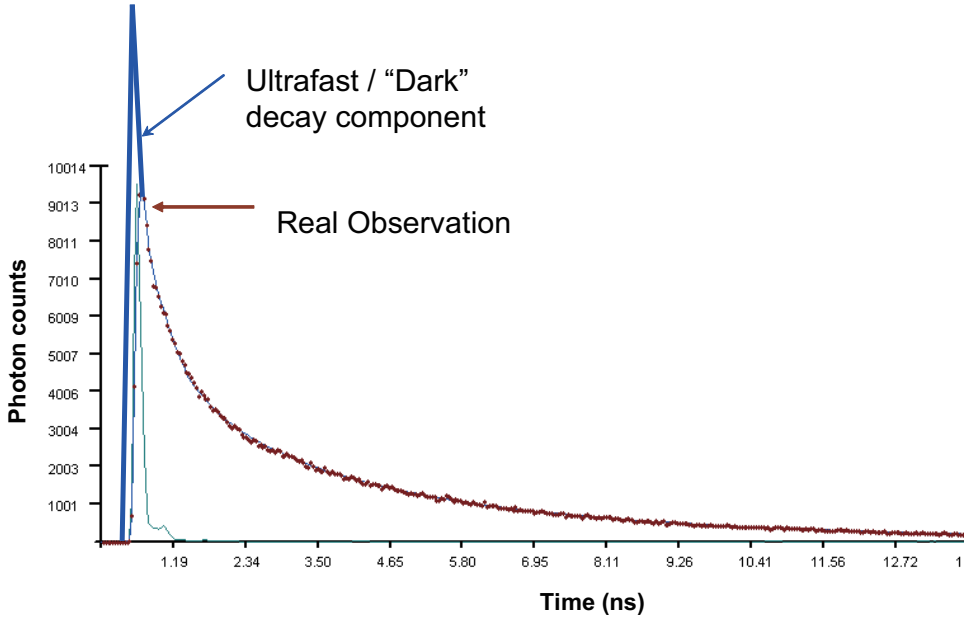

Figure 4.4. Scheme of quasi static self quenching (QSSQ). QSSQ occurs right after excitation. The dark component can not be resolved directly because it overlaps with the lamp excitation profile.

Table 4.2. Percentage of absolute alpha for 6MI-labeled sequences with or without KCl from Table 4.1

Sequence	Salt Environment	$A_1(\%)$	$A_2(\%)$	$A_3(\%)$	$A_{dark}(\%)$
G1	✓	3.94	2.25	3.70	90.12
		2.47	2.56	6.14	88.84
G4	✓	1.35	0.57	1.46	96.62
		2.13	2.41	9.45	86.01
G5	✓	0.76	0.33	0.37	98.54
		1.83	2.38	1.66	94.14
G9	✓	2.01	1.17	1.74	95.07
		5.24	3.50	2.77	88.49
G11	✓	1.67	0.73	0.66	96.94
		3.17	3.10	1.97	91.77

Note: percentage of each absolute value is calculated as $A_i(\%) = \frac{A_i}{\sum A_i}$.

Table 4.3. Neighboring bases around 6MI in 6MI-labeled sequences

Sequence	Neighboring bases (5'-3' direction)	Location	% Increase in A_{dark} on folding
G1	-A-**F**-G-	Top tetrad	1%
G4	-A-**F**-G-	Bottom tetrad	13%
G5	-G-**F**-G-	Center tetrad	5%
G9	-G-**F**-T-	Bottom tetrad	9%
G11	-G-**F**-G-	Center tetrad	5%

where **F**= 6MI

4.3.4 Decay-associated spectra of G1, G4 and G11

Background of Decay-Associated Spectra Fluorescence lifetime measurements for all 6MI-labeled oligonucleotides, in either the unfolded or folded conformations were best fit using a triple exponential decay function. However, the parent fluorophore, 6MI, exhibits a monoexponential fluorescence decay. The origins for the observed multiexponential decay for the 6MI fluorophore within the oligonucleotides could arise from the micro-heterogeneity due to the more complex local environment of the fluorophore residing in the oligonucleotide environment.

We have used decay-associated fluorescence spectra to unravel the lifetime heterogeneity for the G1, G4, and 6MI monomer. DAS can associate the lifetime or decay rates with a specific spectral envelopes underlying the overall steady-state emission spectra [98, 99]. This approach helps to unravel the origins of the heterogeneity in the deactivation pathways for the fluorophore as a result of its environment [76, 98]. For a mixture of two fluorophores with different lifetime values, DAS provides a method for resolving the measured emission spectral envelopes into the spectra associated with each fluorophore. However, multi-lifetimes for a single fluorophore are more challenging to resolve than a simple mixture of two fluorophores, and such lifetime heterogeneity may arise from a single fluorophore located within varying local and/or global environments, such as 6MI within quadruplex forming sequences. In our DAS study, an association is made between the intrinsic decay times of the spectral species, and their respective contributions to the steady-state emission intensity envelopes for the 6MI fluorophore when it is free, or as a guanine substitution in the unfolded or folded quadruplex.

4.3.5 DAS of 6MI, G1 and G4

Double Exponential DAS of 6MI For single curve analysis of 6MI in 10mM cacodylate buffer at 440nm, the fluorescence decay was fit using a mono-exponential decay profile. However, global analysis of the DAS that were collected for 6MI over the emission wavelength range (390-540nm) clearly revealed a small contribution from a second decay

component (τ_2 around 3.91ns shown in Table 4.4). The wavelength maximum (415nm) for the DAS associated with this fast decay component is shifted about 20nm to shorter wavelengths relative to the DAS (430nm) resolved for the major 6MI decay component (Figure 4.5A). The contribution of the blue-emitting DAS to the overall decay function is negligible at 440nm and hence is not easily resolved by single curve analysis collected at this emission wavelength. With addition of KCl (Figure 4.5B), the two lifetime values were essentially unchanged. While a small increase in the contribution of the DAS for the short lifetime component was observed, the contributions by the longer-wavelength DAS were reduced (Figure 4.5A relative to 4.5B). The decrease in the pre-exponential amplitude without change in lifetime, which is a signature of static quenching, may suggest possible complex formation for 6MI at higher (100mM) KCl concentrations. However, the observed effects appear to be small compared to the conformation heterogeneity effects observed for the 6MI-containing oligonucleotides.

The origins of the blue-wavelength shifted DAS for 6MI alone are unclear. Previously Hawkins *et al.* performed DAS for 6MI as a function of pH and also observed a very blue-wavelength DAS associated with a short lifetime component occurring around 400nm [76]. They attributed this DAS to a possible excited-state proton transfer reaction with a diagnostic negative amplitude occurring around 460-470nm. In our studies, we were unable to resolve a negative amplitude associated with our "blue" component (τ_2) at pH 7.2. Hence the origins of this component remain unclear, but may represent a population of 6MI molecules that are unrelaxed through solvent dynamics (e.g. deprotonation and/or solvent relaxation) or complexation (e.g. dimer formation or base stacking at higher ionic strengths). Further studies are required.

DAS for G1 and G4 DAS associated with the three lifetimes resolved for the decay of G1 and G4 were extracted (Figure 4.5C-F). G1 located near the 5'-end, as discussed above, shows an increase in fluorescence intensity with K^+-promoted folding, and provided an interesting application of DAS in an attempt to resolve the source of micro-heterogeneity.

Table 4.4. Decay times resolved from DAS for 6MI monomer and 6MI-labeled oligonucleotides

Sequence	Decay time (ns)	No Salt[a](csm[c])	In KCl[b](csm)	$\Delta\tau$ (Δcsm)[d]	% Increase[e]
6MI	τ_1	6.65 (440.0)	6.71(441.2)	0.06 (1.2)	0.90
	τ_2	3.91 (416.5)	3.98 (422.3)	0.07 (5.8)	1.79
G1	τ_1	4.87 (441.2)	8.30 (455.1)	3.43 (13.9)	70.73
	τ_2	1.81 (438.3)	3.47 (441.1)	1.66 (2.8)	91.91
	τ_3	0.31 (438.7)	0.49 (437.2)	0.18 (-1.5)	58.06
G4	τ_1	4.16 (436.0)	5.99 (437.6)	1.83 (1.5)	43.99
	τ_2	1.22 (438.0)	2.17 (434.7)	0.95 (-3.2)	77.87
	τ_3	0.25 (438.8)	0.40 (442.7)	0.15 (3.8)	60.00

[a,b] Samples were prepared in the buffer of 10mM cacodylate at pH 7.2 in the absence (No Salt[a]) or presence (In Salt[b]) of 100mM KCl.

[c] Center of spectral mass (csm)= $\frac{\sum \lambda_i I_i}{\sum I_i}$, where I_i stands for the fluorescence intensity emitted at wavelength λ_i.

[d] $\Delta\tau = \tau_{i,n} - \tau_{i,w}$ and Δcsm= csm$_{i,n}$− csm$_{i,w}$, where subscript n and w indicate the presence and absence of KCl in buffer respectively.

[e] %Increase = $\Delta\tau_i/\tau_{i,n} \times 100\%$, suggesting the relative increase of decay time of the sample from no salt to in salt environment.

In addition, we examined the G4 position, which lies next to the first TTA loop within the quadruplex.

For both sequences examined, a triple exponential decay best fit the fluorescence-intensity-decay data across the entire emission spectral envelope. A summary of the decay times for the unfolded and folded states of G1 and G4 is shown in Table 4.4. The three resolved DAS for G1 and G4 were associated with their respective decay times, τ_1, τ_2 and τ_3, representing the longest, medium and shortest lifetimes, respectively.

Compared to the 6MI monomer, one additional DAS component was resolved for G1 and G4. This is not surprising as incorporation of 6MI into an oligonucleotide results in a more complex environment for the fluorophore than when free in solution. In both the folded and unfolded quadruplex, three resolved DAS exist, but differ in the relative contribution of each to the total decay at each wavelength. Since the total spectral peaks of the DAS were normalized to 1, the relative contribution of deactivation pathways to the intensity in the

absence and presence of K^+-ion can be compared, as shown in Figure 4.6 for G1 and Figure 4.7 for G4.

As expected, the relative contribution of intensity, represented by the y-axis value "Alpha*T", are quenched "in salt" relative to "no salt" for both τ_2 and τ_3 for both G1 (Figure 4.6B and C) and G4 (Figure 4.7B and C). As suggested above, we propose that their intensity quenching originates predominantly from local base reorganization (including enhanced ground-state static quenching and rapid ring flipping mechanisms), arising from stronger base stacking interactions on quadruplex folding for G1 and G4. No significant spectral shifts were observed for these DAS, suggesting that deactivation pathways *via* the τ_2 and τ_3 deactivation routes contribute to the observed intensity quenching of the steady-state emission spectra, but not the emission wavelength shifts as observed during the folding of G1.

However, the steady-state emission spectral envelope is not solely a reflection of intensity quenching arising from base stacking, since a third deactivation route represented by τ_1 was also clearly present and was a dominant component for the decay (compared with τ_2 and τ_3) of the fluorophore. The increase of $\alpha_1\tau_1$ "in salt" relative to "no salt" for both G1 (Figure 4.6A) and G4 (Figure 4.7A) suggest that this component may not be solely related to base stacking interactions, but other environmental effects predominating around the fluorophore resulting in differing decay pathways.

For G1, the red-shifting of τ_1 (a_1t_1 "in KCl" *vs.* "no KCl" in Figure 4.6A) suggests that this position is more exposed to a polar environment when in the folded quadruplex. It is possible that this longest-decay-time component may be related to interaction of the fluorophore with its local (polar) environment, possibly through H-bonding as a consequence of its greater solvent exposure at the 5'-end of the sequence. Hence, the steady-state intensity enhancement and spectral red-shift we observe for G1 on quadruplex formation described in Chapter 3 arises predominantly from contributions (τ_1) of local environmental effect on this fluorophore population. Although the origins for the intensity increase for the τ_1 species for both G1 and G4 (Table 4.4) may not be determined definitively without further experimen-

tation, its existence suggest that the 6MI local environment within the HT_4 oligonucleotide is heterogenous and complex.

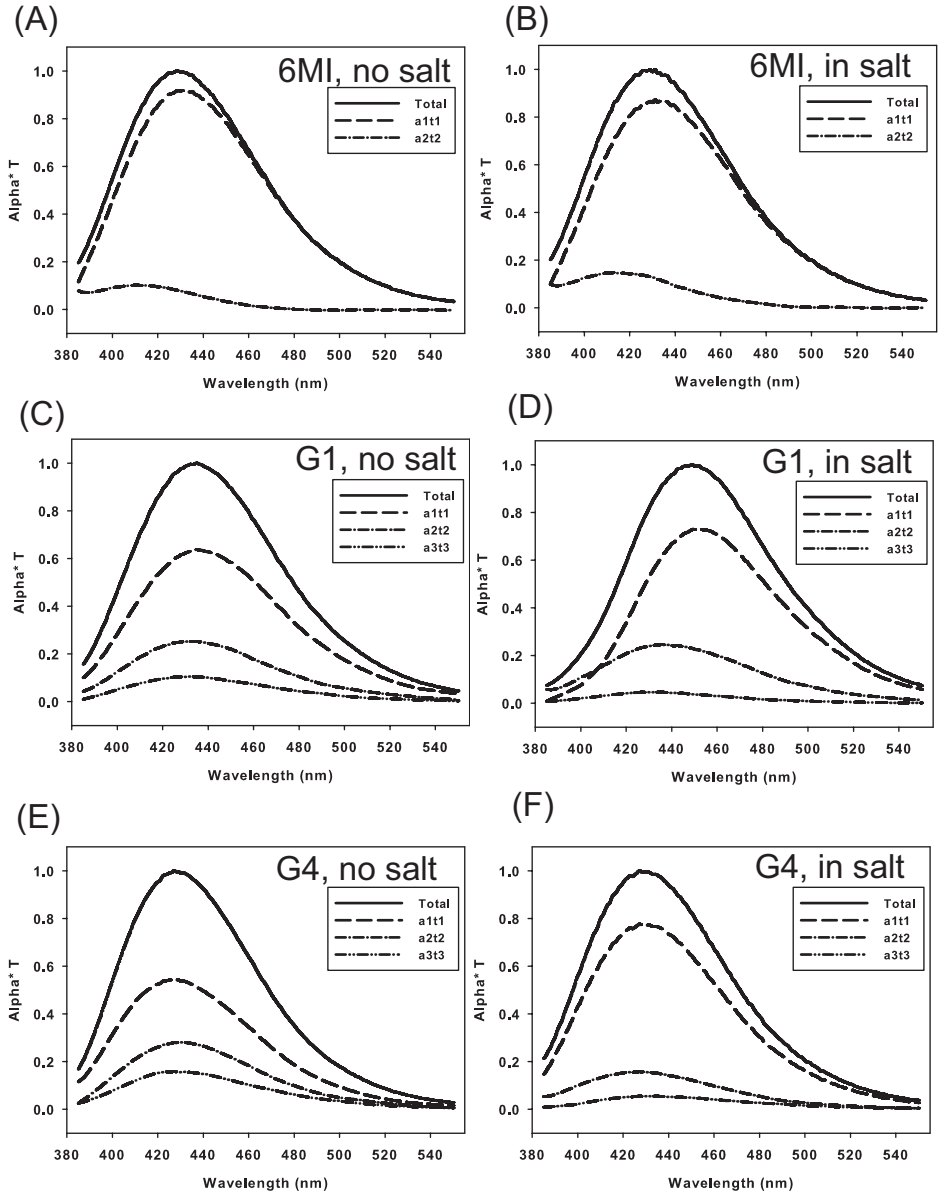

Figure 4.5. DAS for 6MI monomer ((A) and (B)), G1 ((C) and (D)) and G4 ((E) and (F)). Samples on left column are in 10mM cacodylate (pH 7.2) without KCl, and samples on right column are in 10mM cacodylate (pH 7.2) with 100mM KCl. Time-resolved fluorescence decay for each oligonucleotide was collected with excitation at 335nm and emission wavelength λ from 390nm to 540nm with 10nm increment. The fluorescence intensity at wavelength λ were fitted to $I(\lambda, t) = \sum_i \alpha_i(\lambda) exp(-t/\tau_i)$, where $\alpha_i(\lambda)$ is the wavelength-dependent pre-exponential factors and τ_i is the associated fluorescence decay time. The total value at each wavelength λ is the sum of all $\alpha_i(\lambda)\tau_i(\lambda)$, and the max value in the "total" around 430nm was normalized to 1. Two decay time values were resolved for 6MI monomer and three values for G1 and G4. τ_1, τ_2 and τ_3 refer to their longest, medium and short decay time values, respectively.

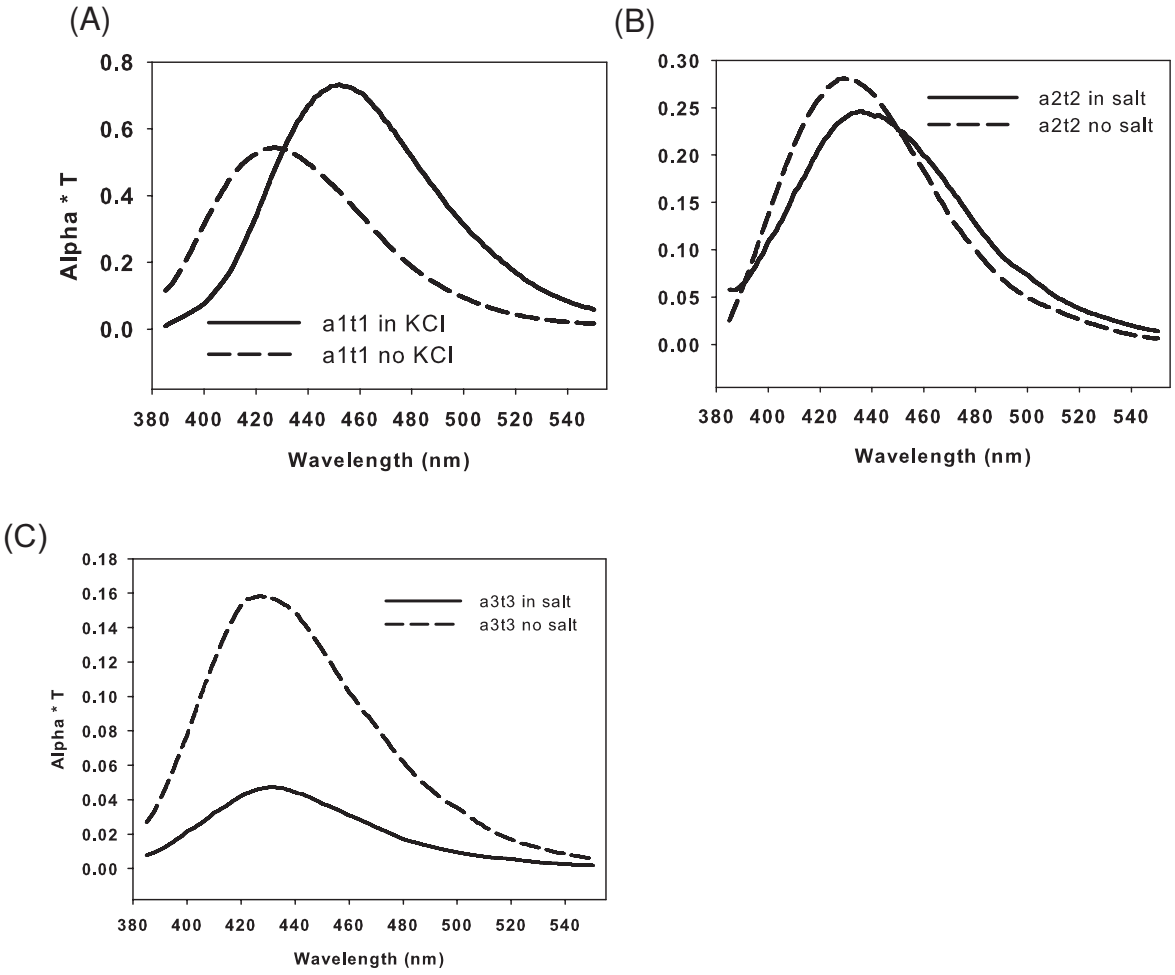

Figure 4.6. DAS of G1 in 10mM cacodylate (pH 7.2) buffer without ("no salt", dash line) or with 100mM KCl ("in salt", solid line) for its (A) longest τ_1, (B) medium τ_2 and (C) shortest τ_3 decay times.

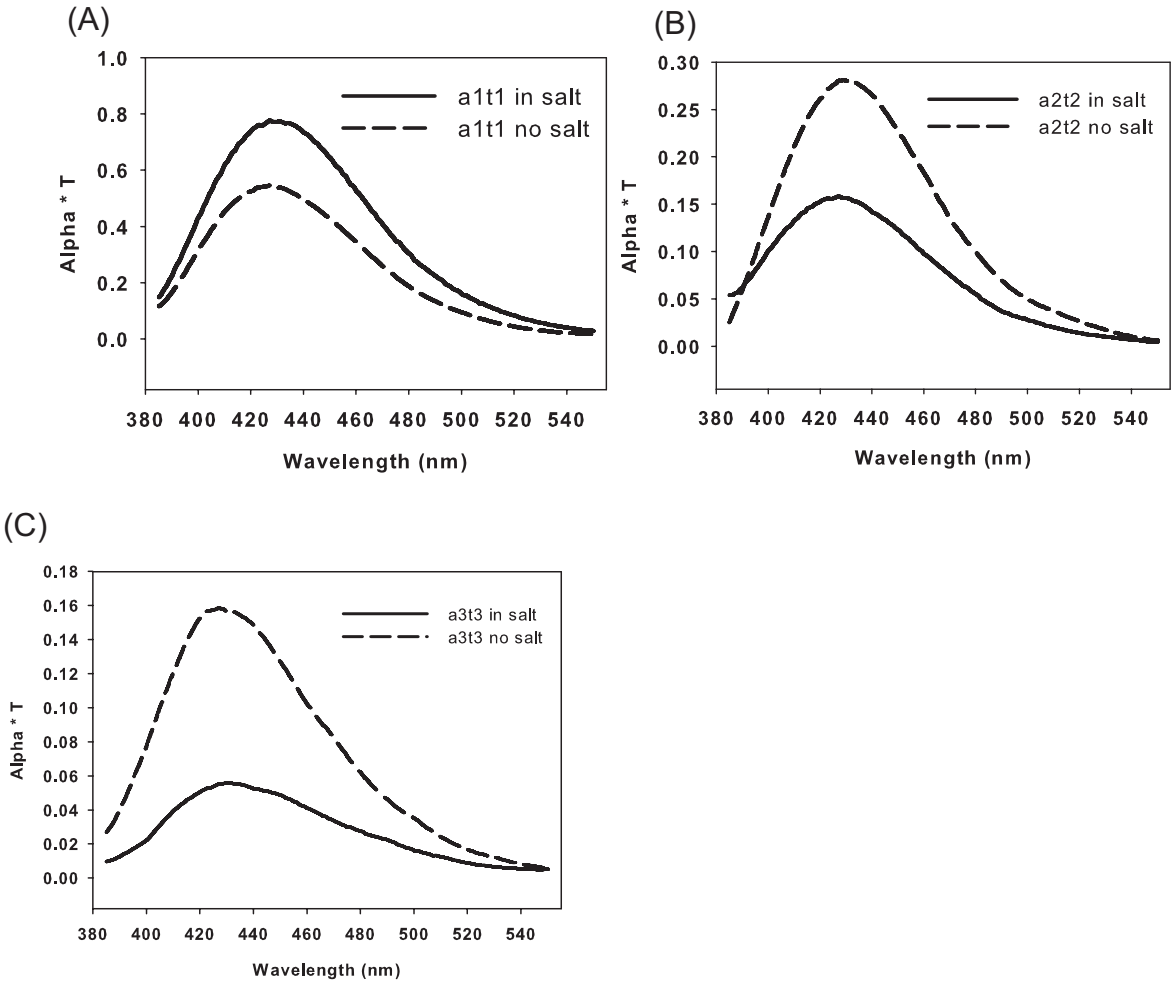

Figure 4.7. DAS of G4 in 10mM cacodylate (pH 7.2) buffer without ("no salt", dash line) or with 100mM KCl ("in salt", solid line) for its (A) longest τ_1, (B) medium τ_2 and (C) shortest τ_3 decay times.

4.4 Summary

Steady-state fluorescence intensity quenching observed for 6MI-labeled oligonucleotides compared to the parent fluorophore (6MI monomer) suggest complex heterogeneous deactivation pathways involving static quenching mechanisms arising from local base interactions (ground-state base stacking and flipping) and environmental (solvent) interactions. On quadruplex folding, additional quenching (deactivation) of 6MI is observed. While there is evidence for enhanced static quenching (τ_3), the decay is predominated by QSSQ which represents an ultrafast (sub-picosecond) self quenching pathway that can not be resolved directly due to the resolution of the TCSPC measurements. Varying extents of QSSQ, reflected by the percentage of the dark component "A_{dark}", were observed for 6MI with different neighboring bases within the oligonucleotides. For either unfolded or folded states, the percentage of A_{dark} was highest for G5 and G11, which are sandwiched by two guanines, and lowest for G1 near the 5'-end. With addition of K^+ to the buffer, the percentage of A_{dark} increased to varying extents for all positions, suggesting an enhancement of base interactions around 6MI on folding, and/or enhancement of possible alternate sub-picosecond deactivation pathways (such as electron transfer). The extent of increase in A_{dark} values were more obvious for G4, G5, G9 and G11 than G1, which correlated with our observation in Chapter 3 that guanine 1 only weakly interacts with other bases in the quadruplex folding.

To better understand the origins for the lifetime heterogeneity of the 6MI-labeled sequences, we examined the decay-associated spectra for 6MI in varying sequences, which dissect the steady-state emission spectra to contributions from "species" with different decay times. On quadruplex folding for G1, the steady-state spectral red shift arises from the contributions of the specie with the longest decay time τ_1. For G4 and 6MI monomer, red shifted DAS were not observed.

Chapter 5

SINGLE VALUE DECOMPOSITION ANALYSIS – INDICATION OF INTERMEDIATE STATES

5.1 Introduction

The polymorphism of the G-quadruplex is highly dynamic in solution, and strongly depends on the cation present [66]. Therefore, it is not surprising that folding of the quadruplex forming sequence is complex and that multiple intermediate states may exist along the pathway. Fluorescence decay-associated spectra provide the opportunity to examine the local environmental heterogeneity experienced through the deactivation pathways for the fluorophore, as discussed in Chapter 4. In the following, we have applied single value decomposition (SVD) to analyze our quadruplex "melting" profiles, which has provided evidence for folding intermediates existing during the HT_4 quadruplex unfolding/folding pathway.

Thermal studies of the quadruplex measured using absorbance changes as discussed in Chapter 2, provided "global" melting profiles occurring at a single wavelength (295nm), which we analyzed using a simple two-state model to extract thermodynamic parameters (Tm and $\Delta G_{folding}$). This model assumes that during the folding process, only the folded and unfolded species exist, with no intermediate states present. While the two-state assumption provides a reasonable and convenient approach for analysis, it is clear that the conformational heterogeneity arising during G-quadruplex folding, needs further investigation.

Previously Gray *et al.* described the application of SVD for the multidimensional analysis of DNA melting curves, which includes possible extraction of intermediate states, with

no requirement of prior knowledge about the number of existing species underlying the DNA melting profiles [100]. In this chapter, SVD analysis has been adopted to examine if intermediate states coexist during quadruplex melting. This method of data analysis can supplement micro-heterogeneity studies examined using DAS analysis of fluorescence decay data.

5.2 Methods for SVD analysis

SVD analyses were applied to experimental data previously obtained from the UV absorbance melting studies in Chapter 2 and fluorescence melting studies in Chapter 3. To examine the existence of intermediate states using SVD, absorbance spectra over a wavelength range 220-340nm and at varying temperatures (typically 20-90°C) are required, as shown in Figure 5.1A. A data matrix **D** is then constructed from the absorbance values at varying wavelengths and temperatures as shown in Figure 5.1B. The size of the matrix is 61rows × 71columns, corresponding to absorbance values at 61 wavelength values (every 2nm in 220-340nm) and 71 temperature values (every 1°C 20-90°C), respectively. Thus, each column shows the absorbance spectrum at a single temperature, while each row shows the melting curve at a single wavelength.

Singular value decomposition (SVD) is a linear algebra method for factoring a data matrix. Using SVD, the matrix **D** can be factored into the product of three matrices, **U**, **S** and **V**:

$$D = USV^T \tag{5.1}$$

where V^T is the transpose of V [101]. The SVD analysis in our study was performed using MATLAB 7.7 (The MathWorks, Inc.), by importing the experimental matrix **D** to yield the **U**, **S** and **V** matrices. According to Gray *et al.*, the **S** matrix (size: 61×71) is a diagonal matrix and contains the singular values, the magnitudes of which are the weights of the components [100]. The **U** matrix (61×61) is a unitary matrix and contains the "basis spectra", which are "spectral shapes that can be combined to form the family of spectra" in the data matrix **D** [100]. The **V** matrix (71×71) is a unitary matrix containing the amplitude

vectors as a function of the experimental variable, which is temperature in these studies. The information in the **U**, **S** and **V** matrices is used to decide the number of significant species that compose the spectra in the parent matrix **D**. Therefore, if intermediates exist during the quadruplex melting, more than two (folded and unfolded) components are expected to be resolved using SVD analysis.

5.3 Results

5.3.1 Analysis of the HT_4 G-quadruplex absorbance melting

The global melting profiles, as monitored using absorbance spectral changes, for the **unlabeled** HT_4 G-quadruplex in 100mM NaCl or KCl were examined using SVD analyses. The conformations of the two quadruplexes are expected to be significantly different when in the presence of Na^+ or K^+-ions (basket *versus* hybrid, respectively), which may lead to varying unfolding pathways. The most important step in SVD analysis is to determine the number of statistically significant components. Several criteria, to justify the number of significant components, were used and discussed as follows. First, the magnitudes of the singular values **S** were inspected. Since **S** measures the weight of each component, for random or insignificant components, their **S** values should fade out into noise. As shown in Figure 5.2A, the S values are obvious for the first seven components *versus* other higher-numbered components.

The second justification is the value of the first-order autocorrelation coefficient for columns in the **U** and **V** matrices. The autocorrelation coefficient is calculated from

$$C(X_i) = \sum_j (X_{j,i})(X_{j+1,i}) \tag{5.2}$$

where $X_{j,i}$ and $X_{j+1,i}$ are the absorbance values at the j^{th} and $j+1^{th}$ row of column i from either the **U** or **V** matrix. The value of $C(X_i)$ is a measure of the smoothness between the adjacent row elements and varies between 1 and -1. Values near -1 indicate rapid row to row variations, or "noise". On the other hand, the $C(X_i)$ values for significant singular

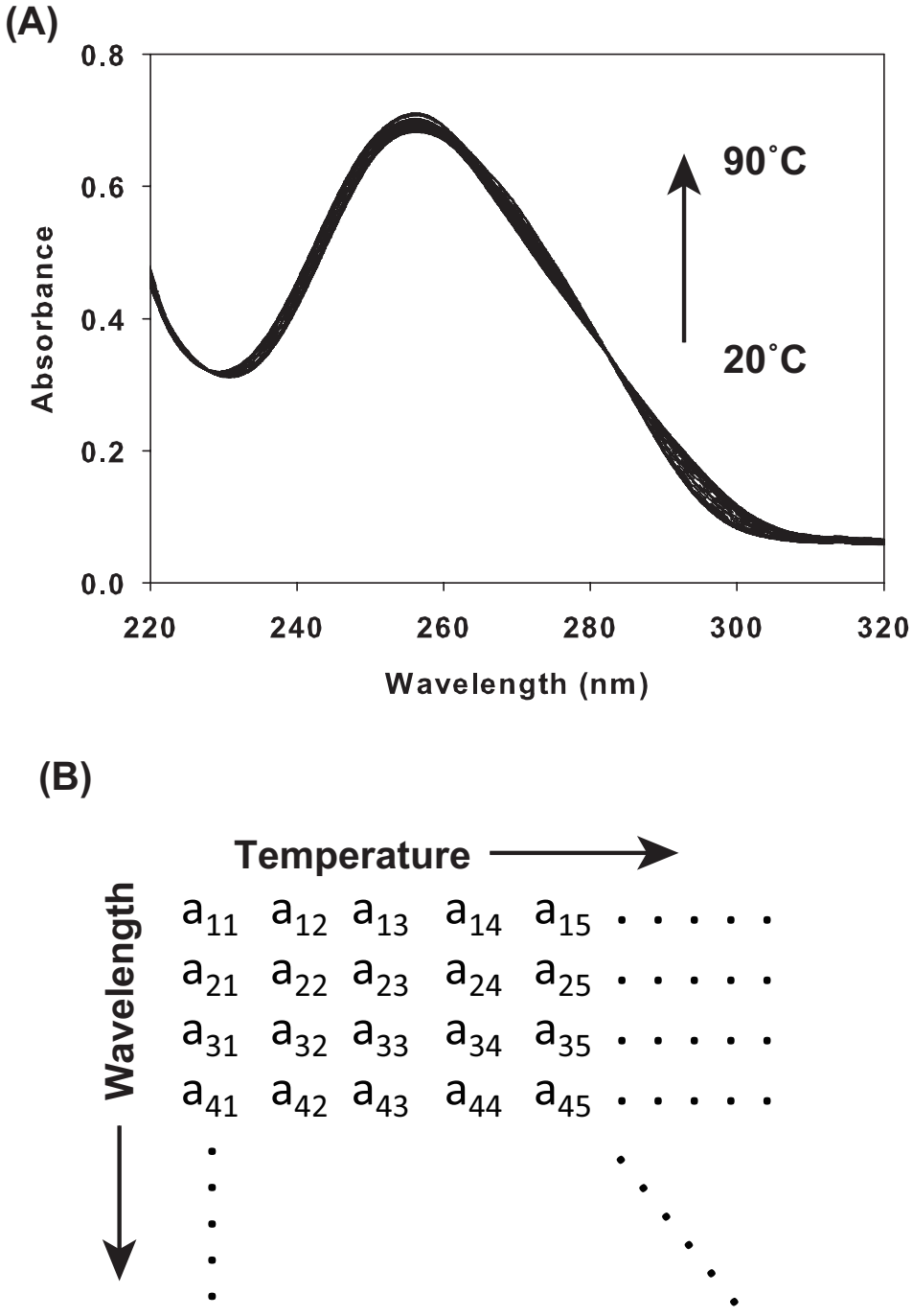

Figure 5.1. Example of the data matrix D from absorbance melting study. (A) UV spectra of the HT_4 oligonucleotide at varying temperatures. The absorbance spectra were scanned from 220 to 340 at 2nm increments. The temperature of the sample was increased from 20 to 90°C with 1°C increment. (B) The data matrix D was constructed from (A), and contained absorbance values of the oligonucleotide at varying wavelengths and temperatures.

components should be close to 1. Henry and Hofrichter have proposed that when the $C(X_i)$ value drops to 0.8, the experimental signal-to-noise ratio is around 1 [101]. Thus, a $C(X_i)$ value larger than 0.8 was used as the criteria for counting significant components or unfolded intermediates. The autocorrelation coefficient for the U and V matrices for the first 10 components are shown in Figure 5.2B. There are six components in the U matrix, and five components in the V matrix with autocorrelation coefficients larger than 0.8.

The final criteria examined is the randomness of the residual plot produced from the difference matrix **A**. The difference matrix **A** is defined as the difference between the experimental matrix **D** and the computed data matrix with a truncated number of singular values S'_n:

$$A = D - US'_nV^T \tag{5.3}$$

where S'_n is a matrix created to contain first n components only, and set to zero everywhere else. When the correct number (n) of singular values is used in S', the matrix A should contain only random noise, and further calculations using $n+1$ will not improve the randomness of the residuals.

Figure 5.3 shows a typical contour plots for the A matrices with the number (n) of components ranging from two to seven used for calculation for HT_4 unlabeled G-quadruplex in 100mM NaCl (basket conformation). With values of n equal to 2 or 3 used for the computations (Figures 5.3A and B), the contour plots are non-random, suggesting the number of significant components are greater than 3. Randomness slightly increases from Figure 5.3D (n = 5) to E (n = 6), but does not improve from Figure E to F. Hence, the number of significant components may be as many as five, but are definitely more than two, indicating the existence of folding intermediates in the Na^+-stabilized quadruplex thermal melting pathway.

5.3.2 Basis spectra and temperature-dependence of singular components

The three steps described above, used to determine the number of significant components suggest that more than two components do exist in the thermal melting profile for

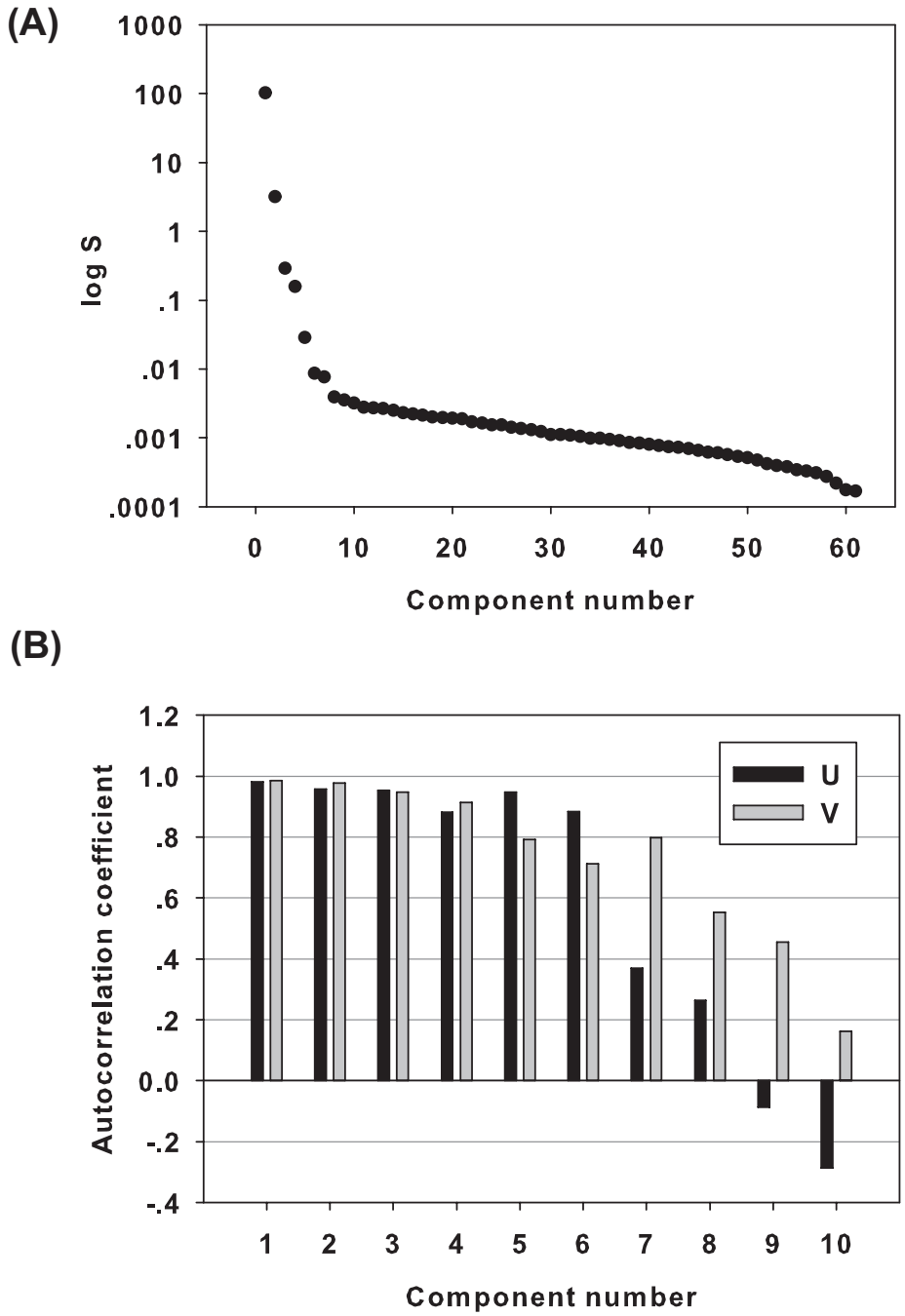

Figure 5.2. The singular values and the autocorrelation coefficient values from the SVD analysis of HT_4 G-quadruplex absorbance melting in 10mM cacodylate (pH 7.2) with 100mM NaCl. (A) The singular values for the 61 components resolved from the SVD analysis is presented in log scale. Only the first five components have statistically significant values, while values for the other components fade into noise. (B) The autocorrelation coefficients $C(X_i)$ for the first ten components in the **U** and **V** matrices are shown. When the $C(X_i)$ value of a component is larger than 0.8, the component can be counted as significant. $C(X_i)$ were calculated from $C(X_i) = \sum(X_{j,i}(X_{j+1,i})$, where $X_{j,i}$ and $X_{j+1,i}$ are the absorbance values at the j^{th} and $j+1^{th}$ row of column i from either the **U** or **V** matrix.

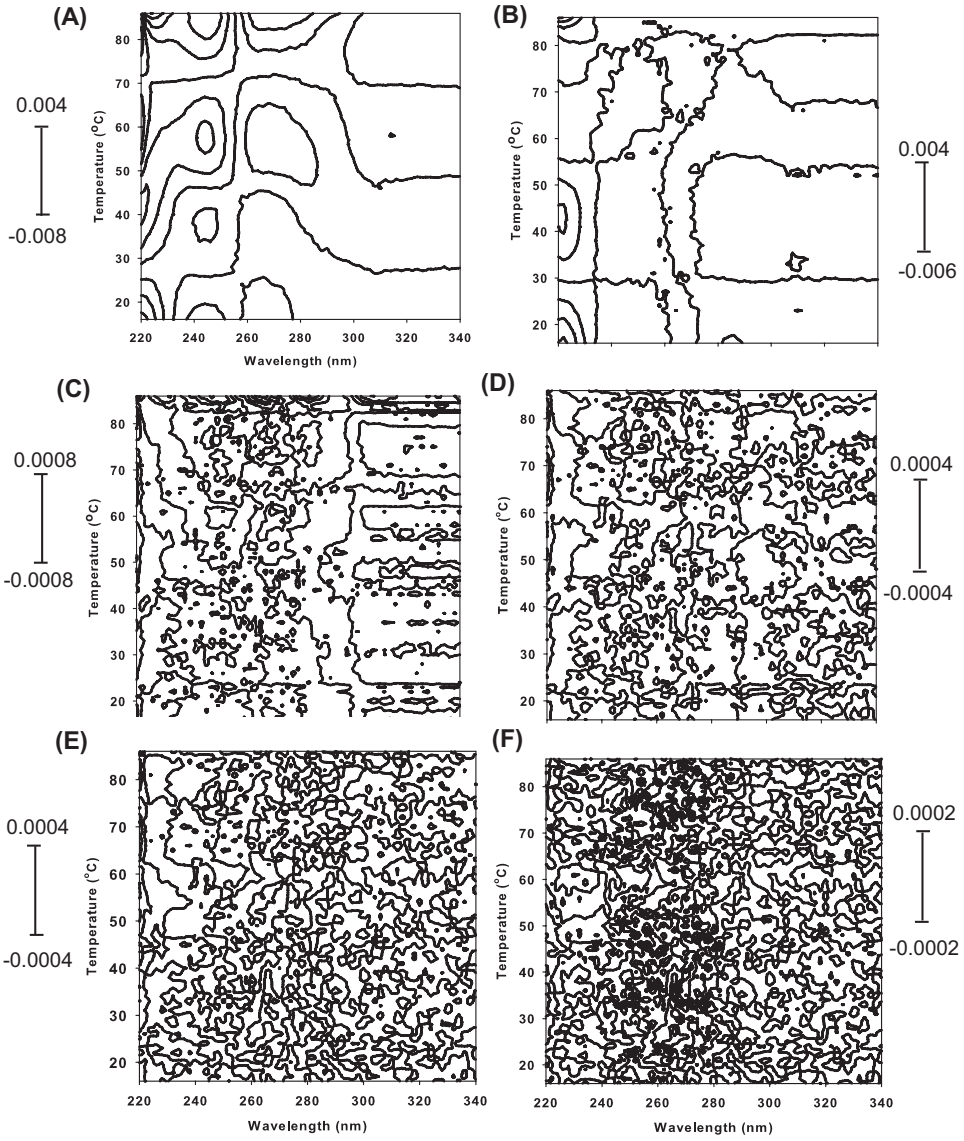

Figure 5.3. Contour plots for the **A** matrices—the differences between the experimental data matrix and data matrices computed with limited number of singular values. Data for the HT_4 G-quadruplex UV-absorbance detected melting profiles in 100mM NaCl are shown. The residual plots show the view looking along the A axis. Numerical ranges for A are shown on the scales next to each plot. The number of singular values n used to compute the **A** matrices were: (A) 2; (B) 3; (C) 4; (D) 5; (E) 6; (F) 7;

HT_4 G-quadruplex in 100mM NaCl, as derived from the absorbance spectra.

We can now plot the basis spectra ($U \times S$ matrix elements) and the V matrices of the first six singular components, for both the parent HT_4 in 100mM KCl (Figure 5.4 and 5.6) and 100mM NaCl (Figure 5.5 and 5.7) buffer. It is important to note that the singular components generated by the SVD analysis do not represent the real molecular species existing along the thermal folding of the quadruplex [101]. Therefore, the SVD analysis does not generate the absolute spectra of the real species present in the DNA solution, but rather shows the mathematical spectra—the basis spectra which can be combined to reproduce the experimental spectrum shown in Figure 5.1A.

The basis spectrum of component 1 resembles a typical/average experimental absorbance spectrum for a DNA oligonucleotide, while the spectrum of component 2 resembles the TDS spectra of the HT_4 G-quadruplex in 100mM KCl (Figure 5.4A) or in 100mM NaCl (5.5A). The magnitudes of the third and forth basis spectra in Figure 5.4B and 5.5B are smaller but still smooth and significant, while the fifth and sixth spectra appears noisy and almost flat. Therefore, the experimental absorbance spectra of the parent HT_4 G-quadruplex in the presence of Na^+ or K^+ can be decomposed into the contributions of four components, suggesting the unfolding pathway of the G-quadruplex is $F \rightarrow I_1 \rightarrow I_2 \rightarrow U$, where F, I_1, I_2 and U represent the folded, intermediate 1, intermediate 2 and unfolded states of the quadruplex, respectively.

The temperature-dependent V matrix elements show the relative weights of each spectral component to the overall absorbance at a particular temperature [100]. For HT_4 in 100mM KCl shown in Figure 5.6A, the first two components 1 and 2 show their mid-point at 61°C, close to the expected Tm value reported in Chapter 2. The V curve shapes for components 3 and 4 are non-random, but for component 5 and 6 were noisy and random (Figure 5.7B). Similarly for HT_4 in 100mM NaCl in Figure 5.7, the V matrices of components 1 and 2 resemble melting curves with a mid-point transition temperature around 50°C, expected for the Na^+-stabilized form of the quadruplex. Here again, inspection to the temperature-dependence V matrix elements also suggests the existence of four significant components in

the global thermal melting for the parent HT_4 G-quadruplex.

Overall, from the above inspections of the singular values **S**, the basis spectra $\mathbf{U} \times \mathbf{S}$ and the temperature-dependent **V** matrices, at least four spectral components are needed to construct the experimental data matrix **D**, suggesting that conformational intermediate states and heterogeneity exist along with the G-quadruplex melting (with pathway $F \rightarrow I_1 \rightarrow I_2 \rightarrow U$), which underly the measured UV-absorbance spectra.

We have also performed SVD analysis on the UV-absorbance melting profiles of the 6MI-labeled sequences in 100mM KCl or NaCl as presented and discussed in Chapter 2. The resolved singular values S from the absorbance melting studies in 100mM KCl or NaCl are shown Figure 5.8. The numbers of the significant components determined by each criterion are summarized in Table 5.8. The numbers of components determined by each criterion may vary, but all give values greater than three, suggesting that intermediate folding state(s) do exist during folding. Overall, at least four components exist during the thermal melting of the G-quadruplex formed by each labeled oligonucleotide, suggesting that unfolding pathways for labeled quadruplex sequences may proceed *via* pathways similar to their parent (unlabeled) sequences.

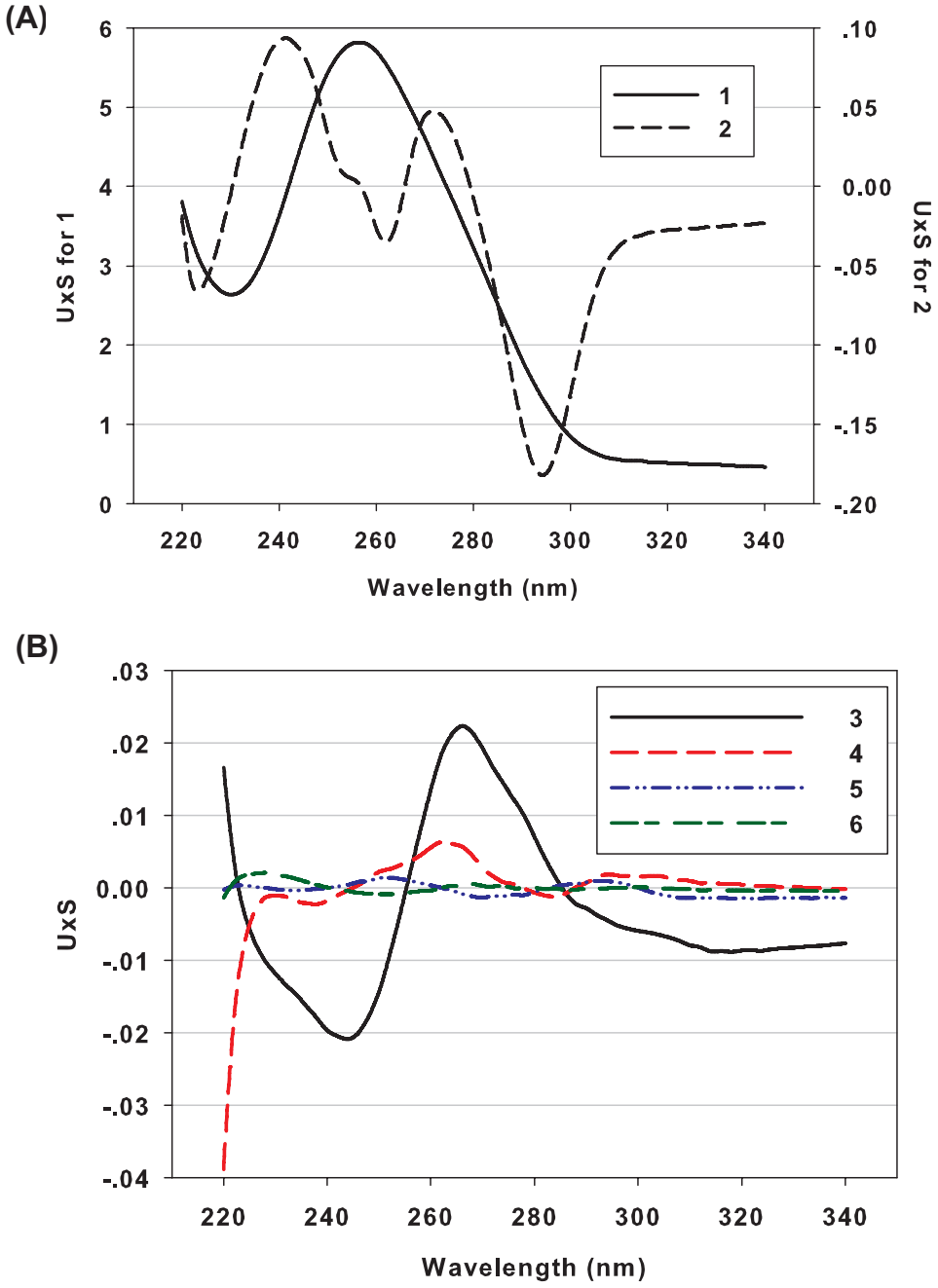

Figure 5.4. The basis spectra plotted by the $U \times S$ from the SVD analysis of the HT_4 G-quadruplex absorbance melting in 100mM KCl. (A) The US values as a function of temperature for component 1 and 2 show a typical experimental HT_4 oligonucleotide absorbance and thermal difference spectra for the G-quadruplex, respectively. (B) The U×S spectra for components 3 and 4 are non-random, indicating the existence of other conformational states. However, for components 5 and 6, their U×S spectra fade into noise, suggesting these components are not significant.

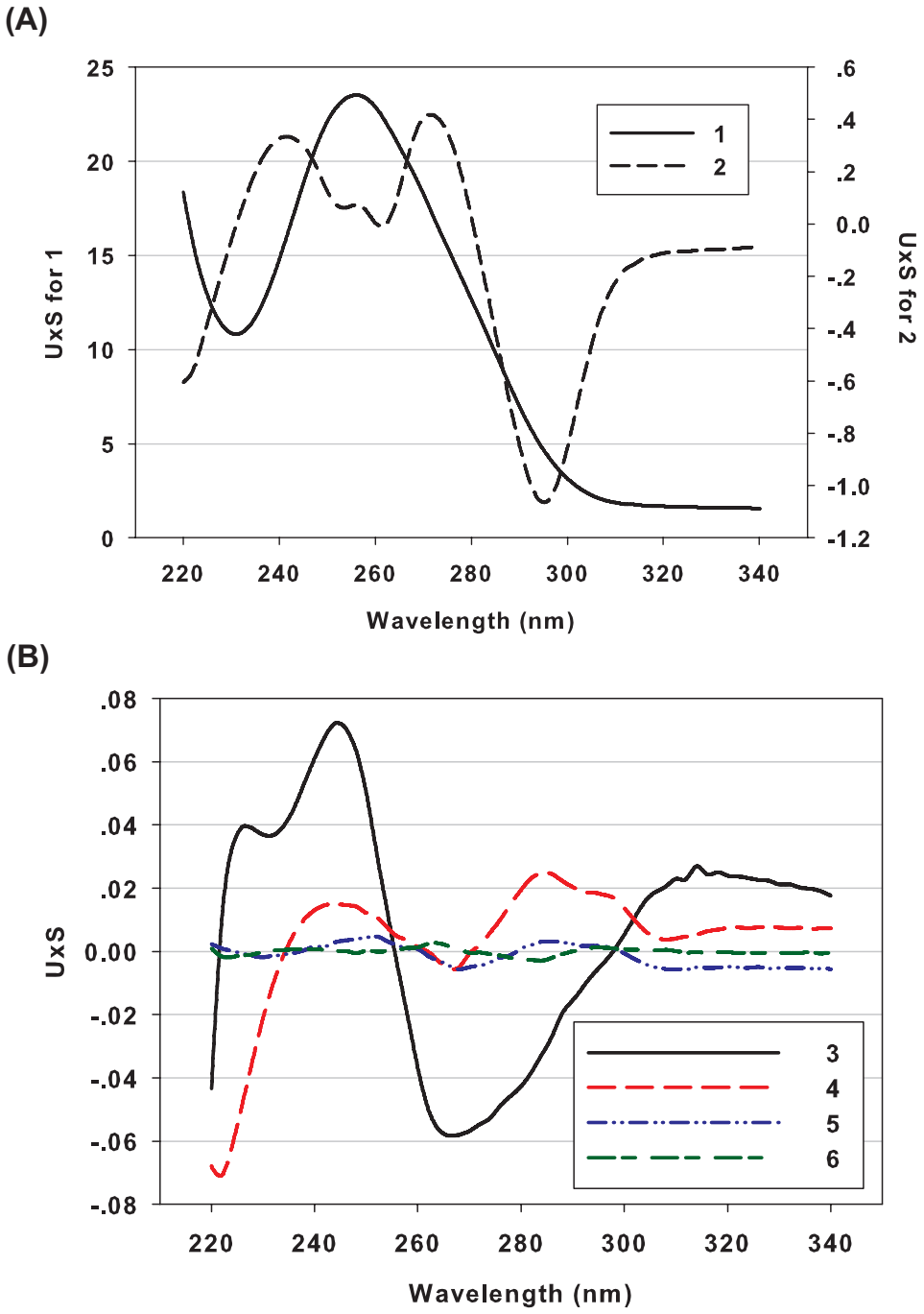

Figure 5.5. The basis spectra plotted by the $U \times S$ from the SVD analysis of the HT_4 G-quadruplex absorbance melting in 100mM NaCl. The numbers for each plot correspond to the component number in Figure 5.2A. (A) The US values as a function of wavelength for component 1 and 2 show a typical experimental HT_4 oligonucleotide absorbance and thermal difference spectra for the G-quadruplex, respectively. (B) The U×S spectra for components 3 and 4 are non-random, indicating the existence of other conformational states in the G-quadruplex melting process. However, for components 5 and 6, their U×S spectra fade into noise, suggesting these components are not significant.

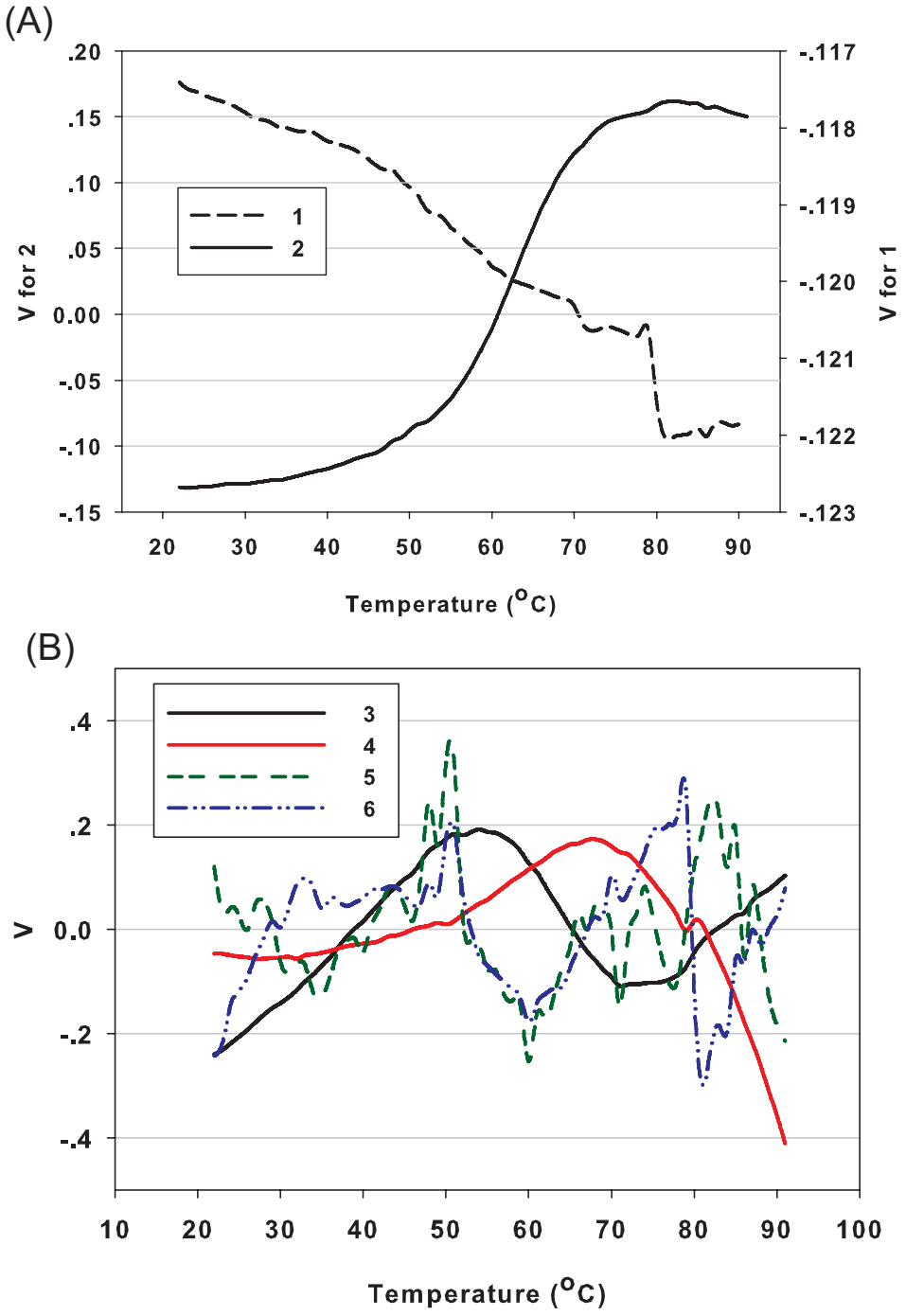

Figure 5.6. The V matrices elements as a function of temperature for the first six components in the HT_4 G-quadruplex absorbance melting in 100mM KCl. (A) The V values as a function of temperature for components 1 and 2 are similar to the absorbance melting profiles shown in Chapter 2. (B) The V spectra for components 3 and 4 are non-random, indicating the existence of other intermediate conformational states. However, for components 5 and 6, their V spectra are random and shows no dependence on temperature, suggesting these components are not significant.

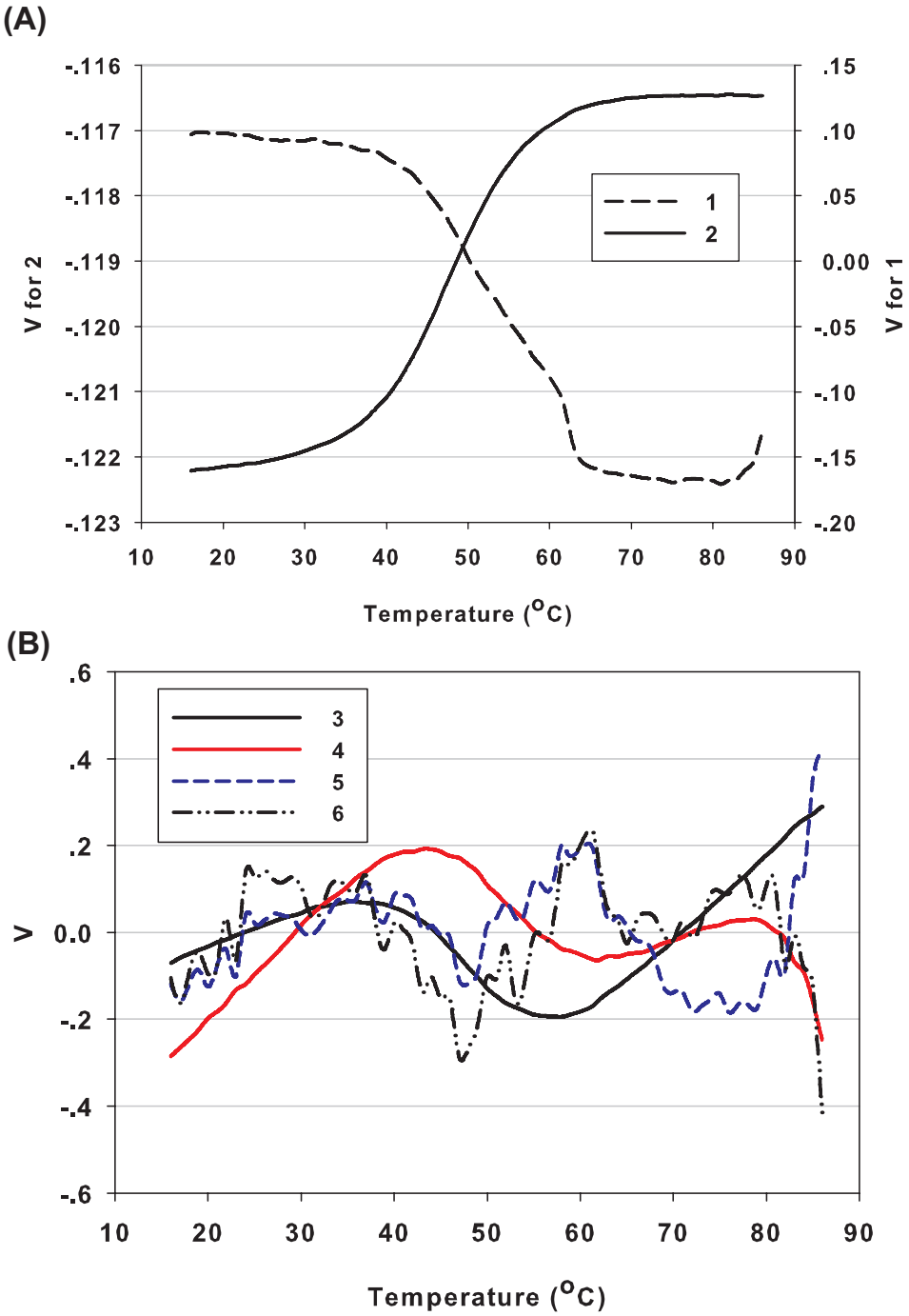

Figure 5.7. The V matrices elements as a function of temperature for the first six components in the HT_4 G-quadruplex absorbance melting in 100mM NaCl. (A) The V values as a function of temperature for components 1 and 2 are similar to the absorbance melting profiles shown in Chapter 2. (B) The V spectra for components 3 and 4 are non-random, indicating the existence of other conformational intermediate states. However, for components 5 and 6, their V spectra are random and shows no dependence on temperature, suggesting these components are not significant.

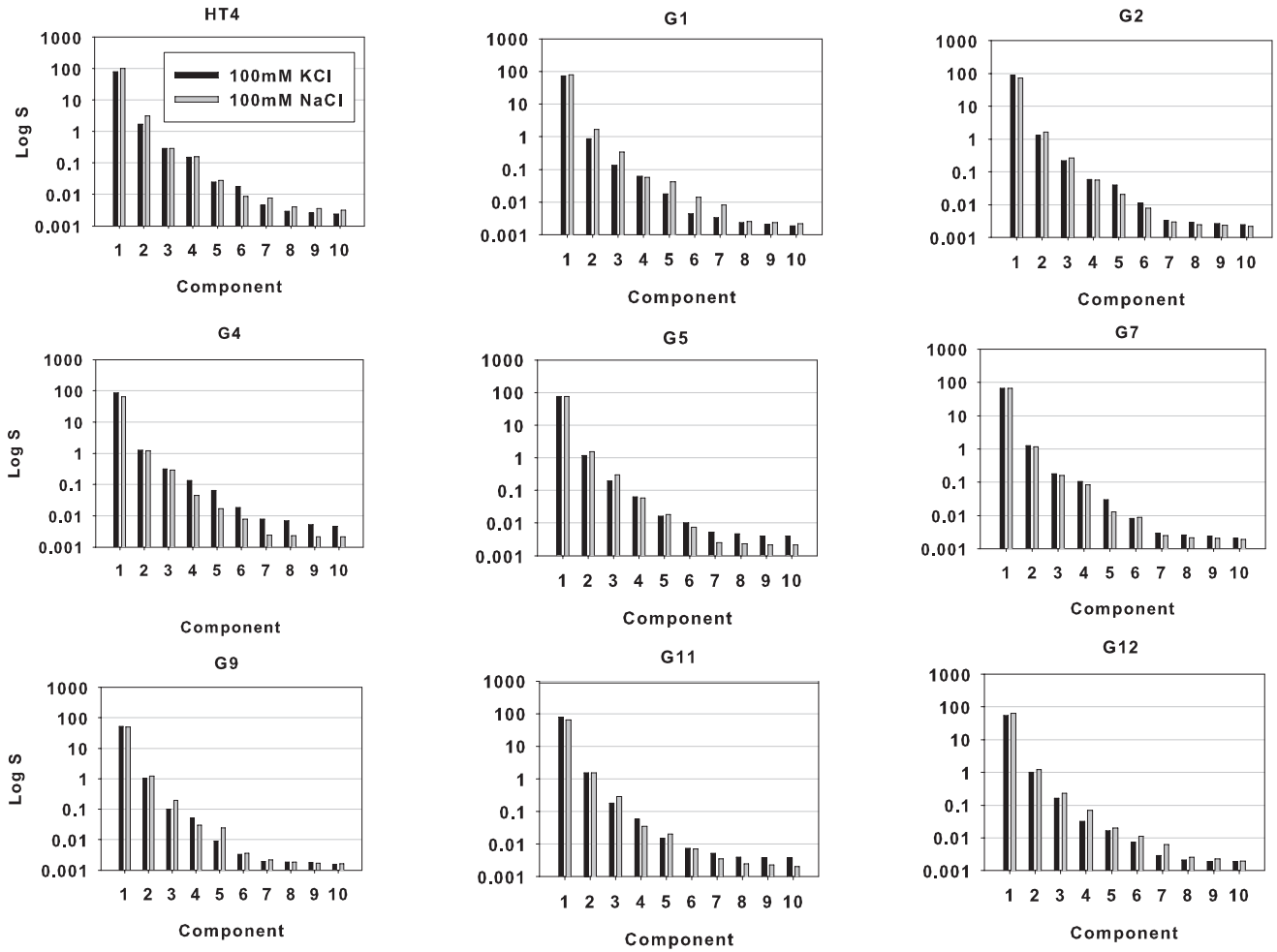

Figure 5.8. The singular (S) values resolved from the SVD analysis for the absorbance melting data of parent HT_4 and eight 6MI-labeled oligonucleotides. The S values are presented in log scale. Data for the UV-absorbance melting studies from Chapter 2 were used for the SVD analysis. The buffer conditions for the oligonucleotides are 10mM cacodylate (pH 7.2) with 100mM KCl (black bar) or 100mM NaCl (grey bar).

Table 5.1. Numbers of significant components resolved from the SVD analysis for the **absorbance** melting data for the parent G-quadruplex and substituted HT_4 sequences in the presence of 100mM KCl or NaCl

Sequence	In 100mM KCl[a]				In 100mM NaCl [a]			
	S	US	V	contour	S	US	V	contour
HT_4	6	5	4	4	5	5	4	4
G1	5	5	4	4	7	5	4	6
G2	6	5	4	5	6	4	4	4
G4	6	5	5	5	6	4	5	5
G5	6	4	4	4	6	4	4	4
G7	6	5	4	5	6	5	4	5
G9	5	4	4	4	5	5	4	5
G11	5	4	4	4	6	5	4	5
G12	6	4	4	4	7	5	4	5

Note: Buffer conditions were 10mM cacodylate (pH 7.2) with 100mM KCl or 100mM NaCl. The data for SVD analysis were from the absorbance melting studies in Chapter 2. The numbers of significant components were determined from the log plot of singular values, ("S" shown in Table 5.8), the smoothness of the "US" spectra (e.g. Figures 5.4 and 5.5) and "V" melting profiles (e.g. Figures 5.6 and 5.7), and the randomness of the contour plots (e.g. Figure 5.3).

5.3.3 SVD analysis in fluorescence melting studies

As discussed in Chapter 3, fluorescence-based thermal folding studies of the 6MI-labeled quadruplex-forming sequences focus on the local environmental effects (base stacking interactions and solvent effects) around a single guanine base position. Therefore, fewer conformational states may exist from SVD analysis of fluorescence melting profiles, in contrast to the global absorbance melting studies. Alternatively, different fluorophore positions along the quadruplex may mirror sensitivity to global conformational folding/unfolding effects.

Substitution of guanine by 6MI at G5 locates the fluorophore in the middle tetrad of the quadruplex, with strong local neighboring interactions resulting in fluorescence intensity quenching during the quadruplex folding process, as discussed in Chapter 3. We have used the fluorescence thermal annealing data of G5 in 100mM KCl as the example for discussion. As shown in Figure 5.9A, at least three (possibly four) significant components may be extracted from the fluorescence melting data (Figure 5.2A).

From the autocorrelation coefficients of the **U** and **V** matrices in Figure 5.9B, there are also three components with autocorrelation coefficients values greater than 0.8. Further confirmation is also seen in the contour plots in Figure 5.10, as no obvious enhancement is observed when four components were used for the computation of the contour plots. The shapes of the basis spectra $U \times S$ and the V matrix shown in Figures 5.11 and 5.12 also suggest the presence of three significant intermediates. The mid-point temperatures for the V value transitions for components 1 and 2, as shown in Figure 5.12 were around 52 °C, close to the $T_{1/2}$ reported in the G5 fluorescence melting in Chapter 3. Similar SVD analysis results were observed for all other 6MI-labeled oligonucleotides and summarized in Figure 5.13 and Table 5.2. In general, the number of significant components that could be resolved from the fluorescence folding profiles appeared less than those resolved from the corresponding UV-absorbance melting data. This might be expected since the fluorescence measurement focuses solely on the effects of the environment surrounding a single 6MI probe located at a specific guanine position during folding. In general three components were resolved from the fluorescence phase transition data for each 6MI-substituted oligonucleotide both in 100mM

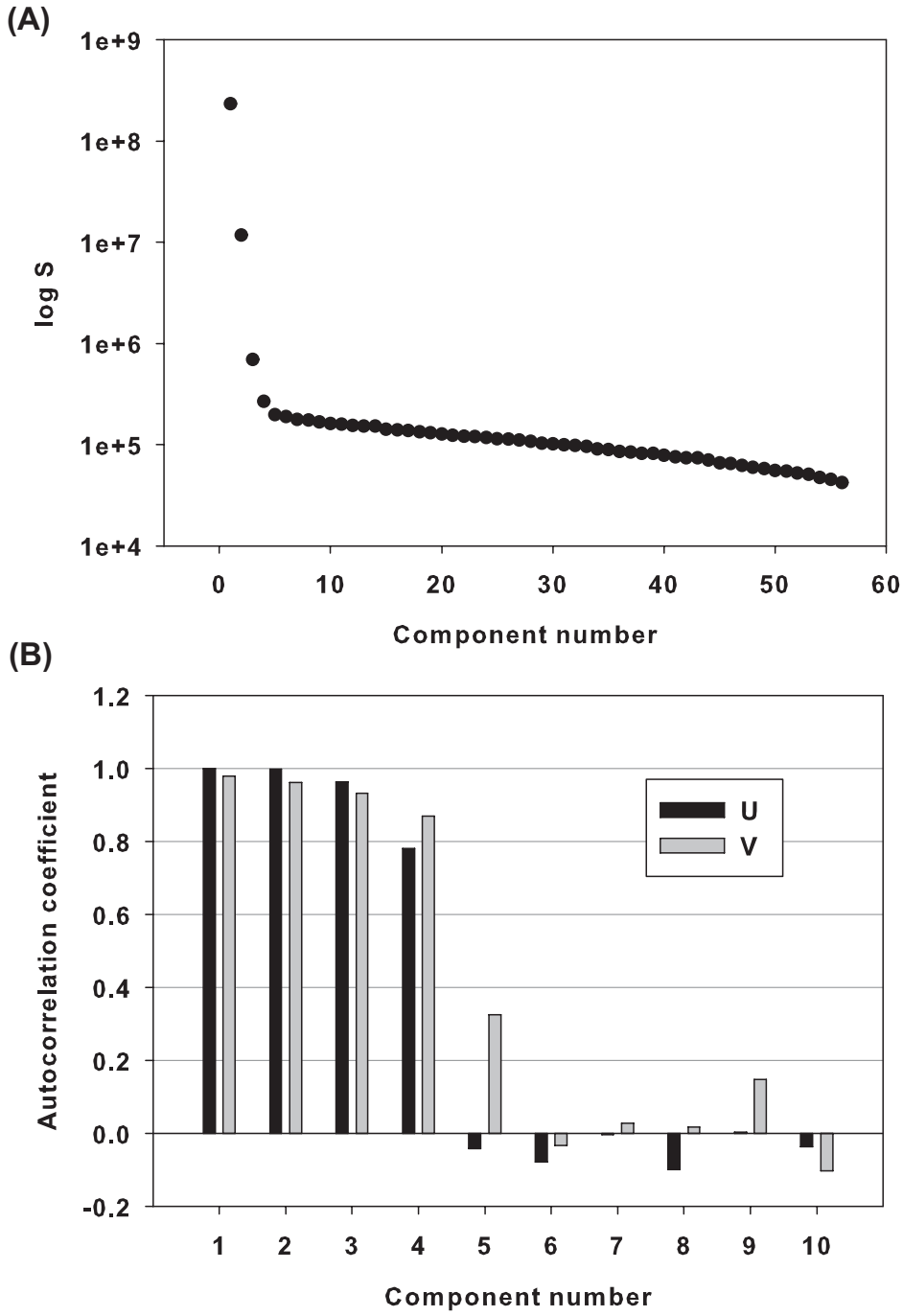

Figure 5.9. The singular values and the autocorrelation coefficient values from the SVD analysis of G5 fluorescence melting in 100mM KCl. (A) The singular values S is presented in log scale. The values of the first three components is of statistically significance, while any other values fade into noise. (B) The autocorrelation coefficient $C(X_i)$ for the first ten components in the U and V matrices are shown. When the $C(X_i)$ value of a component is larger than 0.8, the component can be counted as significant. $C(X_i)$ were calculated from $C(X_i) = \sum(X_{j,i}(X_{j+1,i})$, where $X_{j,i}$ and $X_{j+1,i}$ are the absorbance values at the j^{th} and $j + 1^{th}$ row of column i from either the **U** or **V** matrix.

KCl or NaCl.

5.4 Summary

SVD analysis of quadruplex "melting" data examines the numbers of significant singular components present, and provides insight into whether intermediates exist along the G-quadruplex folding/unfolding pathway. From the inspections of the singular values **S**, the autocorrelation coefficients for the **U** and **V** matrices, the basis spectra of $\mathbf{U} \times \mathbf{S}$ and the melting profiles of **V**, more than two significant singular components (folded and unfolded states) are indicated by absorbance melting profiles of the HT_4 sequence, or fluorescence melting profiles of the 6MI-labeled sequences. Therefore, folding intermediates do exist in the quadruplex melting pathway, from the perspective of either the whole G-quadruplex, or the single local guanine residues substituted by 6MI. However, only three components may be decomposed from the fluorescence melting data, indicating that while intermediate states are involved in the thermal folding transition arising from local effects surrounding 6MI, global folding from UV studies may involve the overall backbone rearrangement after orientation of the bases.

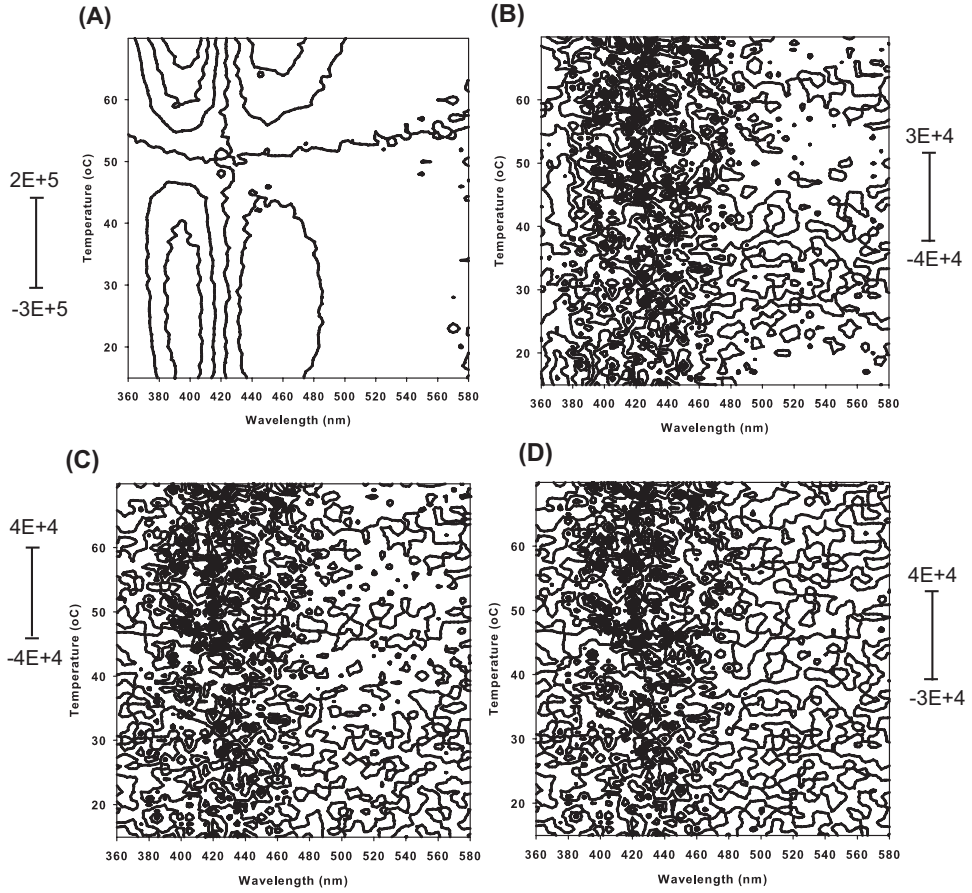

Figure 5.10. Contour plots of the A matrices – the differences between the experimental data matrix and data matrices computed with limited number of singular values, for the G5 fluorescence melting in 100mM KCl are shown. Numeric range of A values across each plot are shown on the scale. Experimental data was from the fluorescence melting studies in Chapter 3. Fluorescence emission spectra of G5 at varying temperatures in 10mM cacodylate (pH 7.2) with 100mM KCl were scanned from 340-560nm with excitation at 340nm. Incubation temperatures were increased from 20°C to 80°C with 1°C increment. Excitation and emission slits were 8nm and 4nm, respectively. The data matrix was then constructed from the fluorescence emission intensities at varying wavelengths and temperatures and SVD analyzed. The number of singular values used to compute the **A** matrices were: (A) 1; (B) 2; (C) 3; (D) 4.

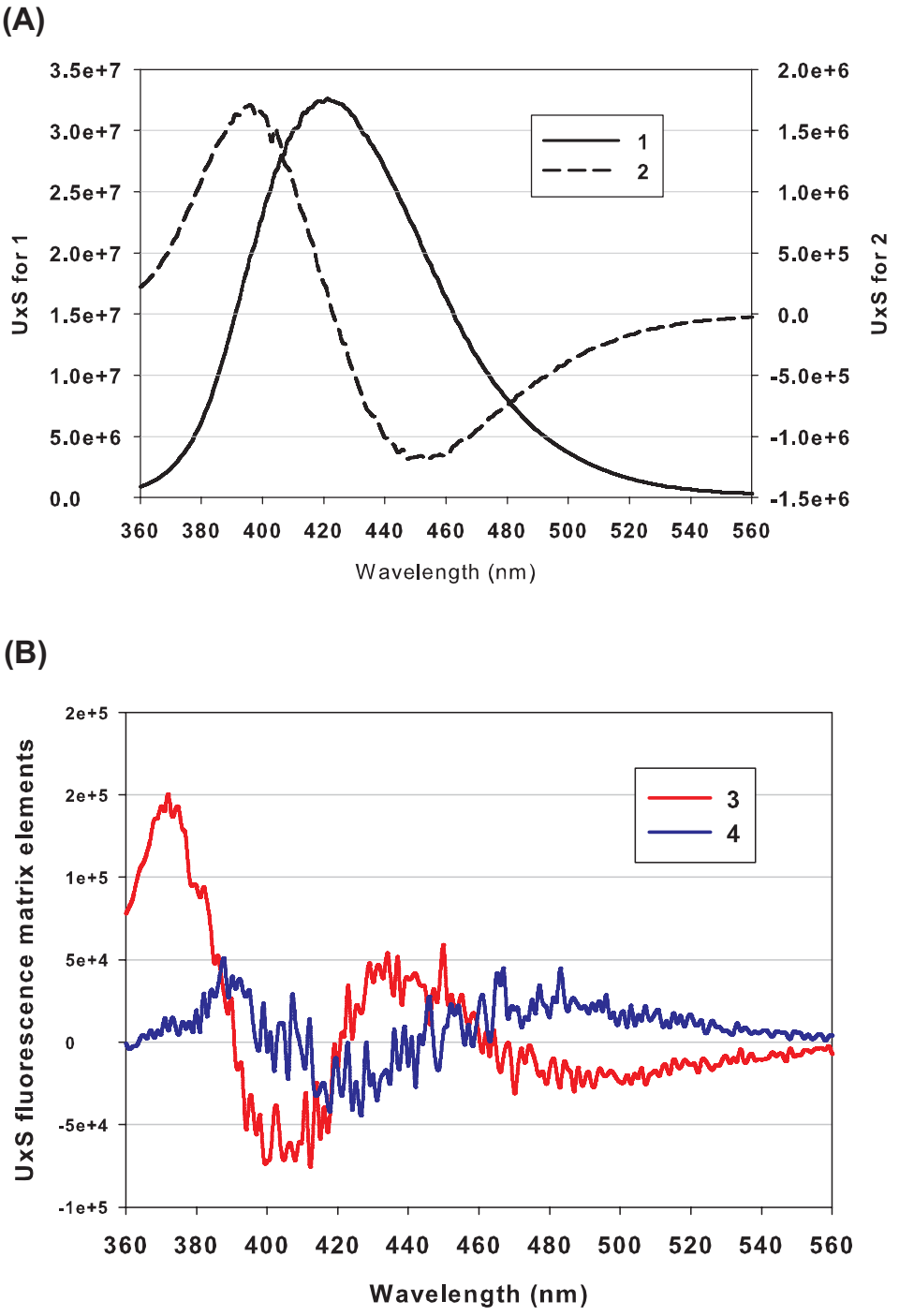

Figure 5.11. The basis spectra plotted by the $U \times S$ as a function of emission wavelengths for the first four components, from the SVD analysis of the G5 fluorescence melting in 100mM KCl. Experimental data and conditions were identical to that stated in Figure 5.10.

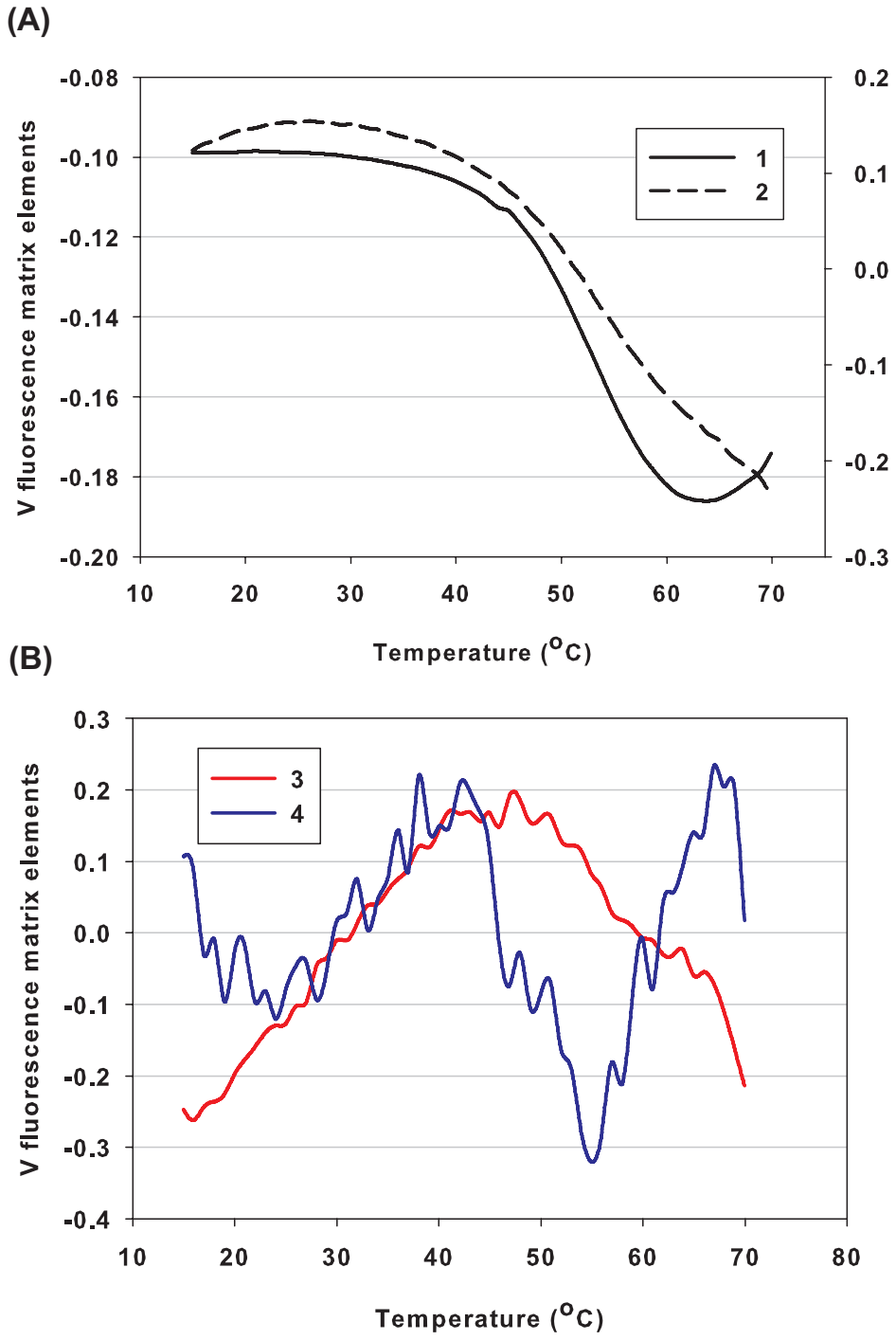

Figure 5.12. The V matrices elements as a function of temperature for the four most significant components in the G5 fluorescence melting in 100mM KCl. Experimental data and conditions were identical to Figure 5.10. (A) The mid-point temperature for component 1 and 2 was around 52°C, close to the $T_{1/2}$ value reported from the fluorescence melting studies in Chapter 3. (B) The V matrix value for component 3 shows moderate dependence on temperature, but for component 4 shows little dependence and appears random.

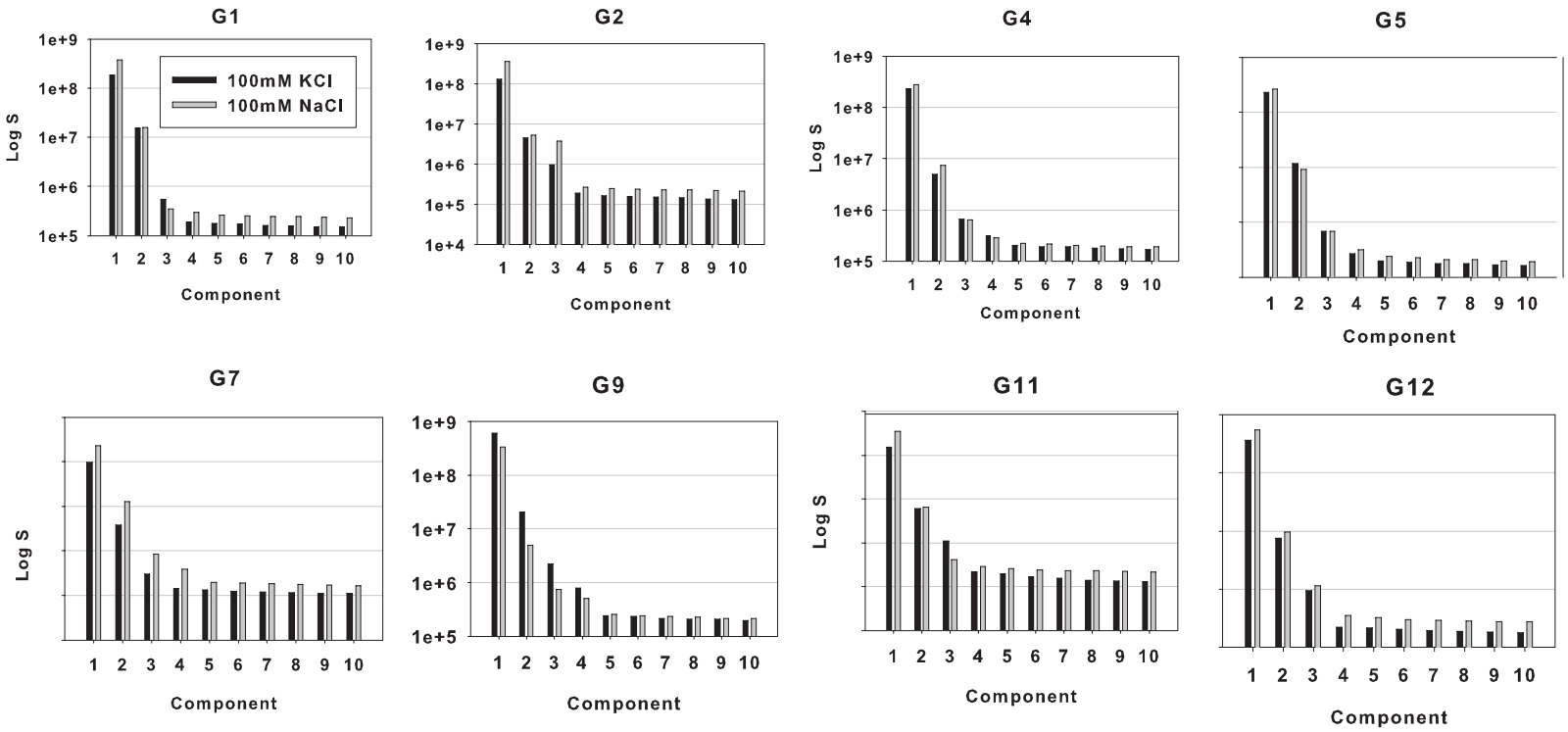

Figure 5.13. The singular (S) values resolved from the SVD analysis from the fluorescence melting profiles for eight 6MI-labeled oligonucleotides. The S values are presented in log scale. Data for the fluorescence melting studies from Chapter 3 is used for the SVD analysis. The buffer conditions for the oligonucleotides are 10mM cacodylate (pH 7.2) with 100mM KCl (black bar) or 100mM NaCl (grey bar).

Table 5.2. Numbers of significant components resolved from the SVD analysis for the **fluorescence** melting data for G-quadruplexes formed from 6MI-substituted human telomeric sequences in the presence of 100mM KCl or NaCl

Sequence	In 100mM KCl[a]				In 100mM NaCl [a]			
	S	US	V	contour	S	US	V	contour
G1	3	3	3	3	2	3	2	3
G2	3	3	3	3	3	3	3	3
G4	4	3	4	4	3	3	3	3
G5	3	3	3	3	3	3	3	3
G7	3	3	3	3	3	3	3	3
G9	4	4	4	4	4	3	3	4
G11	3	3	3	3	3	3	3	4
G12	3	3	3	3	3	3	3	3

Note: The 6MI-substituted oligonucleotides were in buffer of 10mM cacodylate (pH 7.2) with 100mM KCl or 100mM NaCl. The data for SVD analysis were from the fluorescence melting studies in Chapter 3. The numbers of significant components were determined from the singular values, ("S" shown in Table 5.13), the smoothness of the "US" spectra (e.g. Figure 5.11) and "V" melting profiles (e.g. Figures 5.12), and the randomness of the contour plots (e.g. Figure 5.10).

Chapter 6

CONCLUSIONS AND DISCUSSION

Previous investigations of quadruplex structures have suggested more complex and polymorphic conformations in solution *in vitro* [61–66], rather than the Na^+-promoted basket or the K^+-promoted hybrid-1, hybrid-2 and propeller structures determined from NMR or X-ray crystallography. Given that the quadruplex structure can inhibit the activity of the telomerase enzyme in cancer cells, if we are to design appropriate "drug", or small molecules (QIAs) that can promote quadruplex formation, understanding the solution conformation of the quadruplex is an important challenge. In particular there is lack of understanding about folding dynamics of G-quadruplex, and how each guanine residue within the single-stranded sequence contributes to the formation and stabilization of the G-quadruplex.

Our studies have focused on the solution conformation of the human telomeric HT_4 intramolecular G-quadruplex, and specifically the contribution of individual guanine residues to the overall conformational stability in the presence of K^+ and Na^+-ions. With 12 guanines present in the single stranded HT_4 sequence, details identifying the critical guanine residues required for G-quadruplex formation and stabilization remain unclear. We hypothesized that each guanine in the HT_4 sequence plays a differing role in conformational stability and folding dynamics of the G-quadruplex.

Through site-specific substitution of the individual guanine residues with the fluorophore 6MI (with eight 6MI-labeled sequences: G1, G2, G4, G5, G7, G9, G11 and G12), we have investigated the contributions of individual guanine sites to the global quadruplex stability (from thermodynamic analyses), and the influence of local environmental effects (from

steady-state and time-dependent fluorescence studies) about each base position.

Most importantly, using TDS we have shown that the G-quadruplex conformation can be folded in presence of 100mM KCl or NaCl by all 6MI-substituted oligonucleotides. Surprisingly, the folded quadruplex conformations for sequences G1 or G7 in the presence of Na^+, give rise to a TDS very similar to those stabilized in K^+. Guanine substitutions at positions G1 and G7 appear to impact the quadruplex stability least in the global or local thermal studies. In the native Na^+-stabilized basket quadruplex conformation (Figure 6.1C), guanine 7 is located next to the diagonal loop across the top tetrad. It is possible that 6MI, at these two positions in the presence of Na^+-ion, induces a conformation switch from the basket to the hybrid-like conformation (or some intermediate conformations), by alternating the second TTA loop from the diagonal to the lateral topology, resulting in a better conformational stability over other substitutions.

Global stability studies (Tm and $\Delta G_{folding}$) of the quadruplex formed by each 6MI-labeled oligonucleotide revealed Tm values lower than observed for the parent HT_4 conformation, suggesting that 6MI substitution or "mutation" at any guanine location reduces the conformational stability of the quadruplex. However, the extents to which Tm and $\Delta G_{folding}$ values decrease vary for each 6MI-labeled oligonucleotide, support our hypothesis that different guanine positions of the quadruplex play distinct roles in the formation and stabilization of G-quadruplex. Interestingly, stability of the substituted Na^+-quadruplex at physiological temperatures (37°C) was significantly compromised. Hence, under a normal cellular condition where the $[K^+] >> [Na^+]$, the predominant quadruplex conformation is expected to be the K^+-hybrid quadruplex conformation, unless binding of an appropriate QIA ligand can promote the Na^+-stabilized basket conformation. While the biological relevance or importance of the varying quadruplex conformations *in vivo* remains unknown, drugs that bind to the Na^+-conformation may be relevant for productive cancer therapies, since elevated levels of Na^+ have been reported in some cancer cells [102, 103]

We have exploited the fluorescence sensitivity of 6MI as a probe of local environmental changes around individual guanine position. Upon decreasing temperature or addition of

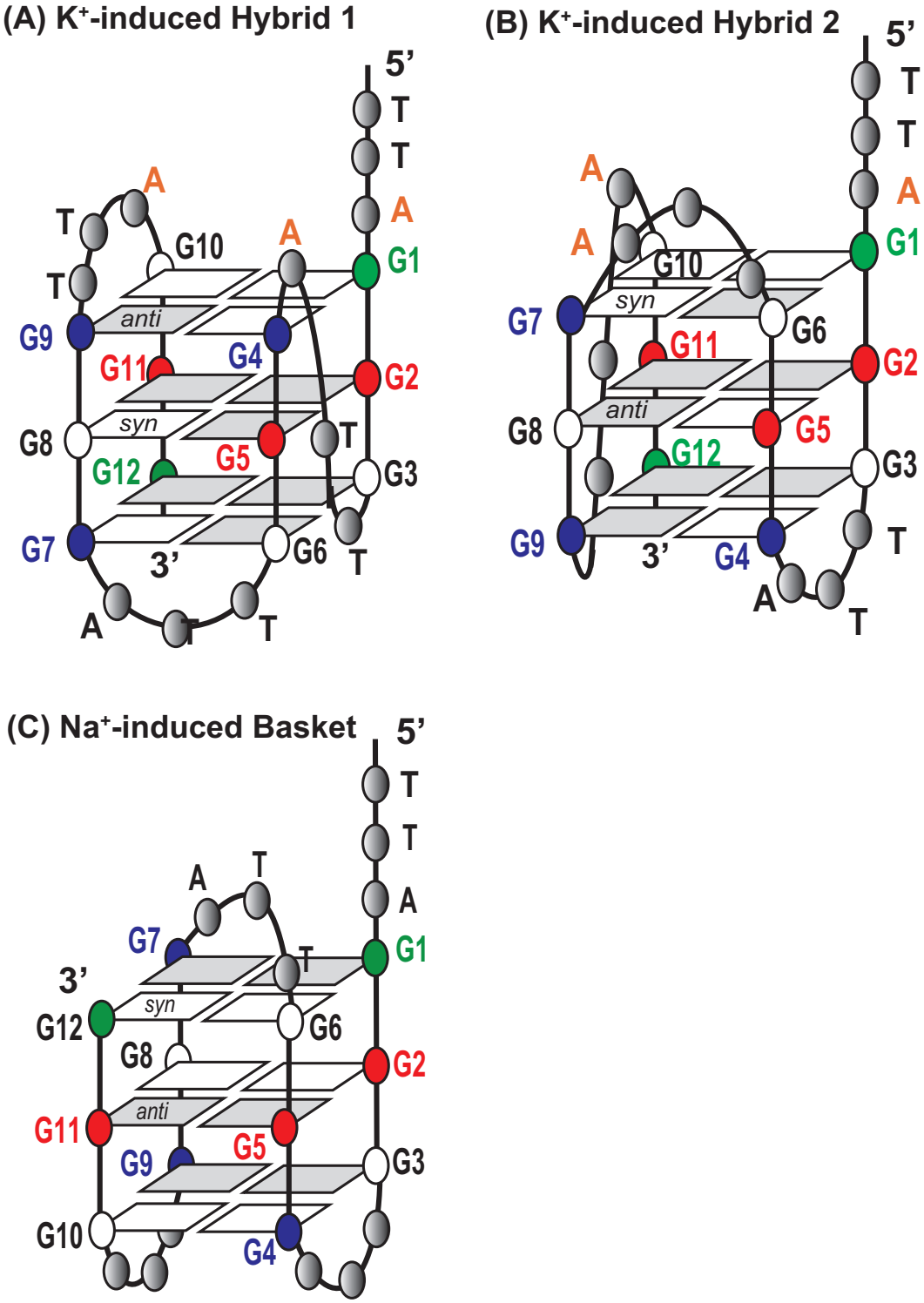

Figure 6.1. Schemes of G-quadruplex formed by the HT_4 in the (A) hybrid-1, (B) hybrid-2 (in K^+), and (B) basket (in Na^+) conformations. Substituted guanine positions shown in colored circles.

K^+, which both promote G-quadruplex folding, the fluorescence intensities differ for each 6MI-labeled sequence, suggesting varying extents of base interactions surrounding these guanine positions. From Hill-binding analyses for the K^+-stabilized quadruplex, we have found that the organization of the bases during folding initiates at low K^+-ion concentrations (<20mM), but better stabilization of the folded conformation requires higher K^+ concentrations (100mM). In addition, the thermodynamic folding pathway appears to initiate within the middle G-tetrad (G5 and G11), followed by the loop regions (G4, G7 and G9), and finally the terminal ends (G1, G2 and G12). For the Na^+-quadruplex conformation, folding may start on the top G-tetrad (G1, G7 and G12) followed by those guanine residues within the middle G-tetrad (G2, G5 and G11).

In the presence of either K^+ or Na^+-stabilizing ions, the two termini of the HT_4 quadruplex sequence (G1 and G12; green circles in Figure 6.1) tend to exhibit "fraying" and "loose association", as seen by their relatively high $K_{0.5}$ values (i.e. K^+ concentration required for 50% quadruplex formation). In addition, position G1, near the 5'-end, exhibits weaker interactions with neighboring bases through base stacking, and minimum effect on quadruplex folding process, as judged from its higher global melting temperature (Tm) value (arising from minimal perturbation from the 6MI mutation), and fluorescence intensity enhancement (in contrast to the usual intensity quenching) with quadruplex folding as promoted by addition of K^+-ions or decreasing temperature. In addition, as the quadruplex folds, G1 is apparently exposed to a more polar environment, as seen from its red-shifted emission spectra relative to that of the unfolded state. DAS suggest that the red shift and intensity enhancement originate from the longest decay component (τ_1). Overall, the fluorescence data suggest that the major local environmental changes surrounding position G1 involves solvent exposure and/or ground-state H-bonding, over base stacking interactions observed for other guanines during quadruplex formation.

Interestingly, fluorescence decay studies provide evidence for a fast (sub-picosecond) interaction (QSSQ) between 6MI and its surrounding bases, which appears to be dependent on the neighboring base in the unfolded state, and may reflect fast electron transfer reactions

from the base to the 6MI. The magnitude of this effect is only nominally enhanced ($< 15\%$) with folding for all the labeled sequences examined, and suggests an additional intrinsic effect arising from base interactions other than from base stacking effects alone.

It is clear that local micro-environments around each 6MI substitution are heterogeneous. Although only one guanine residue is substituted within the oligonucleotide sequence, the fluorescence decays of each 6MI are complex and multi-exponential in both the unfolded or folded states of the quadruplex. The origins for the multi-exponential decay from a single fluorophore suggests micro-heterogeneity for its fluorescence deactivation pathways, arising from either local base stacking interactions or environmental effects (solvent interactions or H-bonding).

Origins for QSSQ may provide preliminary evidence for possible electron-transfer reactions, between bases within the HT_4 in addition to base-stacking interactions, which may be key for protein-quadruplex interactions. Indeed, electron transfer is key within the double-stranded DNA conformation. Future experiments are required to explore this potentially important base-base interactions within the quadruplex conformation.

Environmental "global" heterogeneity was further confirmed by SVD analyses of fluorescence thermal folding profiles, where at least three conformational species (unfolded, intermediate and folded) exist, suggesting that the guanine bases play a significant organization role in the folding process, prior to coiling of the oligonucleotide backbone.

Our studies clearly suggest that the guanine residues of either the Na^+ or K^+-stabilized quadruplex conformations are conformationally distinct. Each position contributes to the overall stability of the quadruplex, but to varying extents. The 5' and 3'-ends exhibit conformational flexibility. In contrast, base stacking interactions within the center-tetrad are key for the quadruplex folding and play a significant role in conformational stability. Future studies can focus on understanding the origins of the intensity enhancement and red shift observed in the G1 labeled sequence resulting from quadruplex folding, specifically whether the absence of the triple adenine platform will effect the fluorescence properties of G1. Since our studies suggested the conformational switch within the Na^+-stabilized

quadruplex formed by the G1 and G7 sequences, it will be interesting to investigate whether the glycosidic bond orientations of 6MI in G1 and G7 are different from the parent HT_4, by solving quadruplex structures of G1 and G7, or measuring the distance between 6MI and the second TTA loop using FRET.

In summary, our biophysical spectroscopic methods in combination with powerful data analysis have focused on mapping the thermodynamic contributions of targeted guanine residues of the human telomeric quadruplex forming sequence, and their local environmental heterogeneity. Many previous studies have examined the binding of possible quadruplex interacting agents, however, our studies have shown that base stacking, solvent interactions of the individual guanine residues of the quadruplex, in combination with possible rapid electron transfer reactions play a central role in the stabilization of the G-quadruplex conformation in presence of either Na^+ or K^+-ions. As discussed, the guanine residues of the quadruplex are conformationally non-equivalent; guanine residues that form the center tetrad are significant for initiating and stabilizing the global quadruplex conformation. As such, folding and unfolding of the quadruplex structure may be modulated by QIA ligands that affect the center tetrad. In contrast, binding of QIAs to the TTA loops or near the terminals of the HT_4 sequence have the potential to provide new chemotherapeutics resulting in stabilizing the folded conformation and resultant telomerase inhibition.

Future studies can focus on whether the fluorescence intensity enhancement and red shift still dominate for the labeled G1 sequence on quadruplex folding, after the 5'-end TTA region within the HT_4 sequence is removed (i.e. $GGG(TTAGGG)_3$). This experiment allow us to investigate if the formation/removal of the triple adenine platform (Figure 6.1A) affect the local dynamics of G1 and G7. In addition, since our studies suggest possible conformational switch within the Na^+-stabilized quadruplex formed by the G1 and G7 sequences, solving their quadruplex structures with NMR or X-ray crystallography can ultimately provide insights into whether the glycosidic bond angles are indeed altered by the 6MI substitutions, and if the alteration in the GBA results in more favorable folding of the quadruplex by G1 and G7 in Na^+.

Bibliography

[1] Cancer Facts & Figures 2010, 2010.

[2] L. Hayflick and P. S. Moorhead. The serial cultivation of human diploid cell strains. *Exp Cell Res*, 25:585–621, 1961.

[3] Calvin B. Harley, A. Bruce Futcher, and Carol W. Greider. Telomeres shorten during ageing of human fibroblasts. *Nature*, 345(6274):458–460, May 1990.

[4] R. K. Moyzis, J. M. Buckingham, L. S. Cram, M. Dani, L. L. Deaven, M. D. Jones, J. Meyne, R. L. Ratliff, and J. R. Wu. A highly conserved repetitive DNA sequence, (TTAGGG)n, present at the telomeres of human chromosomes. *Proceedings of the National Academy of Sciences*, 85(18):6622–6626, 1988.

[5] W. E. Wright, V. M. Tesmer, K. E. Huffman, S. D. Levene, and J. W. Shay. Normal human chromosomes have long G-rich telomeric overhangs at one end. *Genes Dev*, 11(21):2801–9, 1997.

[6] A. M. Olovnikov. A theory of marginotomy. *J Theor Biol*, 41(1):181–90, 1973.

[7] J. D. Watson. Origin of Concatemeric T7 DNA. *Nature New Biology*, 239:197–201, 1972.

[8] Fabrizio d'Adda di Fagagna, Philip M. Reaper, Lorena Clay-Farrace, Heike Fiegler, Philippa Carr, Thomas von Zglinicki, Gabriele Saretzki, Nigel P. Carter, and Stephen P. Jackson. A DNA damage checkpoint response in telomere-initiated senescence. *Nature*, 426(6963):194–198, November 2003.

[9] Hiroyuki Takai, Agata Smogorzewska, and Titia de Lange. DNA Damage Foci at Dysfunctional Telomeres. *Current Biology*, 13(17):1549 – 1556, 2003.

[10] Carol W. Greider and Elizabeth H. Blackburn. Identification of a specific telomere terminal transferase activity in *Tetrahymena* extracts. *Cell*, 43(2, Part 1):405 – 413, 1985.

[11] Gregg B. Morin. The human telomere terminal transferase enzyme is a ribonucleoprotein that synthesizes TTAGGG repeats. *Cell*, 59(3):521 – 529, 1989.

[12] C. I. Nugent and V. Lundblad. The telomerase reverse transcriptase: components and regulation. *Genes Dev*, 12(8):1073–1085, Apr 1998.

[13] J. Lingner and T. R. Cech. Telomerase and chromosome end maintenance. *Curr Opin Genet Dev*, 8(2):226–232, Apr 1998.

[14] J Feng, WD Funk, SS Wang, SL Weinrich, AA Avilion, CP Chiu, RR Adams, E Chang, RC Allsopp, J Yu, and et al. The RNA component of human telomerase. *Science*, 269(5228):1236–1241, 1995.

[15] Thomas R. Cech. Life at the End of the Chromosome: Telomeres and Telomerase. *Angewandte Chemie International Edition*, 39(1):34–43, 2000.

[16] W. E. Wright, M. A. Piatyszek, W. E. Rainey, W. Byrd, and J. W. Shay. Telomerase activity in human germline and embryonic tissues and cells. *Dev Genet*, 18(2):173–179, 1996.

[17] Dara L. Aisner, Woodring E. Wright, and Jerry W. Shay. Telomerase regulation: not just flipping the switch. *Current Opinion in Genetics & Development*, 12(1):80 – 85, 2002.

[18] Y. S. Cong, W. E. Wright, and J. W. Shay. Human telomerase and its regulation. *Microbiol Mol Biol Rev*, 66(3):407–25, table of contents, 2002.

[19] N. R. Forsyth, W. E. Wright, and J. W. Shay. Telomerase and differentiation in multicellular organisms: Turn it off, turn it on, and turn it off again. *Differentiation*, 69(4-5):188–197, 2002.

[20] Jerry W Shay and Woodring E Wright. Telomeres and telomerase in normal and cancer stem cells. *FEBS Lett*, 584(17):3819–3825, Sep 2010.

[21] Ying Zou, Agnel Sfeir, Sergei M. Gryaznov, Jerry W. Shay, and Woodring E. Wright. Does a Sentinel or a Subset of Short Telomeres Determine Replicative Senescence? *Mol. Biol. Cell*, 15(8):3709–3718, 2004.

[22] Calvin B. Harley. Telomere loss: mitotic clock or genetic time bomb? *Mutation Research/DNAging*, 256(2-6):271 – 282, 1991.

[23] Jerry W. Shay and Woodring E. Wright. Telomerase activity in human cancer. *Current Opinion in Oncology*, 8(1):66–71, 1996.

[24] J.D. Henson, A.A. Neumann, T.R. Yeager, and R.R. Reddel. Alternative lengthening of telomeres in mammalian cells. *Oncogene*, 21(1):598–610, 2002.

[25] Roger R. Reddel. Alternative lengthening of telomeres, telomerase, and cancer. *Cancer Letters*, 194(2):155 – 162, 2003. Telomeres, Telomerase and The Cancer Cell.

[26] J.P. Murnane, L. Sabatier, B. A. Marder, and W. F. Morgan. Telomere dynamics in an immortal human cell line. *EMBO Journal*, 13:4953–62, 1994.

[27] J. W. Shay and W. E. Wright. *Telomeres*, chapter Telomerase and Human Cancer, pages 81–108. Cold Srping Harbor Laboratory Press, 2006.

[28] J.W. Shay and S. Bacchetti. A survey of telomerase activity in human cancer. *European Journal of Cancer*, 33(5):787 – 791, 1997. Telomeres and Telomerase in Cancer.

[29] W E Wright, O M Pereira-Smith, and J W Shay. Reversible cellular senescence: implications for immortalization of normal human diploid fibroblasts. *Mol. Cell. Biol.*, 9(7):3088–3092, 1989.

[30] N. W. Kim, M. A. Piatyszek, K. R. Prowse, C. B. Harley, M. D. West, P. L. Ho, G. M. Coviello, W. E. Wright, S. L. Weinrich, and J. W. Shay. Specific association of human telomerase activity with immortal cells and cancer. *Science*, 266(5193):2011–5, 1994.

[31] Jerry W Shay and Woodring E Wright. Telomerase therapeutics for cancer: challenges and new directions. *Nature Reviews Drug Discovery*, 5:577–584, 2006.

[32] Laura K. White, Woodring E. Wright, and Jerry W. Shay. Telomerase inhibitors. *Trends in Biotechnology*, 19(3):114 – 120, 2001.

[33] Anne De Cian, Laurent Lacroix, Celine Douarre, Nassima Temime-Smaali, Chantal Trentesaux, Jean-Francois Riou, and Jean-Louis Mergny. Targeting telomeres and telomerase. *Biochimie*, 90(1):131 – 155, 2008. Telomeres and Telomerase: from Basic Research to Clinical Applications.

[34] Mirancea N. Boukamp, P. Telomeres rather than telomerase a key target for anti-cancer therapy? *Experimental Dermatology*, 16:71–79, 2006.

[35] Sarah Burge, Gary N. Parkinson, Pascale Hazel, Alan K. Todd, and Stephen Neidle. Quadruplex DNA: sequence, topology and structure. *Nucleic Acids Research*, 34(19):5402–5415, 2006.

[36] G Laughlan, AI Murchie, DG Norman, MH Moore, PC Moody, DM Lilley, and B Luisi. The high-resolution crystal structure of a parallel-stranded guanine tetraplex. *Science*, 265(5171):520–524, 1994.

[37] J. Meyne, R. L. Ratliff, and R. K. Moyzis. Conservation of the human telomere sequence (TTAGGG)n among vertebrates. *Proc Natl Acad Sci U S A*, 86(18):7049–53, 1989.

[38] Michael G. Schechtman. Characterization of telomere DNA from *Neurospora crassa*. *Gene*, 88(2):159 – 165, 1990.

[39] L. A. Klobutcher, M. T. Swanton, P. Donini, and D. M. Prescott. All gene-sized DNA molecules in four species of hypotrichs have the same terminal sequence and an unusual 3' terminus. *Proc Natl Acad Sci U S A*, 78:30153019, 1981.

[40] Janis Shampay, Jack W. Szostak, and Elizabeth H. Blackburn. DNA sequences of telomeres maintained in yeast. *Nature*, 310(5973):154–157, July 1984.

[41] Alan K. Todd, Matthew Johnston, and Stephen Neidle. Highly prevalent putative quadruplex sequence motifs in human DNA. *Nucleic Acids Research*, 33(9):2901–2907.

[42] Julian L. Huppert and Shankar Balasubramanian. Prevalence of quadruplexes in the human genome. *Nucleic Acids Research*, 33(9):2908–2916.

[43] Pooja Rawal, Veera Bhadra Rao Kummarasetti, Jinoy Ravindran, Nirmal Kumar, Kangkan Halder, Rakesh Sharma, Mitali Mukerji, Swapan Kumar Das, and Shantanu Chowdhury. Genome-wide prediction of G4 DNA as regulatory motifs: Role in *Escherichia coli* global regulation. *Genome Research*, 16(5):644–655, 2006.

[44] Sunita Kumari, Anthony Bugaut, Julian L Huppert, and Shankar Balasubramanian. An RNA G-quadruplex in the 5[prime] UTR of the NRAS proto-oncogene modulates translation. *Nat Chem Biol*, 3(4):218–221, April 2007.

[45] Adam Siddiqui-Jain, Cory L. Grand, David J. Bearss, and Laurence H. Hurley. Direct evidence for a G-quadruplex in a promoter region and its targeting with a small molecule to repress c-MYC transcription. *Proceedings of the National Academy of Sciences*, 99(18):11593–11598, 2002.

[46] Daekyu Sun, Kexiao Guo, Jadrian J. Rusche, and Laurence H. Hurley. Facilitation of a structural transition in the polypurine/polypyrimidine tract within the proximal promoter region of the human VEGF gene by the presence of potassium and G-quadruplex-interactive agents. *Nucleic Acids Research*, 33(18):6070–6080.

[47] Richard De Armond, Stacey Wood, Daekyu Sun, Laurence H. Hurley, and Scot W. Ebbinghaus. Evidence for the Presence of a Guanine Quadruplex Forming Region within a Polypurine Tract of the Hypoxia Inducible Factor 1 Promoter. *Biochemistry*, 44(49):16341–16350, 2005. PMID: 16331995.

[48] Sarah Rankin, Anthony P. Reszka, Julian Huppert, Mire Zloh, Gary N. Parkinson, Alan K. Todd, Sylvain Ladame, Shankar Balasubramanian, and Stephen Neidle. Putative DNA Quadruplex Formation within the Human c-kit Oncogene. *Journal of the American Chemical Society*, 127(30):10584–10589, 2005.

[49] Cheng-Chung Chang, I.-Chun Kuo, I.-Fang Ling, Chin-Tin Chen, Huei-Chin Chen, Pei-Jen Lou, Jing-Jer Lin, and Ta-Chau Chang. Detection of Quadruplex DNA Structures in Human Telomeres by a Fluorescent Carbazole Derivative. *Analytical Chemistry*, 76(15):4490–4494, 2004. PMID: 15283592.

[50] Katrin Paeschke, Tomas Simonsson, Jan Postberg, Daniela Rhodes, and Hans Joachim Lipps. Telomere end-binding proteins control the formation of G-quadruplex DNA structures in vivo. *Nat Struct Mol Biol*, 12(10):847–854, October 2005.

[51] Amy Lew, William J. Rutter, and Giulia C. Kennedy. Unusual DNA structure of the diabetes susceptibility locus IDDM2 and its effect on transcription by the insulin promoter factor Pur-1/MAZ. *Proceedings of the National Academy of Sciences*, 97(23):12508–12512, 2000.

[52] Naijie Jing, Yidong Li, Weijun Xiong, Wei Sha, Ling Jing, and David J. Tweardy. G-Quartet Oligonucleotides: A New Class of Signal Transducer and Activator of Transcription 3 Inhibitors That Suppresses Growth of Prostate and Breast Tumors through Induction of Apoptosis. *Cancer Research*, 64(18):6603–6609, 2004.

[53] Haiyan Qi, Chao-Po Lin, Xuan Fu, Laurence M. Wood, Angela A. Liu, Yuan-Chin Tsai, Yongjie Chen, Christopher M. Barbieri, Daniel S. Pilch, and Leroy F. Liu. G-Quadruplexes Induce Apoptosis in Tumor Cells. *Cancer Research*, 66(24):11808–11816, 2006.

[54] Shankar Balasubramanian and Stephen Neidle. G-quadruplex nucleic acids as therapeutic targets. *Current Opinion in Chemical Biology*, 13(3):345 – 353, 2009. Next Generation Therapeutics.

[55] J. Dai, C. Punchihewa, A. Ambrus, D. Chen, R. A. Jones, and D. Yang. Structure of the intramolecular human telomeric G-quadruplex in potassium solution: a novel adenine triple formation. *Nucleic Acids Res*, 35(7):2440–50, 2007.

[56] J. Dai, M. Carver, C. Punchihewa, R. A. Jones, and D. Yang. Structure of the Hybrid-2 type intramolecular human telomeric G-quadruplex in K+ solution: insights into structure polymorphism of the human telomeric sequence. *Nucleic Acids Res*, 35(15):4927–40, 2007.

[57] G. N. Parkinson, M. P. Lee, and S. Neidle. Crystal structure of parallel quadruplexes from human telomeric DNA. *Nature*, 417(6891):876–80, 2002.

[58] Y. Wang and D. J. Patel. Solution structure of the human telomeric repeat d[AG3(T2AG3)3] G-tetraplex. *Structure*, 1(4):263–82, 1993.

[59] Jean-Franois Chantot and Wilhelm Guschlbauer. Physicochemical properties of nucleosides 3. Gel formation by 8-bromoguanosine. *FEBS Letters*, 4(3):173 – 176, 1969.

[60] Nicholas V. Hud, Flint W. Smith, Frank A. L. Anet, and Juli Feigon. The Selectivity for K+ versus Na+ in DNA Quadruplexes Is Dominated by Relative Free Energies of Hydration:? A Thermodynamic Analysis by 1H NMRc. *Biochemistry*, 35(48):15383–15390, January 1996.

[61] Correia J.J. Wang L. Trent J.O. Chaires J.B. Li, J. Not so crystal clear: The structure of the human telomere G-quadruplex in solution differs from that present in a crystal. *Nucleic Acids Research*, 33(14):4649–4659, 2005. cited By (since 1996) 128.

[62] Y. He, R. D. Neumann, and I. G. Panyutin. Intramolecular quadruplex conformation of human telomeric DNA assessed with 125I-radioprobing. *Nucleic Acids Res*, 32(18):5359–67, 2004.

[63] L. Ying, J. J. Green, H. Li, D. Klenerman, and S. Balasubramanian. Studies on the structure and dynamics of the human telomeric G quadruplex by single-molecule fluorescence resonance energy transfer. *Proc Natl Acad Sci U S A*, 100(25):14629–34, 2003.

[64] Bombard S. Elizondo-Riojas M.-A. Chottard J.-C. Redon, S. Platinum cross-linking of adenines and guanines on the quadruplex structures of the AG3(T2AG3)3 and (T2AG3)4 human telomere sequences in Na+ and K+ solutions. *Nucleic Acids Research*, 31(6):1605–1613, 2003. cited By (since 1996) 63.

[65] J. Qi and R. H. Shafer. Covalent ligation studies on the human telomere quadruplex. *Nucleic Acids Res*, 33(10):3185–92, 2005.

[66] J. Dai, M. Carver, and D. Yang. Polymorphism of human telomeric quadruplex structures. *Biochimie*, 90(8):1172–83, 2008.

[67] R. D. Gray and J. B. Chaires. Kinetics and mechanism of K+- and Na+-induced folding of models of human telomeric DNA into G-quadruplex structures. *Nucleic Acids Res*, 36(12):4191–203, 2008.

[68] Robert D. Gray, Luigi Petraccone, John O. Trent, and Jonathan B. Chaires. Characterization of a K+-Induced Conformational Switch in a Human Telomeric DNA Oligonucleotide Using 2-Aminopurine Fluorescence. *Biochemistry*, 49(1):179–194, 2010. PMID: 19961180.

[69] Yan Xu, Yuki Noguchi, and Hiroshi Sugiyama. The new models of the human telomere d[AGGG(TTAGGG)3] in K+ solution. *Bioorganic & Medicinal Chemistry*, 14(16):5584 – 5591, 2006.

[70] Kenji Okamoto, Yuta Sannohe, Tomoko Mashimo, Hiroshi Sugiyama, and Masahide Terazima. G-quadruplex structures of human telomere DNA examined by single molecule FRET and BrG-substitution. *Bioorganic & Medicinal Chemistry*, 16(14):6873 – 6879, 2008.

[71] J. Gros, F. Rosu, S. Amrane, A. De Cian, V. Gabelica, L. Lacroix, and J. L. Mergny. Guanines are a quartet's best friend: impact of base substitutions on the kinetics and stability of tetramolecular quadruplexes. *Nucleic Acids Res*, 35(9):3064–75, 2007.

[72] Cory L. Grand, Tiffanie J. Powell, Raymond B. Nagle, David J. Bearss, Denise Tye, Mary Gleason-Guzman, and Laurence H. Hurley. Mutations in the G-quadruplex silencer element and their relationship to c-MYC overexpression, NM23 repression, and therapeutic rescue. *Proceedings of the National Academy of Sciences of the United States of America*, 101(16):6140–6145, 2004.

[73] Jie Xiao, Andrew M. Lee, and Scott F. Singleton. Construction and evaluation of a kinetic scheme for RecA-mediated DNA strand exchange. *Biopolymers*, 81(6):473–496, 2006.

[74] S. F. Singleton, A. I. Roca, A. M. Lee, and J. Xiao. Probing the structure of RecA-DNA filaments. Advantages of a fluorescent guanine analog. *Tetrahedron*, 63(17):3553–3566, 2007.

[75] Jeffrey C. Myers, Sheila A. Moore, and Yousif Shamoo. Structure-based Incorporation of 6-Methyl-8-(2-deoxy--ribofuranosyl)isoxanthopteridine into the Human Telomeric Repeat DNA as a Probe for UP1 Binding and Destabilization of G-tetrad Structures. *Journal of Biological Chemistry*, 278(43):42300–42306, 2003.

[76] Mary E. Hawkins, Wolfgang Pfleiderer, Frank M. Balis, Denise Porter, and Jay R. Knutson. Fluorescence Properties of Pteridine Nucleoside Analogs as Monomers and Incorporated into Oligonucleotides. *Analytical Biochemistry*, 244(1):86 – 95, 1997.

[77] J. L. Mergny, J. Li, L. Lacroix, S. Amrane, and J. B. Chaires. Thermal difference spectra: a specific signature for nucleic acid structures. *Nucleic Acids Res*, 33(16):e138, 2005.

[78] Jean-Louis Mergny and Laurent Lacroix. *UV Melting of G-Quadruplexes*. John Wiley & Sons, Inc., 2009.

[79] J. L. Mergny, A. T. Phan, and L. Lacroix. Following G-quartet formation by UV-spectroscopy. *FEBS Lett*, 435(1):74–8, 1998.

[80] Phillip A. Rachwal and Keith R. Fox. Quadruplex melting. *Methods*, 43(4):291 – 301, 2007. Quadruplex DNA.

[81] C. R. Cantor and P.R. Schimmel. *Biophysical Chemistry: Part III: The Behavior of Biological Macromolecules*. W. H. Freeman, 1980.

[82] Mary Hawkins. Fluorescent pteridine nucleoside analogs. *Cell Biochemistry and Biophysics*, 34:257–281, 2001. 10.1385/CBB:34:2:257.

[83] Kristi Wojtuszewski Poulin, Aleksandr V. Smirnov, Mary E. Hawkins, Frank M. Balis, and Jay R. Knutson. Conformational Heterogeneity and Quasi-Static Self-Quenching in DNA Containing a Fluorescent Guanine Analogue, 3MI or 6MI. *Biochemistry*, 48(37):8861–8868, 2009. PMID: 19610668.

[84] Jerson L. Silva, Edith W. Miles, and Gregorio Weber. Pressure dissociation and conformational drift of the β dimer of tryptophan synthase. *Biochemistry*, 25(19):5780–5786, 1986.

[85] D. Voet and J. G. Voet. *Biochemistry*. John Wiley & Sons, Inc., 2004.

[86] Harvey Lodish, Arnold Berk, C.A. Kaiser, M. Krieger, M.P. Scott, A. Bretscher, H. Ploegh, and P. Matsudaira. *Molecular cell biology*. W. H. Freeman, 6th edition, 2007.

[87] Madhavan Narayanan, Goutham Kodali, Yangjun Xing, Mary E. Hawkins, and Robert J. Stanley. Differential fluorescence quenching of fluorescent nucleic acid base analogues by native nucleic acid monophosphates. *The Journal of Physical Chemistry B*, 114(17):5953–5963, 2010.

[88] Shana O. Kelley and Jacqueline K. Barton. Electron Transfer Between Bases in Double Helical DNA. *Science*, 283(5400):375–381, 1999.

[89] Vladimir Shafirovich, Alexander Dourandin, Natalia P. Luneva, and Nicholas E. Geacintov. The kinetic deuterium isotope effect as a probe of a proton coupled electron transfer mechanism in the oxidation of guanine by 2-aminopurine radicals. *The Journal of Physical Chemistry B*, 104(1):137–139, 2000.

[90] Torsten Fiebig, Chaozhi Wan, and Ahmed H. Zewail. Femtosecond Charge Transfer Dynamics of a Modified DNA Base: 2-Aminopurine in Complexes with Nucleotides. *ChemPhysChem*, 3(9):781–788, 2002.

[91] Melanie A. O'Neill, Chikara Dohno, and Jacqueline K. Barton. Direct chemical evidence for charge transfer between photoexcited 2-aminopurine and guanine in duplex dna. *Journal of the American Chemical Society*, 126(5):1316–1317, 2004. PMID: 14759170.

[92] C. Antonacci, J. B. Chaires, and R. D. Sheardy. Biophysical characterization of the human telomeric (TTAGGG)4 repeat in a potassium solution. *Biochemistry*, 46(15):4654–60, 2007.

[93] A. N. Lane, J. B. Chaires, R. D. Gray, and J. O. Trent. Stability and kinetics of G-quadruplex structures. *Nucleic Acids Res*, 36(17):5482–515, 2008.

[94] Mugurel G. Badea and Ludwig Brand. Time-resolved fluorescence measurements. In Serge N. Timasheff C.H.W. Hirs, editor, *Enzyme Structure Part H*, volume 61 of *Methods in Enzymology*, pages 378 – 425. Academic Press, 1979.

[95] Joseph R. Lakowicz. Time-Resolved Protein Fluorescence. In *Principles of Fluorescence Spectroscopy*, pages 580–581. Springer, New York, 3 edition, 2006.

[96] R. F. Chen, J. R. Knutson, H. Ziffer, and D. Porter. Fluorescence of tryptophan dipeptides: correlations with the rotamer model. *Biochemistry*, 30(21):5184–95, 1991.

[97] Joseph R. Lakowicz. Principles of Fluorescence Spectroscopy. chapter 8, page 280. Springer, 2006.

[98] Jay R. Knutson, Dana G. Walbridge, and Ludwig Brand. Decay-associated fluorescence spectra and the heterogeneous emission of alcohol dehydrogenase. *Biochemistry*, 21(19):4671–4679, 1982.

[99] Joseph M. Beechem, Jay R. Knutson, J. B. Alexander Ross, Benjamin W. Turner, and Ludwig Brand. Global resolution of heterogeneous decay by phase/modulation fluorometry: mixtures and proteins. *Biochemistry*, 22(26):6054–6058, December 1983.

[100] Robert D. Gray and Jonathan B. Chaires. *Analysis of Multidimensional G-Quadruplex Melting Curves*. John Wiley & Sons, Inc., 2011.

[101] E.R. Henry and J. Hofrichter. Singular value decomposition: Application to analysis of experimental data. In Michael L. Johnson Ludwig Brand, editor, *Numerical Computer Methods*, volume 210 of *Methods in Enzymology*, pages 129 – 192. Academic Press, 1992.

[102] Katarzyna J. Macura Antonio C. Wolff Vered Stearns Sarah D. Mezban Nagi F. Khouri David A. Bluemke Ronald Ouwerkerk, Michael A. Jacobs and Paul A. Bottomley. Elevated tissue sodium concentration in malignant breast lesions detected with non-invasive 23Na MRI. *BREAST CANCER RESEARCH AND TREATMENT*, 106:151–160, 2007.

[103] I Z Nagy, G Lustyik, V Z Nagy, B Zarndi, and C Bertoni-Freddari. Intracellular Na+:K+ ratios in human cancer cells as revealed by energy dispersive x-ray micro-analysis. *The Journal of Cell Biology*, 90(3):769–777, 1981.